Detector and read-out development to search for sterile neutrinos with KATRIN

Entwicklung von Detektoren und Ausleseelektronik für die Suche nach sterilen Neutrinos mit KATRIN

MASTERARBEIT

von

Kai Dolde

Erstgutachter:	Prof. Dr. Guido Drexlin Institut für Kernphysik, KIT
Zweitgutachter:	Prof. Dr. Günter Quast Institut für Experimentelle Kernphysik, KIT
Betreuerin:	Dr. Susanne Mertens Institut für Experimentelle Kernphysik, KIT Lawrence Berkeley National Laboratory

Erklärung

Hiermit versichere ich wahrheitsgemäß, die Masterarbeit selbstständig angefertigt, alle benutzten Hilfsmittel vollständig und genau angegeben und alles kenntlich gemacht zu haben, was aus der Arbeit anderer unverändert oder mit Abänderung entnommen wurde.

Kai Dolde
Karlsruhe, 31.03.2016

Acknowledgements

This work would not have been possible without the help of many people. I would like to thank

- SUSANNE MERTENS for the excellent supervision in Berkeley and Karlsruhe and her never-ending and very motivating engagement during my master thesis,
- GUIDO DREXLIN who always supported me during my work as a student assistant as well as during my master thesis and enabled my very interesting research stays abroad,
- DAVID RADFORD for the brilliant input during my stay at Oak Ridge National Laboratory and for his continuous support on all arising questions in the context of my work on detectors and ADC Non-Linearities,
- GÜNTER QUAST for being the second reviewer of my thesis and for showing great interest in the topic,
- MARC KORZECZEK, ANTON HUBER and THIERRY LASSERRE for a nice working atmosphere in the TRISTAN group and at meetings and conferences,
- IVAN PERIC and ROBERTO BLANCO from IPE for their friendly supervision in context of the PCB design,
- SASCHA WÜSTLING, who always had an open ear for all questions on electronics,
- PETER LECHNER from HLL Munich for his big efforts in sensor design and support,
- JOACHIM WOLF for his support in respect to all hardware related issues and
- KEVIN SCHÄFER for his work on the technical drawings for the test stand setup.

Summary

Sterile neutrinos are a well-motivated extension of the Standard Model (SM) of particle physics and provide an explanation for the non-zero mass of active neutrinos. They are right-handed singulets and can have an arbitrary mass scale. For example, the νMSM [1] suggests the existence of sterile neutrinos and in particular foresees one of them to have a mass in the kiloelectron volt (keV) range. Sterile neutrinos with a mass in this range are highly motivated from a cosmological point of view. They are prime candidates for both Warm and Cold Dark Matter, being in good agreement with small- to large-scale structure observations.
The KATRIN (KArlsruhe TRItium Neutrino) experiment, designed to measure the effective mass of active neutrinos with a sensitivity of 200 meV at 90% C.L., shows a promising potential to also search for sterile neutrinos. With an endpoint energy of 18.6 keV, the large number of tritium β-decays in the source provides the option to look for the kink-like signature of a sterile neutrino with high sensitivity. For this purpose the entire tritium β-decay spectrum has to be observed and hence, the spectrometer, acting as a low-pass filter for β-decay electrons, has to be operated at small retarding voltages. To handle the high counting rates in this measurement mode, a novel detector and read-out system is required.
The focus of this work is on the design and development of this novel detector and read-out system. The first part of the thesis introduces the silicon prototype detector TRISTAN, that for the first time combines the advantages of a silicon drift detector (SDD) with a very thin dead layer ($\approx$ 10 nm). Two versions with different parameters were produced at HLL Munich, the Halbleiterlabor of the Max-Planck Society, and at Lawrence Berkeley National Laboratory.
Within the framework of this thesis, the read-out electronics for TRISTAN was developed in collaboration with the Institute for Data Processing and Electronics (IPE), KIT. A printed circuit board (PCB) was designed which connects the prototype detector with a low-noise preamplifier ASIC, which was specifically desgined for TRISTAN. First successful tests demonstrate the functionality of the detector and read-out electronics. Furthermore, a test stand including a vacuum and cooling system was designed and built. This setup will enable a detailed characterization

of the detectors.
The second part of this thesis addresses the design for a large-scale detector system. Here, the focus is especially set on defining the requirements for the Analog-to-Digital Converters (ADCs). Test measurements of a particular high-performance ADC have been performed at Lawrence Berkeley National Laboratory.
Based on these measurements, different techniques to correct and mitigate ADC Non-Linearities (NLs) have been investigated. Detailed simulations, based on both Monte Carlo and analytical methods, identify ADC Non-Linearities to be a strong limiting factor and one of the most critical systematic uncertainties in the search for sterile neutrinos with KATRIN.
A major result of this work is the development of several means of mitigating the effect of ADC NLs. For instance, it was demonstrated that a sophisticated read-out system with full digitization of single particle waveforms is very promising to sufficiently average out the characteristic structure of ADC Non-Linearities. Moreover, usage of the built-in post-acceleration electrode further decreases the uncertainties. Applying all mitigation strategies will allow to reduce the effect of NLs on the spectral shape from the percent level to the level of 10^{-7}.
The investigations culminate in a detailed sensitivity study on the impact of ADC NLs on the KATRIN sensitivity for a sterile neutrino search and underline the importance of the developed reduction mechanisms.

Zusammenfassung

Sterile Neutrinos stellen eine Erweiterung des Standard Models der Teilchenphysik dar und liefern eine Erklärung für Neutrinomassen. Es handelt sich dabei um rechts-chirale Teilchen, die lediglich gravitativ wechselwirken. Sterile Neutrinos können in beliebigen Massenbereichen auftreten. Massen von einigen Kiloelektronenvolt (keV) sind kosmologisch gesehen stark motiviert, da sterile Neutrinos in diesem Massenbereich geeignete Kandidaten für warme und kalte dunkle Materie sind.
Das KATRIN (KArlsruhe TRItium Neutrino) Experiment hat das Ziel, die effektive Masse von aktiven Neutrinos mit einer Sensitivität von 200 meV mit 90% C.L. zu bestimmen. Darüberhinaus bietet es die vielversprechende Möglichkeit nach sterilen Neutrinos zu suchen. Um allerdings das gesamte Tritiumzerfallsspektrum auf differenzielle Art und Weise zu vermessen, was für die Suche nach sterilen Neutrinos im keV Massenbereich notwendig wäre, ist ein neuartiges Detektor- und Auslesesystem notwendig, um die auftretenden hohen Zählraten zu detektieren.
Der Schwerpunkt dieser Arbeit liegt im Design und der Entwicklung von dieses Detektor- und Auslesesystems.
Zunächst wird der Prototypdetektor TRISTAN vorgestellt, der in seinem Design die Vorzüge von Silizium Driftdetektoren und dünnen Totschichten vereint. Im Rahmen dieser Arbeit wurde in Zusammenarbeit mit dem Institut für Prozessdatenverarbeitung und Elektronik (IPE), KIT, die Ausleseelektronik für TRISTAN entworfen. Das in dieser Arbeit konzipierte Printed Circuit Board (PCB) verbindet den Prototyp Detektor mit einem rauscharmen Vorverstärker ASIC, der speziell für TRISTAN produziert wurde. Erste Messungen zeigen die Funktionsfähigkeit des Detektors und der Ausleseelektronik. Außerdem wurde im Kontext dieser Arbeit ein Vakuumteststand aufgebaut, um eine detaillierte Charakterisierung der Detektoren zu ermöglichen.
Ein weiterer Fokus der Arbeit ist die Untersuchung der Anforderungen an die Ausleseelektronik für ein neuartiges Detektorsystem. Das Hauptaugenmerk liegt dabei auf den Anforderungen an Analog-Digital-Wandler (ADCs). In diesem Zusammenhang wurden dedizierte Messungen am Lawrence Berkeley National Labo-

ratory durchgeführt um ADC Nichtlinearitäten (NL) zu messen und neue Korrekturmethoden zu testen. Desweiteren identifizieren detaillierte Simulationen, basierend auf Monte Carlo Methoden und analytischen Modellen, diese Nichtlinearitäten als wesentliche systematische Unsicherheit. Untersuchungen zeigen, dass die durch ADC Nichlinearitäten verursachte systematische Unsicherheit von einigen Prozent auf ein Level von 10^{-7} reduziert werden kann, wenn verschiedene in dieser Arbeit entwickelte NL-Reduktionsmethoden eingesetzt werden. Diese basieren auf einer vollständigen Digitalisierung der Teilchen-Signalpulse und auf dem Einsatz der in KATRIN eingebauten Nachbeschleunigungselektrode. Die Untersuchungen werden mit einer detaillierten Sensitivitätsstudie abschlossen, die die Auswirkungen von Nichtlinearitäten auf die KATRIN Sensitivität für sterile Neutrinos aufzeigt und die Notwendigkeit der entwickelten Reduktionsmethoden deutlich macht.

Contents

List of Abbreviations

Symbol	Description
A	Mass number
ADC	Analog-to-Digital Converter
α	α particle, i.e. Helium nucleus
AgPd	Silver palladium
Au	Gold (element)
B	Magnetic field
β	electron from β-decay
C_d	Detector capacity
CDF	Cumulative Density Function
CDM	Cold Dark Matter
C.L.	Confidence Level
CPS	Cryogenic Pumping Section
DAC	Digital-to-Analog Converter
DAQ	Data acquisition
$d\Gamma/dE$	Fermi function to describe tritium β-decay
DPS	Differential Pumping Section
E_0	Endpoint energy
E_{ehp}	Necessary energy to create an electron-hole-pair in silicon
E_{INL}	Trapezoidal filter output of an INL de-corrected waveform
E_ν	Neutrino energy
ΔE_σ	Gaussian 1 σ energy resolution
ΔE_{FWHM}	FWHM energy resolution
f_c	Corner frequency of low-pass filter
FPD	Focal Plane Detector
FWHM	Full Width Half Maximum
γ	γ particle
GND	Ground potential
GRETINA	Gamma-Ray Energy Tracking In-beam Nuclear Array experiment

GUT	Grand Unified Theory
HLL	Halbleiter Labor of the Max-Planck Society, Munich
INL	Integral Non-Linearity
KATRIN	KArlsruhe TRItium Neutrino experiment
ΛCDM	Standard model of cosmology, Λ = Einstein's cosmological constant
LBNL	Lawrence Berkeley National Laboratory
LSB	Least Significant Bit
Δm^2	Difference of mass squares in neutrino oscillation experiments
MAC-E filter	Magnetic Adiabatic Collimation with Electrostatic filter
m_e	Electron mass
m_{ee}	Effective Majorana neutrino mass
m_D	Dirac mass of neutrino
m_ν	Neutrino mass
m_{ν_e}	Effective neutrino mass
M_p	Planck scale $\approx 10^{19}$ GeV
M_R	Majorana mass of neutrino
m_s	Sterile neutrino mass
n	Neutron
NL	Non-Linearity
ν_1, ν_2, ν_3	Neutrino mass eigenstates
ν_α	Neutrino flavor eigenstate
$\overline{\nu}_e$	Electron anti-neutrino
ν_L, ν_R	Left-handed and right-handed neutrino
νMSM	Neutrino Minimal Standard Model
ORNL	Oak Ridge National Laboratory
p	Proton
PCB	Printed Circuit Board
PDF	Probability Density Function
Φ_0	Higgs vacuum expectation value
PMNS	Pontecorvo-Maki-Nakagawa-Sakata Matrix
r	Radius
r_f	Reduction factor
ρ	Density
RMS	Root Mean Square
SAR	Successive Approximation Register

SM	Standard Model of particle physics
Sn	Tin (element)
TBTF	Too-Big-To-Fail
t_{flattop}	Flat top time of trapezoidal filter
t_{rise}	Rise time of trapezoidal filter
$U_{e\mathrm{i}}$	Elements of PMNS matrix U with electron flavor
V	Voltage
WDM	Warm Dark Matter
WGTS	Windowless Gaseous Tritium Source
y_{D}	Yukawa coupling constant
Z	Atomic number

1 Neutrinos

A short review on neutrinos from their discovery until today is presented in this chapter. Section 1.1 focuses on properties of neutrinos and describes fundamental experimental mile stones in the history of neutrino physics, which opened the door to physics beyond the Standard Model (SM). In section 1.2 the existence of so-called *sterile neutrinos* is motivated from both particle physics and cosmology views. Finally, sterile neutrinos in the mass range of a few keV [1] are presented to be a promising Dark Matter (DM) candidate.

1.1 Active neutrinos

Active neutrinos were discovered in the 1930s and were assumed to be massless particles within the Standard Model of particle physics. Only about 70 years later detections of neutrino oscillations proved non-zero neutrino masses.

1.1.1 Discovery of the neutrino

In 1930 Wolfgang Pauli postulated the existence of a very light and neutral particle which could explain observations of continuous β-spectra, discovered by James Chadwick in 1914 [2]. Unlike in the case of α-decays, where monoenergetic α particles were observed and understood, the continuity of measured β-spectra was a long-standing miracle. Pauli's invented particle, he called it *neutron*, explained the measured spectra and saved the fundamental law of energy conservation. Pauli predicted these *neutrons* to have a small mass of the order of the electron mass and to be a spin 1/2 particle. In a letter of the year 1930 Pauli explains his idea of this new particle to scientists in Tübingen, Germany. An extract is shown in figure 1.1. In 1933 Enrico Fermi established the theory of β-decay via weak interaction and called the postulated particle *neutrino*, i.e. the *small neutron*. The 'real' neutron had been discovered by the time by James Chadwick.

1 The speed of light c is set to unity in this thesis. In SI units the mass is given in units of $\frac{\text{keV}}{c^2}$.

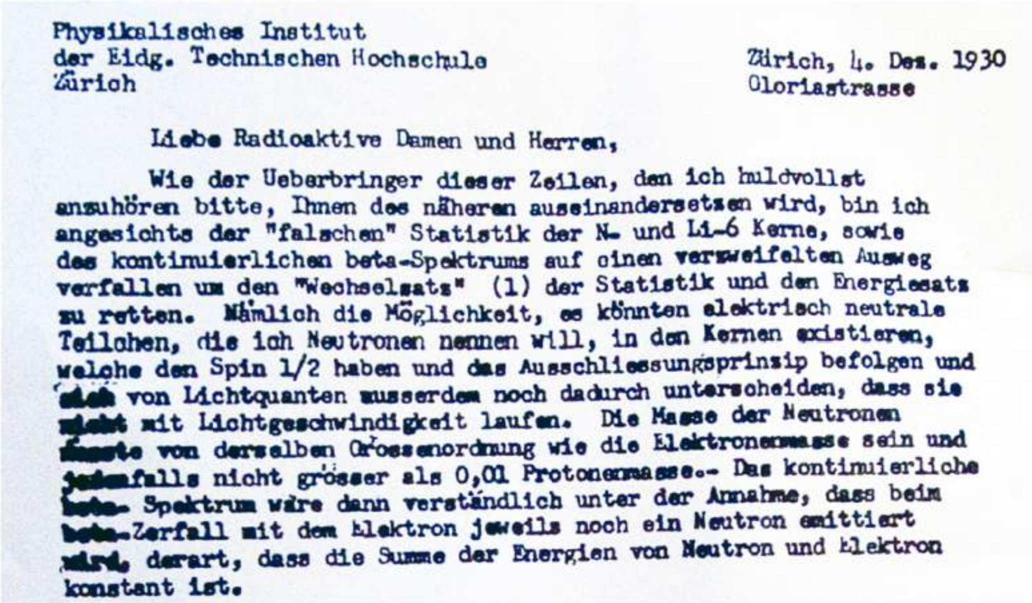

Physikalisches Institut
der Eidg. Technischen Hochschule
Zürich

Zürich, 4. Dez. 1930
Gloriastrasse

Liebe Radioaktive Damen und Herren,

Wie der Ueberbringer dieser Zeilen, den ich huldvollst anzuhören bitte, Ihnen des näheren auseinandersetzen wird, bin ich angesichts der "falschen" Statistik der N- und Li-6 Kerne, sowie des kontinuierlichen beta-Spektrums auf einen verzweifelten Ausweg verfallen um den "Wechselsatz" (1) der Statistik und den Energiesatz zu retten. Nämlich die Möglichkeit, es könnten elektrisch neutrale Teilchen, die ich Neutronen nennen will, in den Kernen existieren, welche den Spin 1/2 haben und das Ausschliessungsprinzip befolgen und sich von Lichtquanten ausserdem noch dadurch unterscheiden, dass sie nicht mit Lichtgeschwindigkeit laufen. Die Masse der Neutronen müsste von derselben Groessenordnung wie die Elektronenmasse sein und jedenfalls nicht grösser als 0,01 Protonenmasse.- Das kontinuierliche beta- Spektrum wäre dann verständlich unter der Annahme, dass beim beta-Zerfall mit dem Elektron jeweils noch ein Neutron emittiert wird, derart, dass die Summe der Energien von Neutron und Elektron konstant ist.

Figure 1.1: Letter from Wolfgang Pauli to German physicists from 1930, in which he postulates a new neutral particle, resolving the energy conservation issue in the observed β-spectra [3].

In β-decay, a neutron decays to a proton and emits an electron and an electron anti-neutrino, as described in equation 1.1. Figure 1.2 shows a historic plot of a continous β-decay spectrum from the year 1935, the associated Feynman graph is displayed in figure 1.3

$$n \to p + e^- + \bar{\nu}_e \tag{1.1}$$

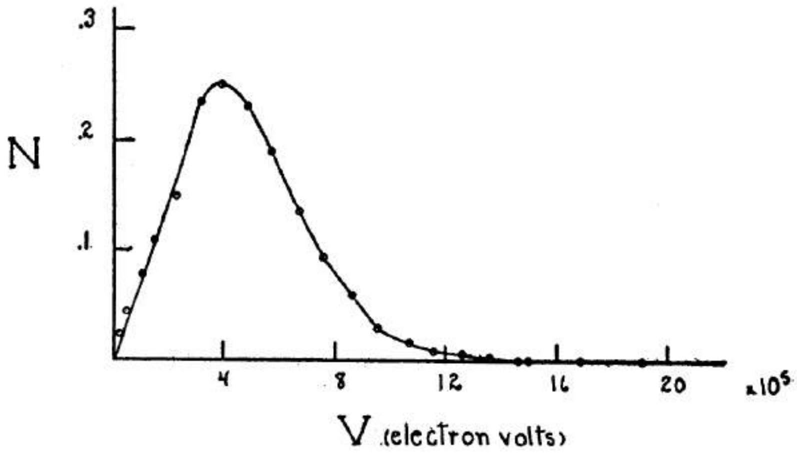

Figure 1.2: Continuous β-decay spectrum of Radium E, published in 1935 [4].

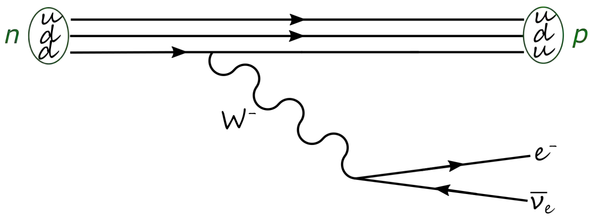

Figure 1.3: Feynman diagram of single β-decay (This way of representation was introduced in 1948 by R. Feynman).

The first experimental evidence for the existence of neutrinos was given by Reines and Cowan [5] in 1956 by the detection of inverse β-decay, where an anti-neutrino interacts with a proton to create a neutron and a positron. Reines and Cowan derived a neutrino mass limit $m_\nu < \frac{1}{500} m_e \approx 1$ keV, where m_e denotes the electron mass.

1.1.2 Neutrinos in the Standard Model

The Standard Model (SM) of particle physics entails three neutrino flavours (ν_e, ν_μ and ν_τ), belonging to the three lepton generations (e, μ, τ). In the SM neutrinos are assumed to be massless and only left-handed. Figure 1.4 shows the SM fermions with their respective masses.

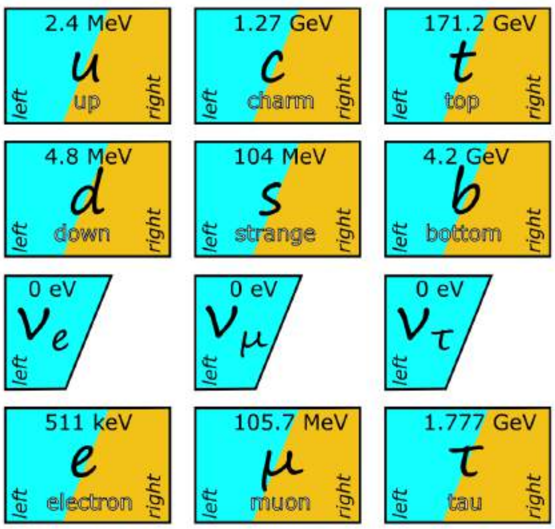

Figure 1.4: Fermions in the Standard Model of particle physics. All fermions appear as left- and right-handed particles except the neutrinos. In the SM they are considered to be massless and no right-handed component is foreseen.

Every fermion appears as a left- and right-handed particle, except the neutrinos, which only have a left-handed component. A right-handed neutrino would not carry any charge and hence would not interact at all (not even weakly like its left-handed partner). Without its right-handed partner, neutrinos cannot form a Dirac mass term like all the other fermions of the SM, which coincides with the assumption of massless neutrinos.

1.1.3 Neutrino oscillations

In the 1960s, experiments started to detect solar and atmospheric neutrinos. The standard solar model predicts a neutrino energy spectrum resulting from fusion processes inside the sun [6]. Radio-chemical experiments like the *Homestake* experiment were launched to prove the predicted energy spectra via inverse β-decay and a following electron capture [7]. The experimental results showed a solar neutrino flux which was about a factor of three lower than the predicted flux. The results were confirmed by *GALLEX* [8], *SAGE* [9] and *Super-Kamiokande* [10].
This phenomenon is known as the *solar neutrino problem* [11]. In the year 2000 the *SNO* experiment was able to resolve the problem, by allowing a measurement of all neutrino flavours via neutral current (NC) interactions [12]. The measured neutral current rate, measured by the *SNO* experiment, was in agreement with the standard solar model predictions. It confirmed that the total neutrino flux is conserved, but only the neutrino flavour changes on its way from the sun to the earch, such that it cannot be detected via a neutral current (CC) interaction.

This phenomenon, called neutrino oscillations, was further confirmed by experiments with atmospheric neutrinos (e.g. *Super-Kamiokande* [13], see figure 1.5), reactor neutrinos (e.g. *Daya Bay* [14]) and accelerator neutrinos (e.g. *T2K* [15]).
Neutrino oscillations stem from the fact that neutrinos are produced in flavour eigenstates (ν_e, ν_μ, ν_τ) of the weak interaction, but propagate as mass eigenstates ν_1, ν_2, ν_3. The mass eigenstates travel with different velocities due to their mass differences and thus experience different time evolutions. Analog to the quark mixing, a neutrino mixing matrix, the PMNS matrix [2] U, can be introduced which shows the relation between flavour and mass eigenstates [17, 18].

$$\begin{pmatrix} \nu_e \\ \nu_\mu \\ \nu_\tau \end{pmatrix} = \underbrace{\begin{pmatrix} U_{e1} & U_{e2} & U_{e3} \\ U_{\mu 1} & U_{\mu 2} & U_{\mu 3} \\ U_{\tau 1} & U_{\tau 2} & U_{\tau 3} \end{pmatrix}}_{U} \begin{pmatrix} \nu_1 \\ \nu_2 \\ \nu_3 \end{pmatrix} \tag{1.2}$$

A neutrino flavour eigenstate ν_α ($\alpha = e, \mu, \tau$) can therefore be written as a weighted

2 The matrix was introduced by the scientists *Pontecorvo*, *Maki*, *Nakagawa* and *Sakata*.

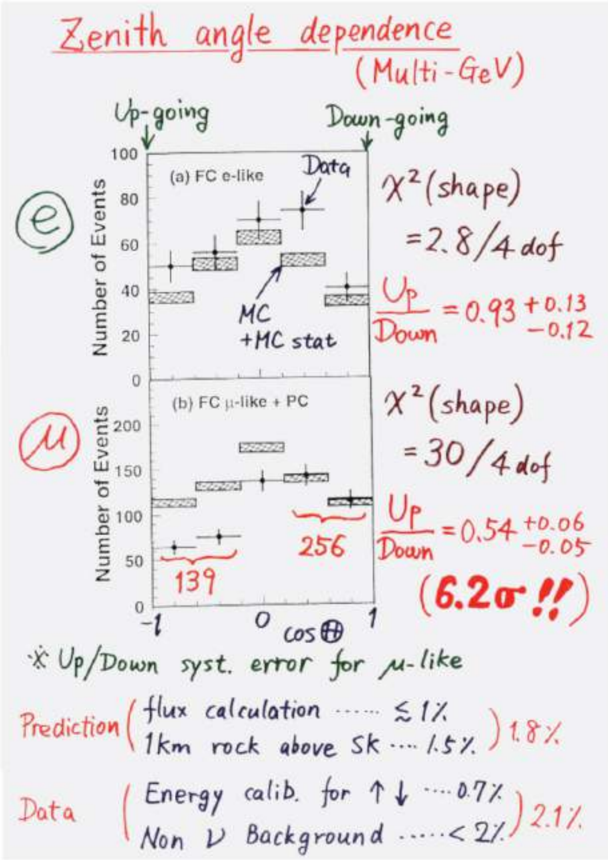

Figure 1.5: Historic slide from Takaaki Kajita (1998) presented at the *Neutrino 98* conference in Japan [16]. It proves neutrino oscillations of atmospheric ν_μ measured with *Super-Kamiokande*. In the graphs, the number of detected events is plotted against $\cos\theta$, where θ denotes the incident angle of the neutrino. The number of μ-like neutrinos coming down from the atmosphere was in agreement with the expectation. However the flux of μ-like neutrinos, which originate from the other side of the earth and have travelled through the entire earth before reaching the detector, was almost a factor of two smaller than expected. This was a clear evidence (6.2 σ) of neutrino oscillations.

superposition of the three mass eigenstates ν_1, ν_2, ν_3:

$$|\nu_\alpha\rangle = \sum_{j=1}^{3} U_{\alpha j} \left|\nu_j\right\rangle . \tag{1.3}$$

In a two-flavour case the probability of a neutrino, produced in flavour eigenstate α and detected in flavour eigenstate β, is given by

$$P_{\alpha\to\beta} = \sin^2(2\vartheta)\sin^2\left(\frac{1.27\Delta m^2[\mathrm{eV}^2]L[\mathrm{km}]}{E_\nu[\mathrm{GeV}]}\right), \tag{1.4}$$

where E_ν denotes the neutrino energy, ϑ is the mixing angle between the flavour eigenstates, Δm^2 the difference of squared masses of the mass eigenstates. L gives the length of the travel path. The oscillation probability depends on the masses of the mass eigenstates. If neutrinos were massless, then $\Delta m^2_{ij} = m_i^2 - m_j^2 = 0$ ($i, j = 1, 2, 3$ in the three-flavour case) and oscillations would not occur.
"For the discovery of neutrino oscillations, which shows that neutrinos have mass" [19] and thus for the first physics beyond the Standard Model, the *Nobel Prize in*

Physics 2015 was given to Takaaki Kajita (*Super-Kamiokande*) and Arthur McDonald (*SNO*).

1.1.4 Neutrino mass measurements

While oscillation experiments give information on Δm_{ij}^2 and the respective mixing angles ϑ_{ij}, they do not provide information on the absolute neutrino mass scale. The latter is accessible through the investigation of the kinematics of β-decays.

Single β-decay

In single β-decays with tritium an electron and an electron anti-neutrino are released. The maximum kinetic energy an electron can get, depends on the neutrino mass and is shifted to lower energies for a non-zero mass. The current best limit [20] on the effective electron anti-neutrino mass is set to

$$m_{\nu_e} = \sqrt{\sum_i m_i^2 |U_{ei}|^2} \leq 2.3 \text{ eV } (95\% \text{ C.L.}), \tag{1.5}$$

which is expected to be surpassed by the KArlsruhe TRItium Neutrino (KATRIN) experiment [21]. KATRIN is designed to reach a sensitivity of

$$m_{\nu_e} \leq 0.2 \text{ eV } (90\% \text{ C.L.}). \tag{1.6}$$

Double β-decay

Another approach to measure the absolute neutrino mass is the search for neutrinoless double β-decay ($0\nu\beta\beta$). This second-order weak interaction process is forbidden in the SM due to the associated lepton number violation $\Delta L = 2$ and is only possible if the neutrino is a *Majorana* particle, i.e. $\nu = \overline{\nu}$.
A nucleus with mass number A and atomic number Z decays to a nucleus with atomic number $Z + 2$. Two electrons are emitted as well as an anti-neutrino $\overline{\nu_R}$ which, emitted by a neutron decay, gets absorbed as a neutrino ν_L by another neutron.

$$(A, Z) \rightarrow (A, Z + 2) + 2e^- \tag{1.7}$$

The Feynman diagram is shown in figure 1.6.

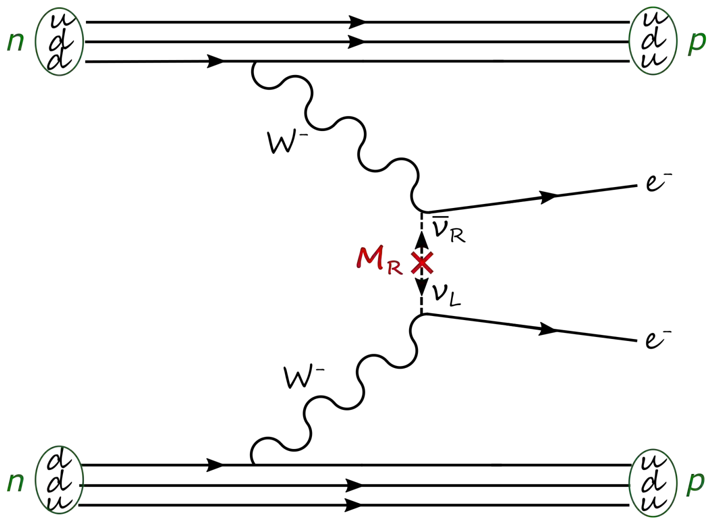

Figure 1.6: Feynman diagram of neutrinoless double β-decay. If neutrinos are Majorana particles (i.e. there is a Majorana mass $M_R \neq 0$), a right-handed anti-neutrino can be absorbed as a left-handed neutrino within the nucleus.

Current experiments with ^{76}Ge (e.g. *GERDA* [22]), ^{136}Xe (*KamLAND-Zen* [23]) or ^{130}Te (*CUORE* [24]) set a mass limit on the effective *Majorana* mass m_{ee}

$$m_{ee} = \left| \sum_i m_i U_{ei}^2 \right| \leq 0.2 - 0.4 \text{ eV } (90\% \text{ C.L.}) \tag{1.8}$$

Note the different effective neutrino masses which can be determined by single and double β-decay experiments (equations 1.5 and 1.8).

1.2 Sterile neutrinos

One natural way to introduce non-zero neutrino masses into the Standard Model is by introducing right-handed (right-chiral) neutrinos[3]. They are $SU(2)$ x $U(1)$ singlets and unlike active neutrinos do not even take part in the weak interaction. Therefore they are called *sterile*. However, sterile neutrinos can mix with active neutrinos.

In this paragraph, a motivation for sterile neutrinos from a particle physics point of view is given which implies a way to explain the masses of active neutrinos and elaborates on the *Dirac* or *Majorana* nature of neutrinos. Moreover, a cosmological motivation for sterile neutrinos and limits on the sterile neutrino mass and mixing angle are presented.

3 The introduction of right-handed neutrinos is a straightforward way to introduce a neutrino mass, however, it is not the only possible way. Neutrino masses can also be introduced by an extension of the scalar sector [25, 26].

1.2.1 Motivation from particle physics

The introduction of right-handed neutrinos is a natural way to explain the non-zero mass of active neutrinos [27]. It can be used to give mass to neutrinos via the Higgs mechanism, requiring a Dirac mass m_D term for neutrinos. The mass is obtained by a transition from left (ν_L) to right-chiral states (ν_R) as shown in figure 1.7.
The process is described by the Lagrangian

$$\mathcal{L}_D = -m_D(\overline{\nu}_L \nu_R + \overline{\nu}_R \nu_L). \tag{1.9}$$

The Dirac mass m_D is given by

$$m_D = y_D \left\langle \Phi^0 \right\rangle, \tag{1.10}$$

where $\langle \Phi^0 \rangle$ is the Higgs vacuum expectation value.

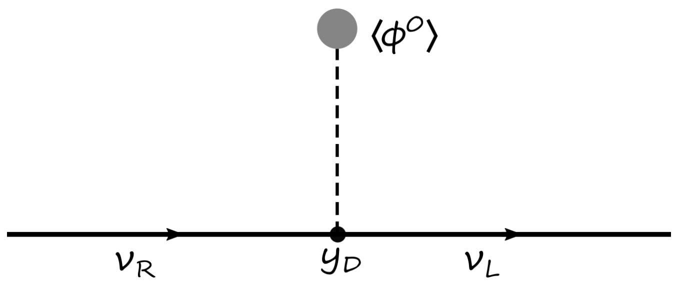

Figure 1.7: A Dirac mass term of neutrinos with a Yukawa coupling y_D to the Higgs vacuum expectation value $\langle \Phi^0 \rangle$ requires right-handed neutrinos ν_R.

In this scenario, a tiny Yukawa coupling constant of the order of $y_D \leq 10^{-11}$ is required to be consistent with current limits on the neutrino mass. This is five orders of magnitude smaller than for the electron.

A second possibility to explain neutrino masses, avoiding this unnaturally small Yukawa coupling, is to introduce *Majorana* mass terms M_R for the right-handed neutrinos. Such a mass term is allowed since right-handed neutrinos are singlets under the SM gauge group and hence it does not violate any gauge symmetry. M_R can be of arbitrary scale, which is in no way connected to the Higgs mechanism. The resulting Lagrangian is given by

$$\mathcal{L}_M = \frac{1}{2} M_R (\overline{\nu}_R \nu_R^c + \overline{\nu}_R^c \nu_R), \tag{1.11}$$

where the exponent c denotes the CP-conjugate of the respective fields. Majorana mass terms of this kind are allowed by gauge symmetry of the Standard Model, however they violate lepton number conservation.

If $M_R \neq 0$, neutrinos are Majorana particles. If $m_D = 0$, neutrinos are a pure Majorana neutrinos with arbitrary mass and no SM interactions. If $M_R = 0$ the neutrino is a pure Dirac particle with a tiny Higgs-Yukawa coupling. For $m_D \neq 0$ and $M_R \neq 0$, predictions on the respective neutrino masses can be made by the see-saw mechanism.

See-saw mechanism

The see-saw mechanism model [28, 29] gives an explanation for the small active neutrino masses, including a heavy Majorana mass term M_R comparable to the GUT-scale.
In this model the neutrino mass matrix M is given by

$$M = \begin{pmatrix} 0 & M_D \\ M_D^T & M_R \end{pmatrix} \tag{1.12}$$

in the basis $\Psi = (\nu_{a,1} \ldots \nu_{a,n_a} \, \nu_{s,1} \ldots \nu_{s,n_s})$ following the notation in [30]. Here n_a is the number of active neutrinos, n_s the number of sterile neutrinos and M is an (n, n) matrix with $n = n_a + n_s$. $''0''$ is a (n_a, n_a) null matrix, M_D is a (n_a, n_s) Dirac mass matrix with entries in the magnitude of the electro-weak scale and M_R denotes the (n_s, n_s) Majorana mass matrix with entries of a high-energy scale like the GUT scale. For $n_a = n_s = 1$, M is a simple $(2, 2)$ matrix with the eigenvalues

$$\lambda_1 \approx M_R \tag{1.13}$$
$$\lambda_2 \approx \frac{-M_D^2}{M_R}. \tag{1.14}$$

One of the eigenvalues, i.e. the physical neutrino masses, is proportional to the heavy Majorana mass M_R, the other one is inverse proportional to M_R. With a very heavy Majorana mass scale, equation 1.14 provides an explanation for the smallness of active neutrino masses (λ_2 is small for large M_R).

Possible masses of sterile neutrinos

In principle there are no restrictions on the allowed Majorana mass M_R, as M_R is a new and independent mass scale. The following listing gives a short overview on different mass regions, motivated by various experiments and models.

- $M_R = \mathcal{O}(\text{eV})$
  Sterile neutrinos in this mass region[4] can contribute to solve tensions in the results of short-baseline neutrino oscillation experiments, such as the so-called reactor anomaly by oscillations from active to sterile neutrinos [31, 32].

- $M_R = \mathcal{O}(\text{keV})$
  From a cosmological point of view, sterile neutrinos in the mass range of a few keV are a promising Cold and Warm Dark Matter (CDM and WDM) candidate. WDM is in agreement with cosmological observations from small to large scales and has the potential to solve tensions of purely CDM scenarios in the description of of very small scales (<10 kps) in the universe [33]. More details are given in section 1.2.2.

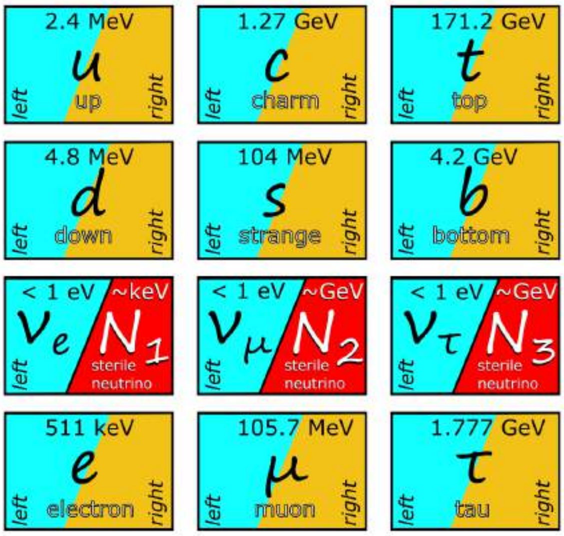

Figure 1.8: Fermions in the Neutrino Minimal Standard Model (νMSM). All fermions appear as left and right-handed particles. One sterile neutrino ($N1$) has a keV mass to account for Dark Matter, the two other sterile neutrinos ($N2$, $N3$) have masses in the range of GeV to explain baryon asymmetry via oscillation induced leptogenesis [34]. In the νMSM, one of the active neutrinos has to be very light $m_1 \lesssim \mathcal{O}(10^{-6})$ eV, the other two are fixed to $m_2 \simeq 9 \cdot 10^{-3}$ eV and $m_3 \simeq 5 \cdot 10^{-2}$ eV for normal hierarchy and $m_{2,3} \simeq 5 \cdot 10^{-2}$ eV for inverted hierarchy.

- $M_R = \mathcal{O}(\text{GeV})$
  A minimal extension of the SM with three sterile neutrinos ($N1$, $N2$, $N3$) in the mass range of keV, GeV and GeV, the Neutrino Minimal Standard Model,

4 Strictly speaking the sterile neutrino is not a mass eigenstate. Here a sterile neutrino of a given mass refers to the corresponding new mass eigenstate that is mostly composed of the sterile neutrino type.

νMSM [1], provides both a DM candidate (keV) and explains baryon asymmetry with two nearly degenerate sterile neutrinos in the GeV range. The fermions in the νMSM are shown in figure 1.8.

- $M_R \approx M_P$
  Sterile neutrinos could have masses up to the Planck scale $M_P \approx 10^{19}$ GeV. For large M_R, the see-saw mechanism can explain the tiny active neutrino masses.

1.2.2 Motivation from cosmology

Only 5% of the entire energy density in the universe comes from baryonic matter. Around 25% originates from Dark Matter, the rest is named Dark Energy. However, at the moment it is not known what the latter two consist of.
Many theories provide ideas on the constituents of DM, the most prominent are so-called WIMPS (*weakly interacting massive particles*), which are favoured by the current standard model of cosmology, ΛCDM (Λ is Einstein's cosmological constant). This model agrees with cosmological observations at large scales from gigaparsecs to megaparsecs. Though, tension arises when looking at small structures which can be mitigated by *sterile neutrinos* in the mass range of a few keV. These tensions are namely the *missing dwarf galaxies*, the *cusp-core problem* and the *too-big-to-fail* issue. They are shortly discussed below, a detailed overview can be found in [27].

Missing dwarf galaxies

On a large scale, CDM and WDM scenarios predict similar structures and are both in good agreement with cosmic microwave background observations and galaxy clustering tests. However, the number of observed dwarf galaxies is significantly smaller than the predicted number in ΛCDM simulations. In contrast to this, WDM scenarios have a different primordial power spectrum which leads to a suppression for small scales [35]. Only a few dwarf galaxies are present in WDM simulations and the results correspond to the experimental observations [36].
Figure 1.9 shows N-body simulations of galactic halos in CDM and WDM scenarios with a sterile neutrino mass $m_s = 2$ keV and illustrates the suppression power for small structures in the WDM case due to the larger free-streaming length.

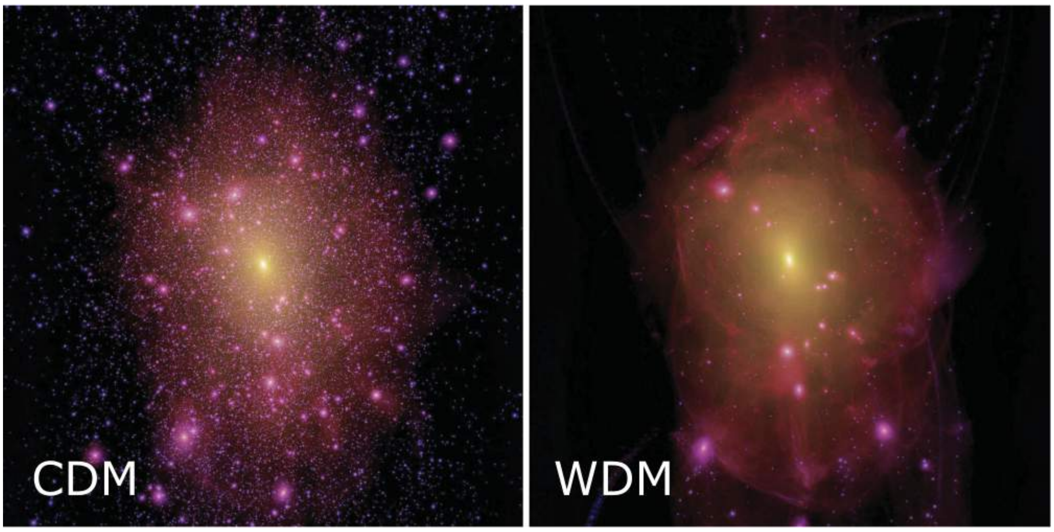

Figure 1.9: N-body simulations of WDM and CDM subhalos [37]. The number of small structures is lower in the case of WDM. This is in good agreement with observations.

Cusp-core problem

With respect to density profiles of low-mass galaxies, ΛCDM simulations predict a cusp power law $\rho \approx r^{-\alpha}$ with $\alpha \approx -1$ [38]. The density increases for small radii. Experimental data of dwarf galaxy rotation curves, however, match core-like models with $\alpha \approx -0.3$, favouring a more flat (core) density profile. The density distribution directly affects the rotation curves and measurements of the rotation curves yield information on α. Figure 1.10 shows the rotation velocity of the F568-3 galaxy and compares it to cusp and core density profiles.

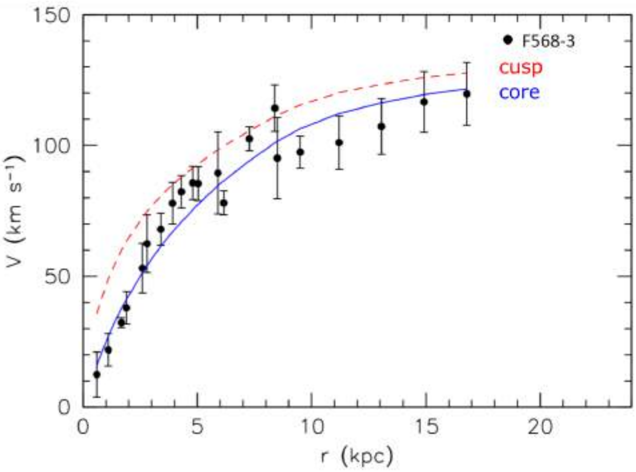

Figure 1.10: Cusp-core problem. Rotation velocity data of galaxy F568-3 compared to models with a cusp (CDM) and core (WDM) densitity profile. For the inner radii, the cusp model predictions are too high by a factor of two or more [39].

With WDM instead of CDM, cores would naturally be produced, as for WDM the phase space density is finite and a steep increase of density for small radii is excluded [27, 40].

Too-big-to-fail

The *too-big-to-fail* issue (TBTF) is strongly related to the *missing dwarf galaxies* and *cusp-core-problem*. It states the difficulty to explain both the number density of dwarf galaxies and their internal kinematics within ΛCDM and combines the issues mentioned above:
To explain the number of observed dwarf galaxies, they need to be in massive halos. However, such massive halos would show different kinematics than measurements demonstrate. Vice versa, in order to match the observed kinematics of dwarf galaxies, they are requested to be situated in low-mass halos. In this case however, way more dwarf galaxies are predicted in the ΛCDM model than experimental data provide [41].
WDM can provide a solution to the TBTF problem, suppressing low-mass halos in a WDM universe and decreasing the halo concentration.

1.2.3 The 3.5 keV candidate Dark Matter decay signal

A possible hint for a sterile neutrino with mass $m_s \approx 7$ keV and $\sin^2(2\vartheta) \approx 10^{-11}$ was seen in a stacked XMM Newton (X-ray observatory) spectrum of 73 galaxy clusters [42]. An unidentified weak emission line at $E \approx 3.55$ keV was detected with approximately 4σ which could origin from the decay of a sterile neutrino with mass $m_s = 2E_\gamma \approx 7.1$ keV. Figure 1.11 shows the corresponding Feynman diagram.

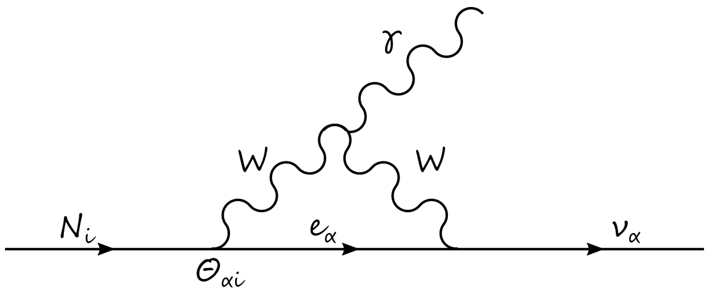

Figure 1.11: Feynman diagram of the radiative decay of a sterile neutrino N_i to an active neutrino ν_α and a photon γ. The photon has half the energy of the sterile neutrino mass $E_\gamma = \frac{1}{2}\, m_s$.

Figure 1.12 shows the 3.5 keV line in the experimental data of the XMM-Newton radio telescope as well as the simulated line as it would be observed by the recently launched X-ray satellite *Astro-H*.

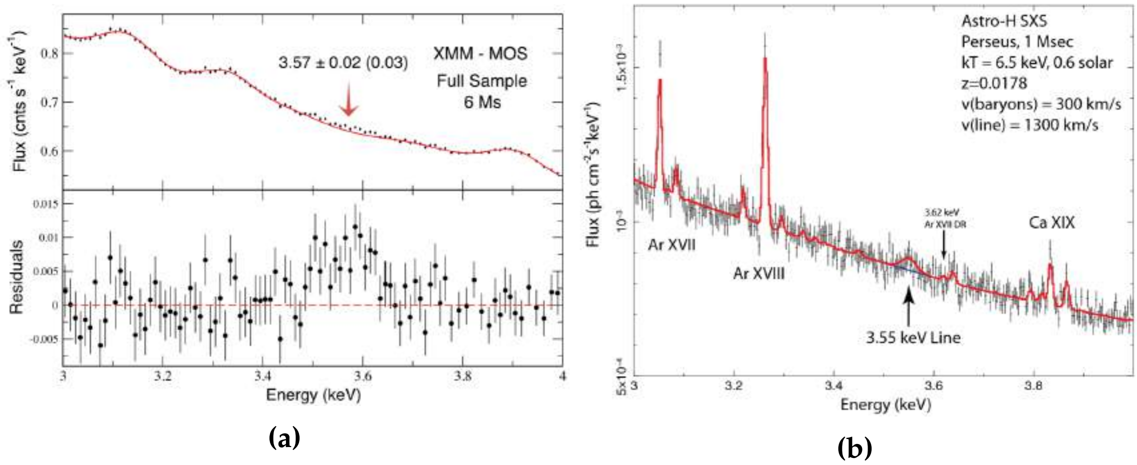

Figure 1.12: (a) XMM-Newton data between 3 and 4 keV show an emission line at ≈ 3.5 keV. **(b)** Astro-H simulations of the Perseus cluster with a 3.55 keV line. Both plots are taken from [42].

However, these results are highly controversial. The line could be compatible with the atomic emission line from K XVIII or with systematic uncertainties due to the complicated instrumentation. Moreover, non-trivial telescope responses may have a large influence. The analysis of the same data by different groups is not consistent, some confirm the line [43], some see no line and exclude it with more than 5σ [44]. Even if the line exists, further investigations are required to determine its origin.

1.2.4 Constraints

Several constraints apply to the parameter space of sterile neutrinos due to observations and DM simulations. The current status is shown in figure 1.13.

- **Tremaine-Gunn bound:** The Tremaine-Gunn bound provides a lower bound for a fermionic DM mass of $m_s > 1$ keV, based on limits on the phase-space density. The phase-space density of fermionic DM should be smaller than the density of degenerate Fermi gas [40].
- **Lyman-α forest:** The Lyman-α forest sets a lower bound on the DM particle mass. It describes the $n = 2 \rightarrow n = 1$ transition in hydrogen at $\lambda = 121.6$ nm of neutral hydrogen clouds in the intergalactic medium along a line-of-sight to a source far away, e.g. as quasar. Depending on the redshift z, caused by the expansion of the universe, the observed wavelength λ_{obs} varies:

$$\lambda_{\text{obs}} = (1 + z)\lambda. \tag{1.15}$$

The absorption lines in the resulting Lyman-α forest give a limit on the free-streaming length λ_{FS} of DM particles. The warmer the WDM particle, the larger is λ_{FS} and the less structure appears on small scales.
The free-streaming length in principle can be converted to a lower mass bound, however the relation strongly depends on the production mechanism of sterile neutrinos in the early universe. Moreover the bound only accounts if sterile neutrinos constitute 100% of DM [45].

- **Exclusion by X-ray observations:** The upper right corner in figure 1.13 is excluded by the non-observation of monoenergetic X-ray lines in the decay of sterile neutrinos $N \to \nu\gamma$. Also this bound assumes that all DM is made of sterile neutrinos [46].

- **DM overproduction and underproduction:** For large mixing angles, the parameter space is excluded by DM overproduction which contradicts observations. If the mixing angle is very small, the amount of produced DM would be to small in models like νMSM.

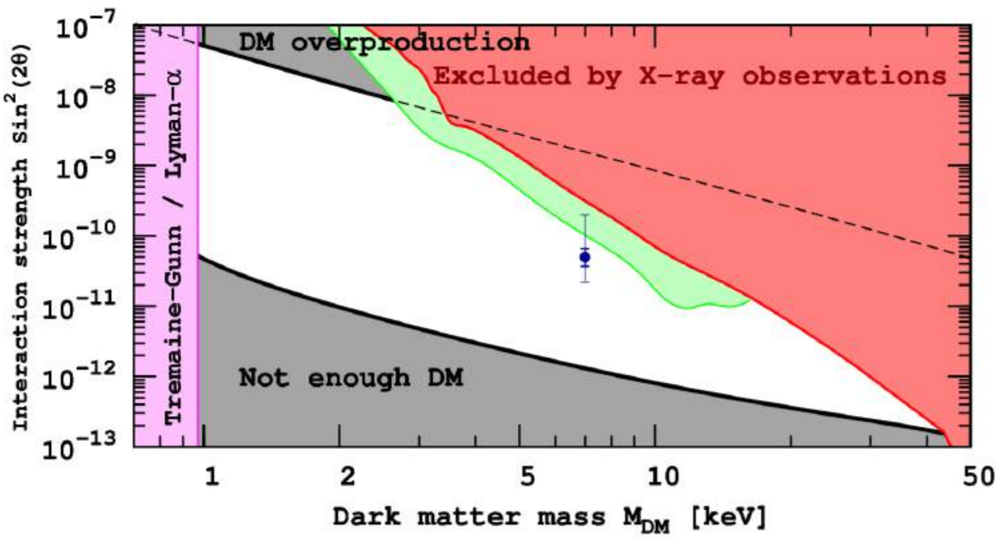

Figure 1.13: Constraints on the mass and mixing angle of sterile neutrinos [46]. The white region is the allowed region for the case that sterile neutrinos constitute 100% of DM. The grey regions are excluded as too much (or not enough respectively) DM would be produced in this parameter region. Small masses < 1 keV are excluded by the Lyman-α constraints and the Tremaine-Gunn limit. The upper right corner is excluded due to the non-observation of monoenergetic X-ray lines from sterile neutrino decays, the green area shows additional recent bounds from X-ray non-observations [47]. The blue dot corresponds to the unidentified 3.5 keV emission line in stacked galaxy clusters.

2 KATRIN

The KATRIN (KArlsruhe TRItium Neutrino) experiment at Karlsruhe Institute of Technology (KIT) is designed to measure the effective electron neutrino mass

$$m_{\nu_e} = \sqrt{\sum_i m_i^2 |U_{ei}|^2} \tag{2.1}$$

with a sensitivity of 200 meV at 90% C.L. by β-spectroscopy of tritium decay [21]. A schematic overview of the entire KATRIN beamline is illustrated in figure 2.1.

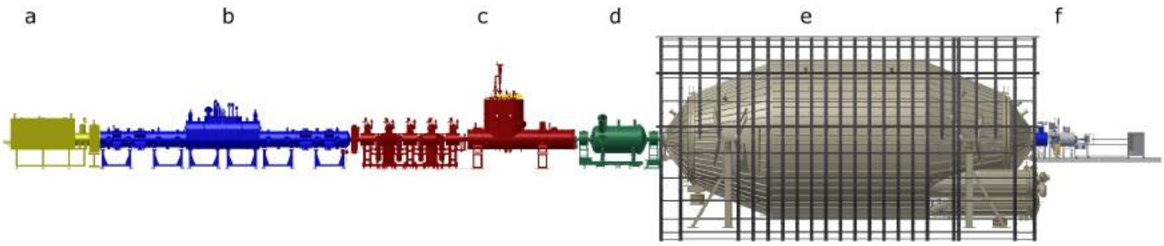

Figure 2.1: 70 m beamline of the KATRIN experiment with rear section (a), windowless gaseous tritium source (b), differential and cryogenic pumping section (c), pre-spectrometer (d), main spectrometer (e) and focal plane detector (f).

Section 2.1 gives an experimental overview on the KATRIN experiment as it is designed for the determination of the neutrino mass. Section 2.2 focuses on using KATRIN to search for sterile neutrinos with a mass in the range of a few keV and addresses the necessary future KATRIN modifications for this purpose.

2.1 Design KATRIN mode

The basic KATRIN idea is to measure the kinetic energy of electrons emitted in tritium β-decay. Tritium decays to ^{3}Helium, an electron and an electron anti-neutrino (equation 2.2). The released decay energy is shared between the latter two, resulting in a continuous β-spectrum, displayed in figure 2.2.

$${}^3_1\mathrm{H} \rightarrow {}^3_2\,\mathrm{He}^+ + e^- + \overline{\nu}_e \tag{2.2}$$

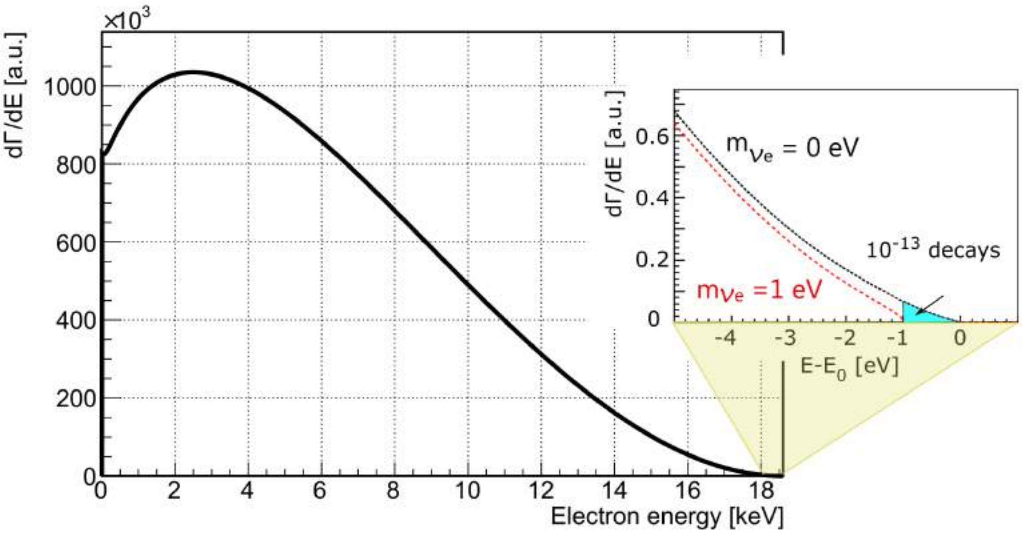

Figure 2.2: Differential tritium β-decay spectrum. The endpoint energy E_0 depends on the neutrino mass m_{ν_e}.

The maximum kinetic energy an electron can get depends on the neutrino mass and is shifted to lower energies for a non-zero mass. KATRIN is designed to analyze the spectrum shape in a region close to the endpoint where the impact of the neutrino mass is maximal.

2.1.1 Windowless gaseous tritium source

KATRIN uses a windowless gaseous tritium source (WGTS) with a very high activity of 10^{11} decays per second and a stability at the level of 10^{-3} [48]. It provides a throughput of 40 g/day and a tritium purity $> 95\%$ which is continuously monitored via Raman spectroscopy [49]. The beam-tube is kept at a temperature of 30 K with a stability of 0.1% [50]. The WGTS, shown in figure 2.3, was finalized and delivered to KIT in September 2015, being the last big missing component of the KATRIN setup.
Tritium has several advantages for β-decay investigations: Tritium decay has a rather short lifetime of $T_{1/2} = 12.3$ years which offers a high count rate for low source densities. The transition ${}^3_1\text{H} \rightarrow {}^3_2$ He is superallowed and its matrix element does not depend on the energy. Moreover tritium appears as a molecule (T_2) with a rather simple internal structure which makes computations easier compared to most other molecules.

Figure 2.3: Fisheye picture of the windowless gaseous tritium source (WGTS) inside the Tritium Laboratory Karlsruhe with the transport section on the right [51].

2.1.2 Transport section

The differential and cryogenic pumping sections (DPS and CPS) operate as a crucial tritium retention system and reduce the tritium flow by 14 orders of magnitude. The DPS contains four turbomolecular pumps to reduce the tritium flow. Moreover, dipole electrodes and Fourier transformation ion cyclotron resonators are built in the DPS section to remove and analyze positive ions [52].
In the cryogenic pumping section, remaining tritium is trapped by cryo-sorption on argon frost at 3 K [53]. Figure 2.4 shows pictures of the DPS inside the Tritium Laboratory Karlsruhe and the delivery of the CPS.

(a) **(b)**

Figure 2.4: **(a)** Differential pumping section with its five cylindrical magnets. The beam tube is still not complete in this picture. **(b)** Arrival of the CPS at KIT in Juli 2015 [54].

2.1.3 Spectrometers

There are three spectrometers in the KATRIN setup. The *pre-spectrometer* is designed to reject a large fraction of low-energy decay electrons which provide no information on the neutrino mass [55]. The *monitor spectrometer* monitors the voltage stability of the main spectrometer, using monoenergetic conversion electrons from ^{83}Kr decays [56].

The *main spectrometer* is the most prominent component of the KATRIN experiment. It operates as MAC-E filter, see figure 2.5, and combines Magnetic Adiabatic Collimation with an Electrostatic filter [21].

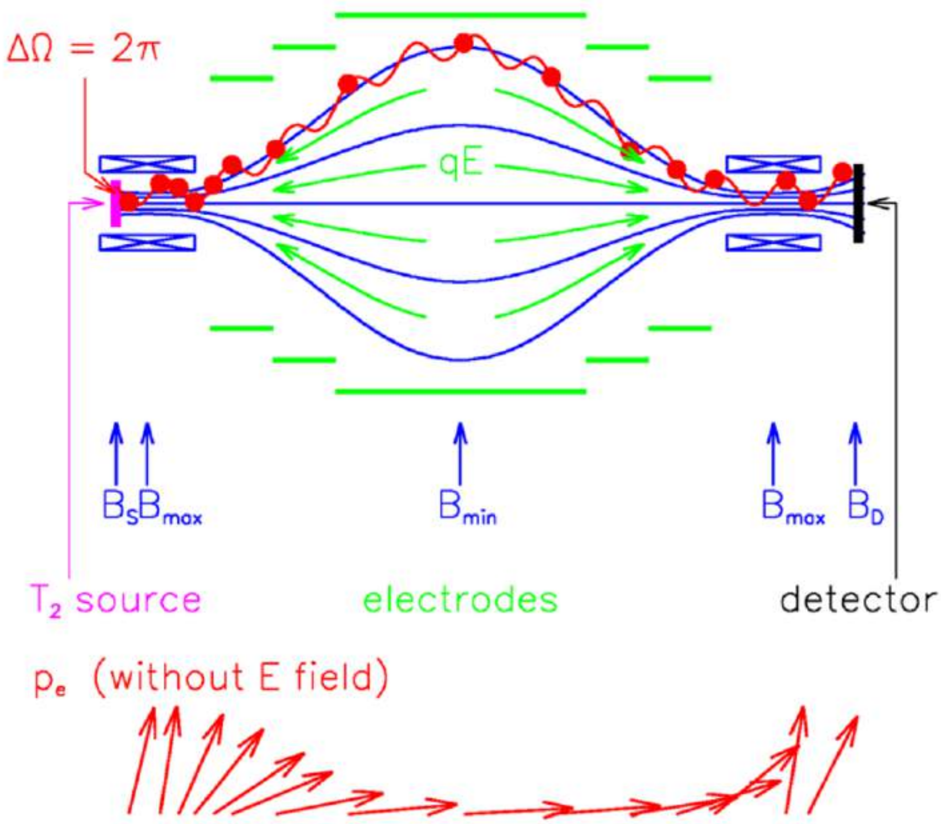

Figure 2.5: Working principle of a MAC-E filter. Electrons, coming from the source, are guided adiabatically by magnetic field lines through the spectrometer, following cyclotron tracks. The magnetic field strongly decreases from $B_{\text{max}} = 6$ T towards the analyzing plane with $B_{\text{min}} = 3 \cdot 10^{-4}$ T in the center of the spectrometer. With decreasing magnetic field, the transversal momentum of the electrons is converted to longitudinal momentum. This provides an ultra-sharp cut-off by the electrostatic filter (< 1 V) and a large acceptance angle at the same time [54].

A negative retarding potential is applied to the main spectrometer, such that only electrons with a higher kinetic energy than this potential can pass and continue their way to the counting focal plane detector. By setting the spectrometer on different potentials, the tritium β-decay spectrum can be scanned in an integral mode. The energy resolution ΔE is given by the ratio of the minimum and maximum magnetic field strength the electrons experience,

$$\frac{\Delta E}{E} = \frac{B_{\text{min}}}{B_{\text{max}}}, \tag{2.3}$$

which yields $\Delta E = 0.93$ eV for $B_{\text{min}} = 3 \cdot 10^{-4}$ T in the analyzing plane and $B_{\text{max}} =$ 6 T for an electron with a kinetic energy of $E = 18.6$ keV.

2.1.4 Focal plane detector

Electrons, which have passed the retarding potential in the main spectrometer, finally reach the focal plane detector system, see figure 2.6. The electrons are guided through the pinch magnet, where they are accelerated by a post-acceleration electrode. Finally they hit the focal plane detector (FPD) which is situated inside the detector magnet.

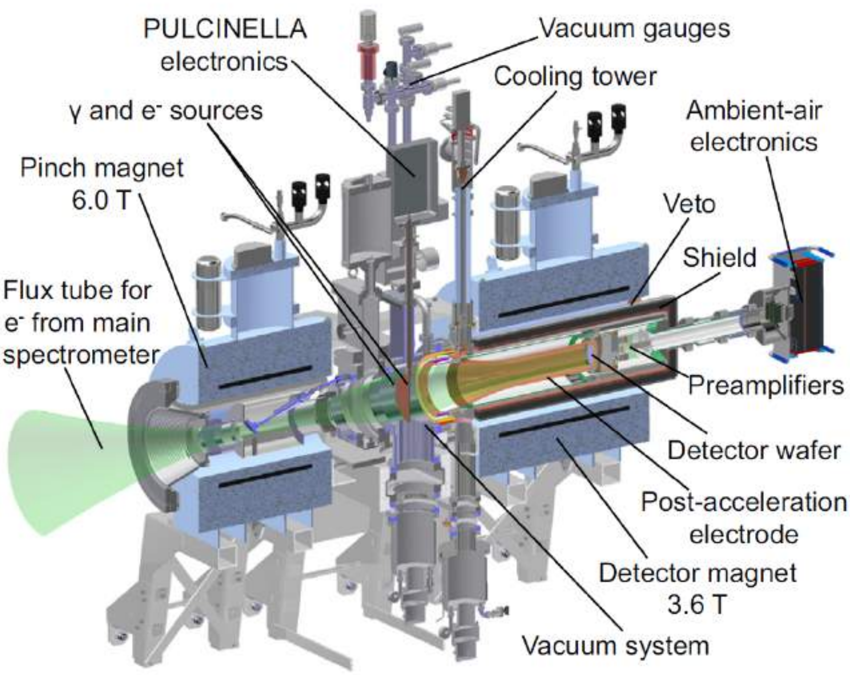

Figure 2.6: Primary components of the FPD system of the KATRIN experiment. The electrons enter the system from the left [57].

Table 2.1: Characterization of the FPD

Detector property	value
Waver thickness	503 μm
Dead layer thickness	$155 \pm 0.5_{\text{stat}} \pm 0.2_{\text{syst}}$ nm
Detection efficiency	$95.0\% \pm 1.8_{\text{stat}}\% \pm 2.2_{\text{syst}}\%$
Energy resolution (FWHM)	1.52 ± 0.01 keV at 18.6 keV
Detector capacity	8.2 pF (design value)
Energy threshold at shaping time 0.8 μs	≈ 8.5 keV
Energy threshold at shaping time 6.4 μs	≈ 4 keV

The FPD is a monolithic silicon p-i-n diode array with 148 p-type pixels and n++ entrance windows [57]. The detector is segmented to account for radial dependencies of the magnetic and electric fields in the main spectrometer in the data analysis. Every pixel covers an area of 44 mm^2, the pixels are grouped into concentric rings, centered around a quartered bull's eye, shown in figure 2.7. In total, the detector has a sensitive detector area with a diameter of 90 mm.

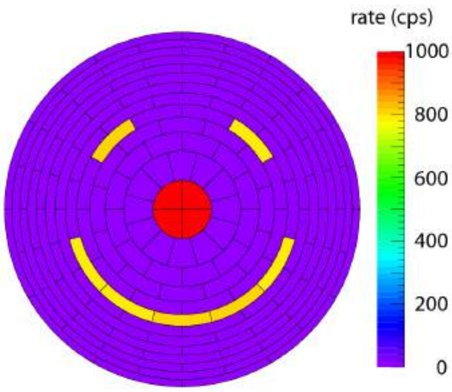

Figure 2.7: Segmented focal plane detector with 148 silicon p-i-n diodes [54].

Characteristic properties of the FPD are listed in table 2.1 [57, 58].
The FPD is designed to detect electrons at low rates. The current limit of 62 kcps (kilocounts per second) for the entire detector (i.e. ≈ 420 cps per pixel) is set by the read-out speed which applies to the overall bandwidth [59] [5]. For high rates in the kcps range, distortions appear in measured spectra due to pile-up effects. Figure 2.8 shows these distortions in energy spectra of monoenergetic electrons, measured at different count rates.

5 Further upgrades to the FPGA are planned which are aimed to allow for higher rates up to > 10 kcps/pixel.

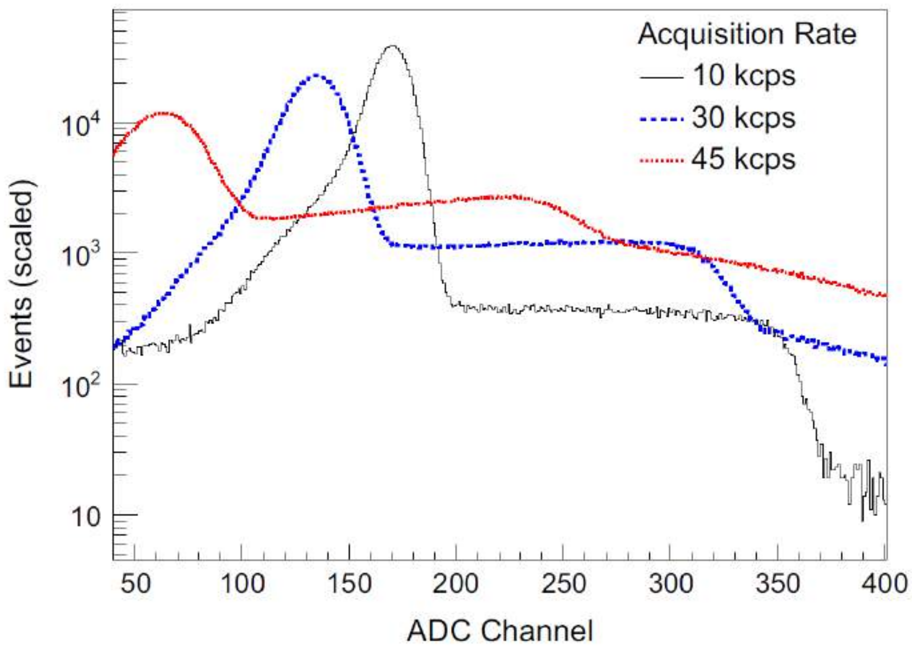

Figure 2.8: Energy spectra of 18.6 keV electrons. For high counting rates, the spectrum shape is distorted due to pile-up effects. The measured event rate is suppressed and the energies are shifted [57].

In the design KATRIN mode, with the goal to measure the active neutrino mass, high count rates do not occur. However, for a future sterile neutrino search the capability of high count rates is of significant importance (section 2.2) and improvements in dead layer thickness, energy resolution and energy threshold are required for this purpose.

2.2 Sterile KATRIN mode

The KATRIN experiment has a very promising potential to search for sterile neutrinos in the mass range of a few keV [60, 61]. Section 2.2.1 describes the impact of sterile neutrinos on the measured tritium β-decay spectrum. Section 2.2.2 focuses on the expected sensitivity in respect to a sterile neutrino search with KATRIN. The experimental requirements and modifications of the KATRIN setup are discussed in section 2.2.3.

2.2.1 Sterile neutrinos in tritium β-decay

The measured tritium β-decay spectrum with KATRIN is a superposition of spectra, corresponding to the individual mass eigenstates of the electron (anti-) neutrino. However, it is not possible to resolve the light mass eigenstates m_i experimentally, therefore KATRIN is sensitive to the effective electron neutrino mass

$$m_{\nu_e} = \sqrt{\sum_i m_i^2 |U_{ei}|^2} \,. \tag{2.4}$$

A right-handed (sterile) neutrino is a flavour eigenstate and hence composed of mass eigenstates. In case of a small mixing among the sterile and active states, the sterile neutrino is mostly composed of the new associated mass eigenstate m_s, but has a small admixture of the three light mass eigenstates m_1, m_2 and m_3. The other way around, also the electron neutrino would contain a small admixture of the new mass eigenstate m_s. In the case of keV-scale sterile neutrinos, there is a large mass splitting between the light neutrino mass eigenstates and m_s which would result in a detectable superposition of tritium β-decay spectra. Mathematically, the resulting superimposed spectrum is given by

$$\frac{d\Gamma}{d\mathrm{E}} = \cos^2\vartheta \left(\frac{d\Gamma}{d\mathrm{E}}\right)_{m_{\nu_e}} \Theta(E_0 - E - m_{\nu_e}) + \sin^2\vartheta \left(\frac{d\Gamma}{d\mathrm{E}}\right)_{m_s} \Theta(E_0 - E - m_s), \tag{2.5}$$

where E is the kinetic electron energy, E_0 denotes the endpoint energy and ϑ the mixing angle between active and sterile neutrinos. Θ is the Heaviside step function. Figure 2.9 shows the impact of active-to-sterile mixing on the tritium β-decay spectrum ($m_s = 10$ keV and $\sin^2\vartheta = 0.2$). It leads to a spectrum distortion and leaves a characteristic kink-signature in the spectrum.[6]

2.2.2 Sensitivity studies

There are several reasons why KATRIN is very suitable to look for sterile neutrinos. One of the main advantages is the high-luminous tritium source strength which allows to achieve high statistics and probe even small mixing angles. Moreover, with an endpoint of 18.6 keV a search for sterile neutrinos with masses up to this

6 Note, that a realistic mixing angle could be of the order of $\sin^2\vartheta = 10^{-6}...10^{-11}$. The value $\sin^2\vartheta = 0.2$ is solely used for didactic reasons to make the kink visible in the spectrum.

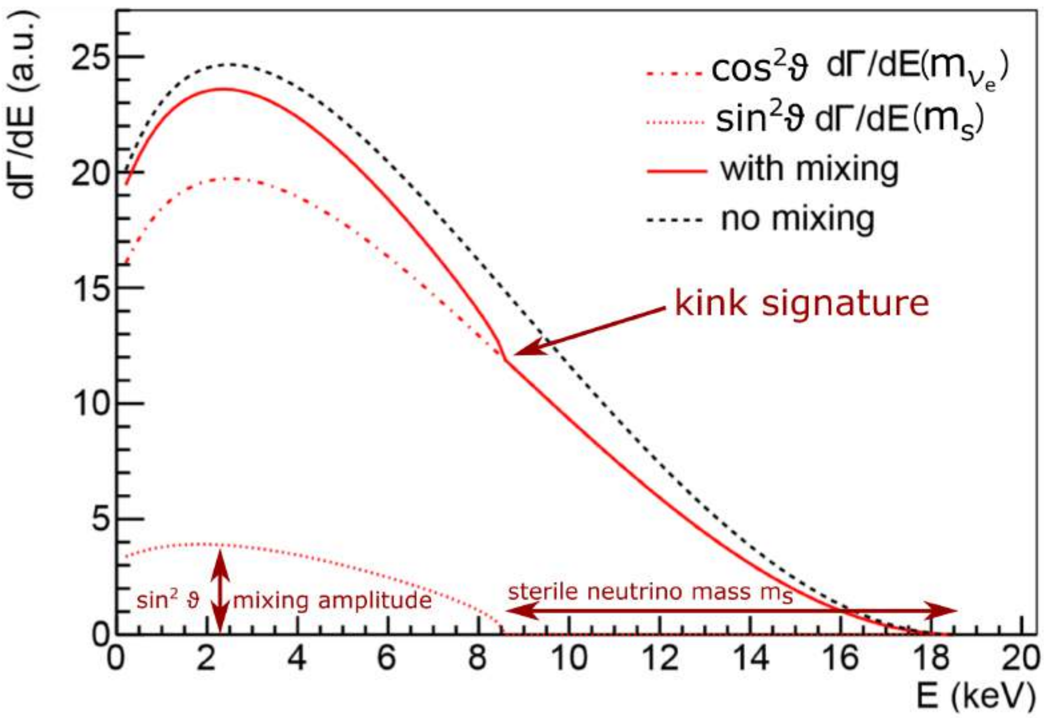

Figure 2.9: Tritium β-decay spectrum for $m_s = 10$ keV and $\sin^2\vartheta = 0.2$ with active-to-sterile mixing (red solid line) and without mixing (black dashed line). A characteristic kink-signature appears at the heavy mass m_s [61].

value is possible in principle. That range is of great interest for DM particles in cosmolgy, see figure 1.13.
Recent sensitivity studies with a spectral fit approach [60], which fits the entire spectrum including theoretical corrections, and a wavelet approach [61], which precisely looks for the kink in the spectrum, show a KATRIN sensitivity down to a mixing angle $\sin^2\vartheta = 10^{-6} \ldots 10^{-8}$ as shown in figure 2.10.
Since the concrete realization of a future KATRIN experiment is still being investigated, these initial sensitivity studies do not include all experimental effects and can be understood as a best-case scenario.

Both analysis procedures strongly favour a differential measurement of the tritium β-decay spectrum over an integral measurement of the entire spectrum. This can be understood since the relative spectrum distortion due to the kink-signature is larger for a differential than for an integral measurement mode. Figure 2.11 shows the ratio of tritium β-decay spectra with and without active-to-sterile mixing for both scenarios, an integral and a differential measurement for $m_s = 10$ keV and $\sin^2\vartheta = 10^{-6}$.

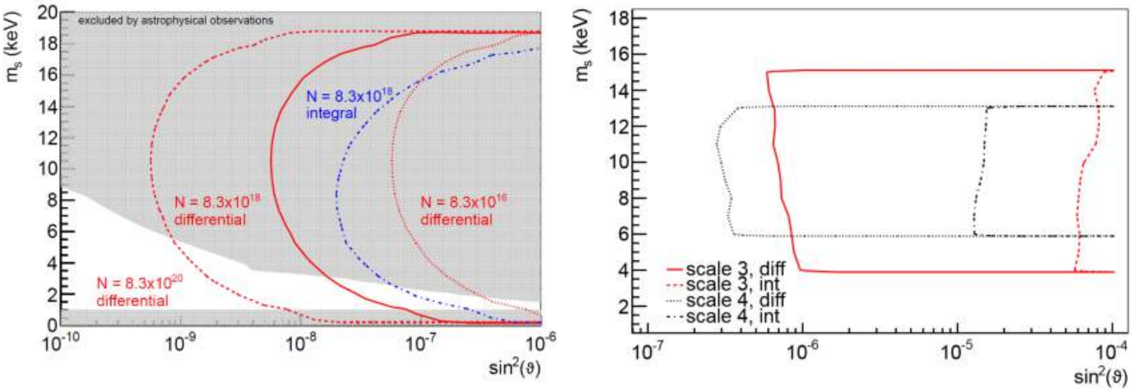

(a) **(b)**

Figure 2.10: 90% C.L. statistical exclusion limit for both differential and integral measurements with a measurement time of three years. **(a)**: Spectral fit approach [60] with different numbers N of tritium molecules in the WGTS. $N = 8.3 \cdot 10^{18}$ is the design value. The grey area indicates the region excluded by cosmological observations in the m_s-$\sin^2 \vartheta$-plane. **(b)**: Wavelet approach [61] for different scales, i.e. frequency bands in the wavelet transformation, for differential and integral measurement modes.

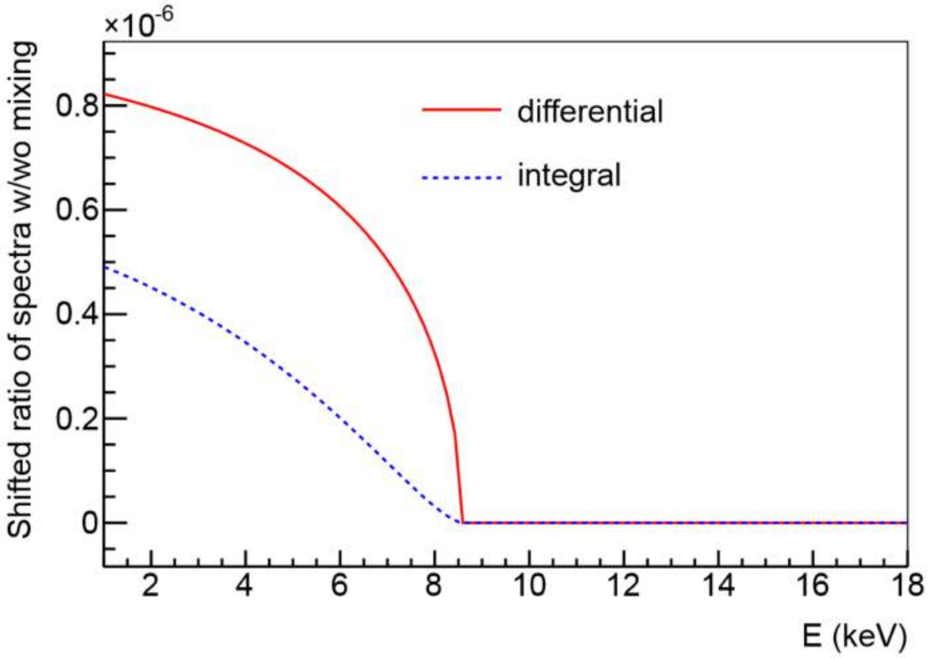

Figure 2.11: Ratio of tritium β-decay spectra with and without active-to-sterile mixing for both differential and integral measurement modes [61]. The differential mode shows a stronger characteristic kink-signature which leads to a higher sensitivity in the 90% C.L. exclusion curves in figure 2.10.

2.2.3 Novel detector design for KATRIN

KATRIN has its highest sensitivity on the mixing angle $\sin^2\vartheta$ for a high count rate (i.e. a high source strength) in a differential measurement mode (figure 2.10). However, the current KATRIN detector is not designed to handle high rates. It experiences pile-up issues for rates above kcps (figure 2.8) and is not optimized to provide a good energy resolution. Moreover, for high acquisition rates the current KATRIN data acquisition cannot record entire waveforms anymore and an ADC Non-Linearity correction of the waveforms, which is strongly favoured (see chapter 4), would be impossible.

Consequently, in order to measure the entire tritium β-decay spectrum in a differential mode, a new detector has to be designed. This section investigates the requirements on such a detector and presents the idea of a novel multi-pixel silicon drift detector design.

- **Handling high rates**
  The crucial challenge for a novel KATRIN detector to search for sterile neutrinos is the capability of handling high rates. This requires small drift times within the silicon pixels and a rather small time constant of the read-out capacitor. The number of pixels should be large to distribute the high count rate over many pixels, reducing the effective rate per pixel as well as pile-up effects. On the other hand, the maximum number of pixels is also limited if each pixel shall be read out individually. A feasible compromise could be of the order of 10^4 pixels (*FPD*: 148 pixels).

- **Thin dead layer**
  In contrast to the design KATRIN mode, in a differential mode the energy measurement is not performed by the main spectrometer anymore. The spectrometer is set to low voltage and all electrons with surplus energies can reach the detector. The detector does not only count the incident particles but also measures their energies.
  For a high-precision energy measurement a thin dead layer on the silicon pixels is required. The latter can be described as a dead detector volume at the surface, where ionizing particles lose energy which is not collected at the read-out contact and thus not seen by the read-out electronics. A thin dead layer decreases the energy threshold, i.e. it allows a detection of low-energy electrons and significantly improves the energy resolution.

Moreover, in KATRIN the incident particles hit the detector surface with different incident angles. The less perpendicular the incident angle to the detector wafer, the more energy is lost in the dead layer. A thin dead layer reduces the uncertainty of energy losses within the dead layer. A dead layer thickness of 10 nm is intended (*FPD:* 155 nm).

- **Energy resolution**
  The energy resolution in the differential KATRIN mode is not given by the properties of the MAC-E filter anymore. It is rather given by the Poisson statistic of the generated electron-hole pairs in the depleted silicon region, the Fano-factor, which reduces the statistical spread due to multiple excitation mechanisms, and electronic noise [62]. For a 18.6 keV electron the physical lower bound of energy resolution ΔE_{FWHM} for a silicon sensor is given by equation 2.6:

$$\Delta E_{\mathrm{FWHM}} = 2.35 \cdot \Delta E_{\sigma} = \sqrt{f/N} \cdot E = 206 \text{ eV}. \tag{2.6}$$

  ΔE_{FWHM} is the energy resolution (full width half maximum), ΔE_{σ} the 1σ energy resolution of a Gaussian, $f = 0.115$ is the Fano-factor for silicon, $N = \frac{E}{E_{\mathrm{ehp}}}$ is the number of generated electron-hole pairs in a silicon sensor for an incident electron with energy $E = 18.6$ keV and an electron-hole-pair conversion factor of $E_{\mathrm{ehp}} = 3.6$ eV/ per electron-hole pair. An ultra-low noise level in order to achieve an energy resolution of 300 eV at 18.6 keV is intended (*FPD:* 1.52 keV at 18.6 keV).
  This energy resolution is very important for a wavelet kink-search [61], as this technique aims to detect the kink-like feature in the spectrum, and a too poor energy resolution would wash-out this feature. In contrast, the spectral fit approach prooves to be rather insensitive to the energy resolution. Here, one exploits the fact that sterile neutrinos do not only leave a kink-signature in the tritium β-decay spectrum, but also modify the entire spectrum shape. The washing out of the kink by the energy resolution is accounted for by the overall spectrum distortion of sterile neutrinos [60].

- **Minimize noise**
  A small peaking time τ for filtering the signal waveforms is required to reduce pile-up effects and to handle high rates per pixel. However, the series noise Q_{series} linearly depends on the detector capacitance C_{d} and becomes most important for small peaking times.

$$Q_{\text{series}} = \sqrt{(4kTR_{\text{s}} + v_{\text{a}}^2)} \cdot \frac{C_{\text{d}}}{\sqrt{\tau}}. \tag{2.7}$$

Here, k is the Boltzmann constant, T the operation temperature, R_{s} the series resistance of the detector, v_{a} the amplifier noise, τ the peaking time and C_{d} the detector capacity [62].

A low detector capacity is required which can be achieved by collecting the charge clouds in the sensor at small point contacts. The designed prototype detectors yield calculated values of $C_{\text{d}} = 0.04$ pF (*FPD:* 8.2 pF).

Combining all these requirements leads to the idea of a multi-pixel silicon drift detector with a thin dead layer, small read-out point contacts and shared steering electrodes to guide and focus the charge clouds.
The detector could have a diameter of 20 cm (*FPD:* 9 cm) and $\approx 10^4$ pixels.

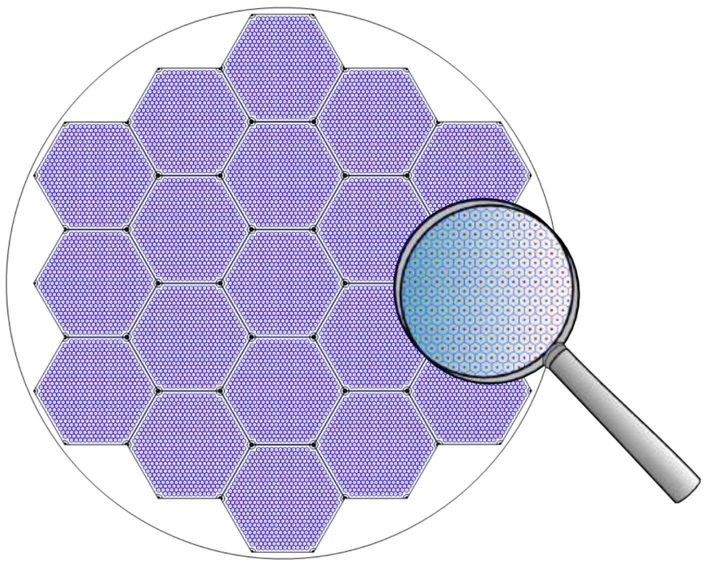

Figure 2.12: Idea of a possible realization for a novel KATRIN detector to search for sterile neutrinos: a multi-pixel silicon drift detector with $\approx 10^4$ hexagonal pixels, small point contact anodes and common steering electrodes [63].

3 Prototype detectors and setup

This chapter focuses on the development of the prototype detector TRISTAN in the context of a search for sterile neutrinos with KATRIN. First of all the principle of a silicon detector is explained (3.1.1) and different designs for the new prototype detectors are shown (3.1.2). The front-end electronics and PCB design to read out the detectors are discussed (3.2) and the setup of a new detector test stand at KIT is described (3.3). Finally, first measurement results of the detector are presented (3.4).

3.1 Prototype detectors

In collaboration with the semiconductor laboratory of the Max-Planck Society Munich (HLL) [64] and the sensor department of Lawrence Berkeley National Laboratory (LBNL) [65], seven-pixel silicon prototype detectors were designed and produced. These prototype detectors are the first step towards a future novel large-scale detector system for the KATRIN experiment in order to measure the entire tritium β-decay spectrum in a differential mode with high counting rates. The main focus in this section is set on the working principle and detector layout of the novel prototype detectors, which combine the advantages of silicon drift detectors with those of a thin dead layer.

3.1.1 Introduction to silicon sensors

Semiconductors have been used as detectors in particle physics for over 50 years. Silicon detectors in particular have proven suitable for many experiments. Silicon has a band gap of 1.12 eV and a good intrinsic energy resolution: For each 3.6 eV of deposited energy of an ionizing particle, one electron-hole-pair is created. The band gap is smaller than 3.6 eV, as silicon is an indirect semiconductor, where transitions between valence band and conduction band are only possible with an additional phonon exchange.

Silicon exists in abundance and its gap properties can be easily changed by inserting dopants into the sensor. Doping with group V elements (*donors*, e.g. phosphorus) lead to *n-type* silicon, *p-type* silicon is realized by adding group III elements (*acceptors*, e.g. boron). Depending on the doping, the Fermi energy is shifted towards the valence band (acceptor doping) or the conducting band (donor doping) respectively to increase the probability of exciting holes or electrons. Fundamental semiconductor concepts are discussed in detail in literature, for example in [66].

Working principle of a silicon sensor

Silicon sensors are operated in *reverse bias mode* of a *pn-junction* configuration with *p-type* and *n-type* silicon. In this mode, the detector volume is depleted and a space charge region establishes at the pn-junction. For a non-depleted silicon detector, the intrinsic number of free charge carriers would in contrast exceed the number of electrons or holes, generated by ionizing particles, by several orders of magnitude and it could not be used as a particle detector [67].

At the pn-junction of a silicon diode, electrons drift from the *n-type* to the *p-type* region, holes drift vice versa. A schematic drawing is shown in figure 3.1. An equilibrium of diffusion and recombination creates a space charge region and an electric field with a diffusion voltage V_{diff} establishes.

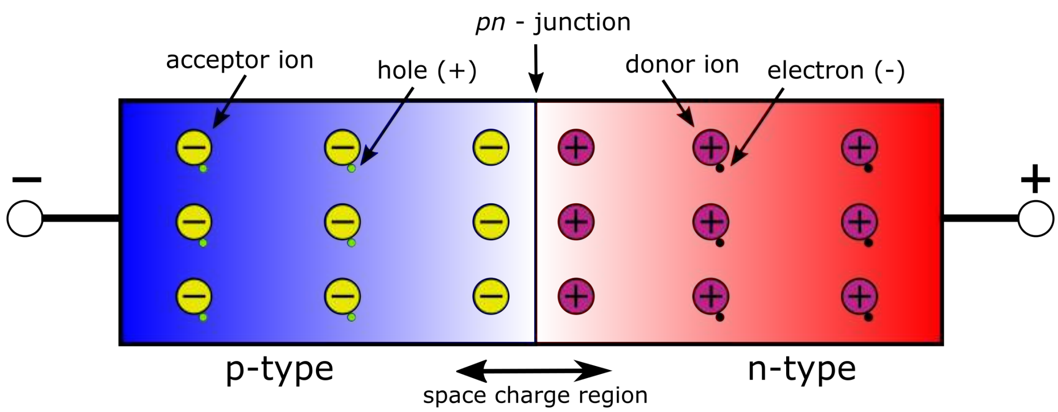

Figure 3.1: Reverse-biased *pn*-junction configuration of a silicon diode. Donor electrons drift towards the *p*-side, acceptor holes move towards the *n*-side and create a depleted space charge region. Applying an external reverse bias voltage further increases the depleted region.

However, the dimensions of this intrinsic space charge region are limited. To deplete the entire sensor volume, the equilibrium has to be disturbed by an external

voltage $V_{\text{ext}} \gg V_{\text{diff}}$ which increases the depletion width.
If an ionizing particle hits the detector, it loses energy according to the *Bethe-Bloch* formula.

$$-\frac{dE}{dx} = 4\pi N_A r_e^2 m_e c^2 z^2 \frac{Z}{A} \frac{1}{\beta^2} \left[\frac{1}{2} \ln \left(\frac{2 m_e c^2 \beta^2 \gamma^2 T_{\max}}{I^2} \right) - \beta^2 - \frac{\delta}{2} \right] \tag{3.1}$$

with Avogadro's number N_A, the classical electron radius r_e, electron mass m_e, speed of light c, charge z of incident particle, atomic number Z, atomic mass A, $\beta = v/c$ with particle velocity v, $\gamma = \frac{1}{\sqrt{1-\beta^2}}$, the maximum kinetic energy $T_{\max}$ that can be transferred to an electron in a collision, mean excitation energy I and density effect correction δ. The lost particle energy is transformed into the creation of electron-hole pairs in the sensitive detector volume.

3.1.2 Detector design

In section 2.2.3 the requirements for a suitable detector to search for sterile neutrinos with KATRIN are derived: Low capacity, thin entrance window and short drift times to handle high rates are some of the essential requirements.
In collaboration with HLL and LBNL, silicon drift detectors were designed, aiming to fulfil the given criteria and prototype detectors have been produced to test both feasibility and performance of these designs.
The prototype detectors have seven hexagonal pixels. Each pixel has a small point contact to ensure a small detector capacity. This is important to obtain a low serial noise for short peaking times. The point contacts are surrounded by different numbers of steering electrodes which guide the charge clouds to the point contacts. The steering electrodes allow for full charge collection even for small read-out contacts.

Several different prototypes were produced by HLL and LBNL with different approaches: Both are n-type detectors (they have an *n-type* silicon bulk), the HLL detectors have the pn-junction between bulk and entrance window, whereas for the LBNL sensors the pn-junction occurs directly at the point contact which leads to different electric field configurations in the sensor: One type of detectors collects electrons (HLL), the other one collects holes (LBNL) at the read-out point-contact.
In the case of the LBNL detector, the entrance window can naturally be extremely thin ($\approx$ 10 nm), whereas in the case of the pn-junction at the entrance side of the detector the dead layer is typically larger ($\approx$ 50 nm). However, in the LBNL design the intrinsic electric field configuration makes the operation of the detector with a

drift ring design very challenging. In contrast, the HLL design with the pn-junction at the entrance is known to work perfectly in a design with a drift ring configuration. Here, our goal is to minimize the dead layer thickness of the HLL detector design and on the other hand to test the feasibility of operating the LBNL detectors as silicon drift detectors.
In the detector schematic (one pixel of HLL sensor) in figure 3.2, electrons, created by an incident ionizing particle, drift towards the readout point contact, whereas holes travel to the back plane which is set to negative voltage. The steering electrodes are also set to negative voltage to guide the electrons to the point contact where the signals are read out DC-coupled and forwarded to an amplifier.

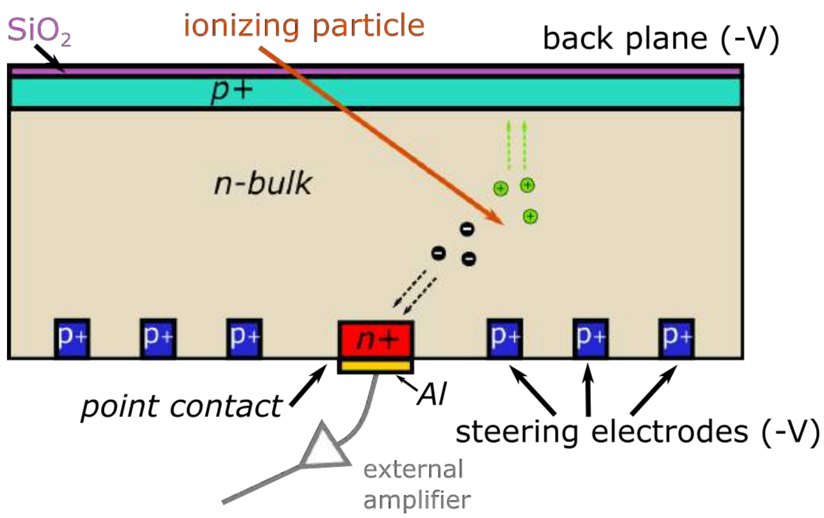

Figure 3.2: Schematic drawing of a cross section of a silicon drift detector with a weakly doped *n-type* bulk, a highly doped backplane ($p+$) and point contacts ($n+$), as it is the case for the HLL prototype sensors. Electrons follow the electric field lines to the point contact, holes drift to the back plane. The steering electrodes are set to negative potential to guide the electrons to the small point contact.

HLL

The prototype detectors produced by HLL have four different sizes of 0.25 mm, 0.5 mm, 1.0 mm and 2.0 mm per cell (pixel). They also vary in the number of steering electrodes, and in the technology and sequences, used to produce a thin entrance window. Figure 3.3 shows the design for three different prototype detectors with multiple drift rings. The point contact anodes have a diameter of 90 μm for all pixel sizes.

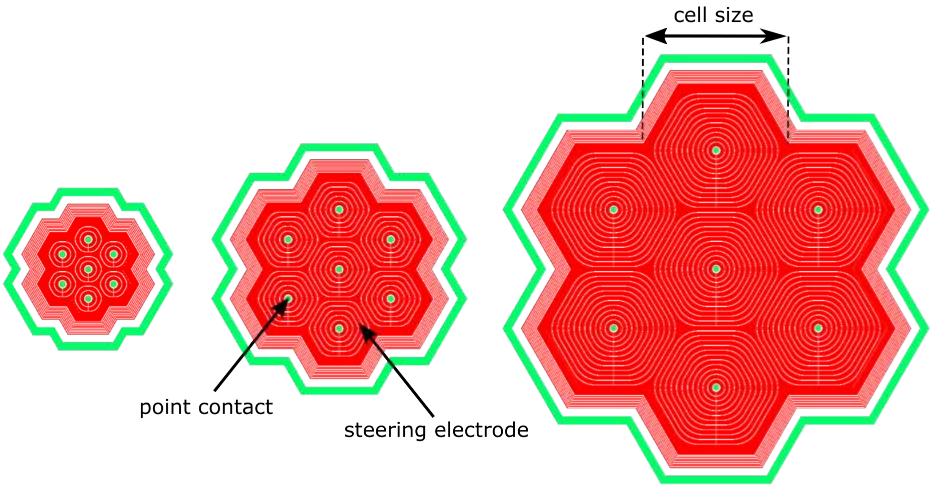

Figure 3.3: Schematic drawing of prototype detectors with cell sizes of 0.5/1.0/2.0 mm [68]. The detectors have seven pixels, each one has a small point contact anode and varying number of steering electrodes to ensure short drift times.

Each size of prototype detector is produced with $N = 1, 2$ and N_{max} drift rings, where $N_{\text{max}} = 2, 3, 6, 12$, see table 3.1. The largest prototype detector of 2 mm cell size is only produced with $N_{\text{max}} = 12$ rings, as its reliability is not promising in the design with only one or two drift rings.

Table 3.1: Maximum number of steering electrodes in the multiple drift ring design

Cell size	N_{max}
0.25 mm	2
0.50 mm	3
1.00 mm	6
2.00 mm	12

Concerning the entrance window (p-implantation), different versions of the HLL prototype differ in process technology parameters like implantation energy, implantation dose, stray oxide thickness and annealing temperature. For some prototypes a deep n-type counter implant is introduced with the intention to partially compensate the diode's p-implanted dose and to increase the electric field [69].

The prototype detectors are produced on chips of 8 mm x 8 mm as shown in figure 3.4. Three detectors are situated on each chip except for the largest cell size 2 mm, where only one detector is placed.

Figure 3.4: Pictures of HLL sensors. Three different detectors with seven pixels each are placed on one squared chip. The sensors all come from the same monolithic silicon wafer.

Figure 3.5 shows an example bonding schematic for one of the prototype detectors in the multiple drift ring designs with a cell size of 0.5 mm. In this design, only the inmost (V_{Ring1}) and outmost (V_{Ring2}) drift rings are connected to external voltage supplies, the voltages of the drift rings in between are defined by an integrated voltage divider.

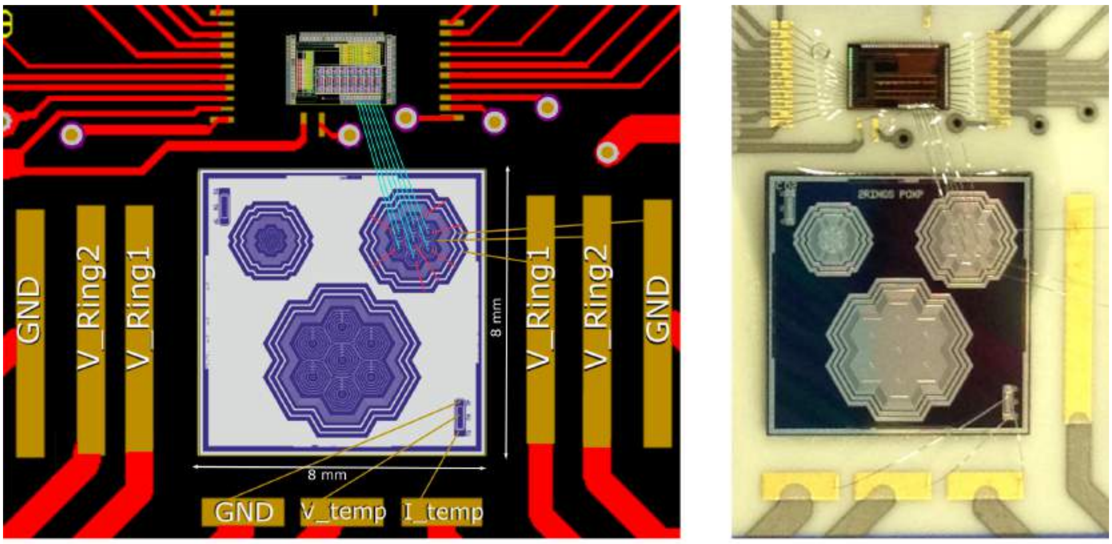

(a) **(b)**

Figure 3.5: Bonding scheme **(a)** and picture of wire bond connections **(b)** on the PCB top layer for an HLL prototype detector with a cell size of 0.5 mm. Two temperature sensors are places on each wafer, one of them is connected. Wire bonds connect the pixel anodes to the input channels of a preamp chip.

Table 3.2: Required voltages for HLL prototype detectors

Voltage Label	Description	Voltage range
V_{Ring1}	inmost steering electrode	-5 V ... -20 V
V_{Ring2}	outmost steering electrode	-5 V ... -20 V $(N = 2)$
		-10 V ... -100 V $(N > 2)$
GND	detector bulk	0 V
V_{temp}	isolation of temperature sensor	-5 V .. -15 V
$V_{\text{BackContact}}$	bias voltage	-100 V ... -200 V
$V_{\text{BackFrame}}$	reduces charge loss at sensor edge	$V_{\text{BackContact}}$ - 10 V
V_{BackGate}	for inversion layer entrance window	$V_{\text{BackContact}}$ - 10 V
I_{temp}	current input for temp. sensor	1 μA
		(1 V at $R = 1$ MΩ)

The voltage V_{Ring1} is wire bonded from the bond pad to a bus ring around the detector. From the bus ring, internal wire bonds connect the different cells. The bulk is set to ground potential. The point contact anodes are directly connected to the respective input pads on a preamp chip.
The detector backside is connected to the voltages $V_{\text{BackContact}}$ and $V_{\text{BackFrame}}$ on the bottom side of the printed circuit board (PCB). Depending on the type of entrance window (if a hole-inversion layer is used or not), a third voltage V_{BackGate} has to be connected.
A temperature sensor diode is is placed on the chip which is connected to GND and to a constant current source with $I_{\text{temp}} \approx 1\ \mu$A. A potential of 1 V will be applied on a resistor with $R = 1$ MΩ, which acts as a constant current source with $I_{\text{temp}} \approx 1\ \mu$A. The voltage V_{temp} shields the temperature sensor from electrical distortions. The voltage drop at the diode, biased in forward direction, gives information about the chip temperature. It changes by 3 $\frac{\text{mV}}{K}$, a material property of silicon [69].
Table 3.2 lists the required voltages for the prototype sensors and gives estimations on the respective voltage ranges based on simulations and experiences of HLL.
In operation mode the detector will be backside illuminated with an electron beam of an e-gun or with a γ-source, such as ^{55}Fe.

LBNL

In contrast to the the HLL detectors, the prototype detectors of LBNL have an n+ entrance window, an n-bulk and p+ read-out contacts. The pn-junction occurs between the n-bulk and the point contact, the sensor collects holes instead of electrons. Figure 3.6 shows drawings of the LBNL prototype detectors. They also have small point contacts and surrounding drift ring steering electrodes to guide the holes to the point contacts. The prototypes are produced with one to three steering electrodes and cell sizes between 0.52 mm and 1.2 mm. The production of the LBNL prototype detectors is ongoing at the moment.

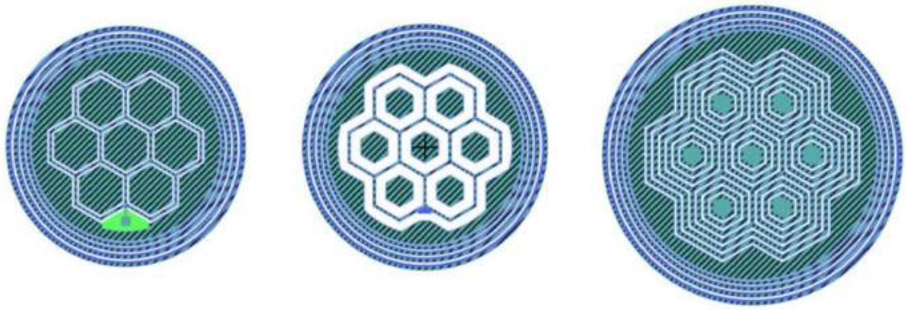

Figure 3.6: Prototype detectors of LBNL [70]. Steering electrodes guide the created holes to the point contacts in the center of each of the seven pixels.

3.2 PCB design

Within the framework of this thesis, the PCB for the HLL detector was designed. The PCB system consists of two boards: The main PCB acts as a holding structure for both sensor and preamp and is used to connect those to electric circuits. The second one, the adapter PCB, is an interface between the main PCB and D-sub connectors in a flange of the vacuum chamber.
The PCBs will be operated in vacuum to be able to test the detectors with an electron gun. Therefore, certain vacuum requirements had to be taken into account in the PCB design. The standard FR-4 glass epoxy substrate is not compatible with vacuum conditions and leads to a large amount of outgassing when operated in vacuum, consequently a Al_2O_3 ceramic is used as a substrate. As solder resist should also not be used in vacuum due to outgassing, a layer of blue protection glass is burned on the main PCB to prevent the traces to be barely exposed and to avoid scratches or other damages on the surface. The areas of sensor, preamp and bonding pads are excluded from the protection layer to allow for wire bonding. Space restrictions by the vacuum chamber (CF 100 double cross, see section 3.3) set limits of 6 cm on the board dimensions.
The PCBs were designed with the software *Altium*, fabrication was executed by the

company *Dorazil* in Berlin. The traces are made out of *AgPd*, solder pads out of *Sn* and bond pads out of *Au*. The wire bonds themselves consist of *Al*.

3.2.1 Main PCB

The main PCB is a double layer board. It has a hole of 7 mm x 7 mm in its center, where the detector chips are mounted. On its left and right, bond pads are situated to provide voltage supplies for the steering electrodes (V_{ring1} and V_{ring2}), and *GND* connections for the anode point contacts. Figure 3.7 shows the top layer design of the main PCB. The bond pads are placed on both sides of the sensor hole for reasons of bonding convenience.

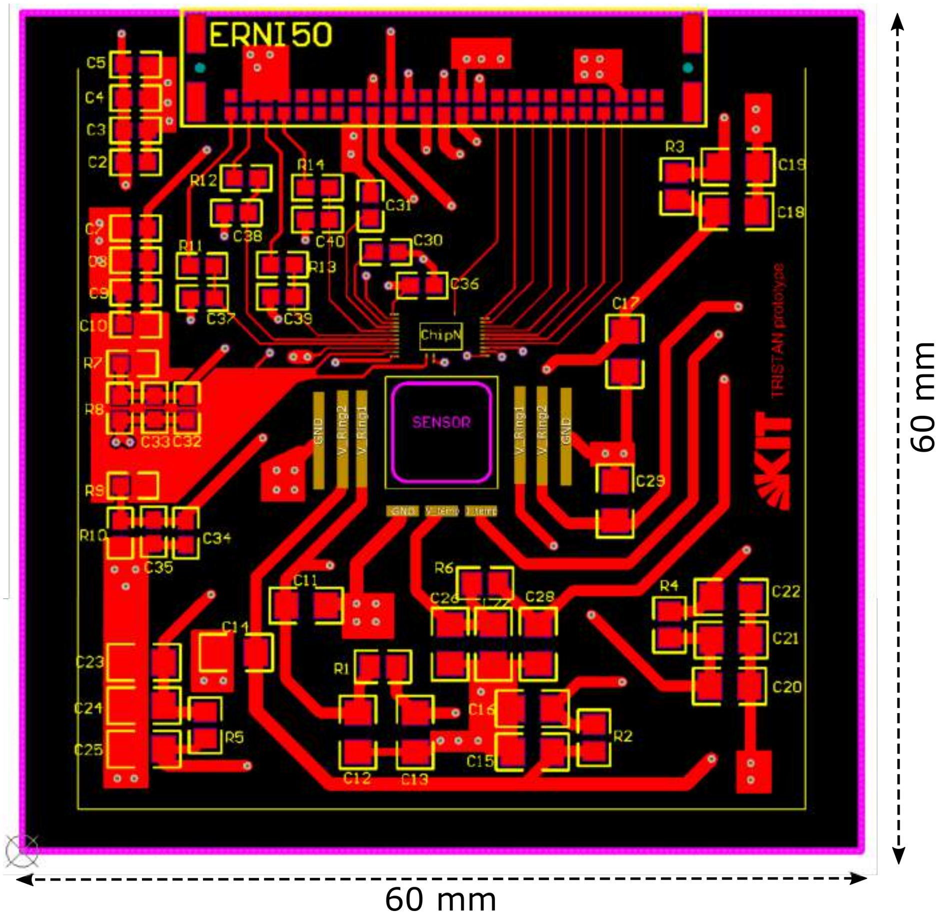

Figure 3.7: Main PCB design, top layer.

Below the cut-out area, there are three further bond pads to connect the temperature sensor to I_{temp}, V_{temp} and *GND*. A preamp chip (labelled as *ChipN*) is mounted above the sensor to amplify the sensor output signals. Wire bonds connect sensor

and preamp.
On the back side (see figure 3.8), bond pads for biasing the detector, $V_{\text{BackContact}}$, $V_{\text{BackFrame}}$ and V_{BackGate} are situated.

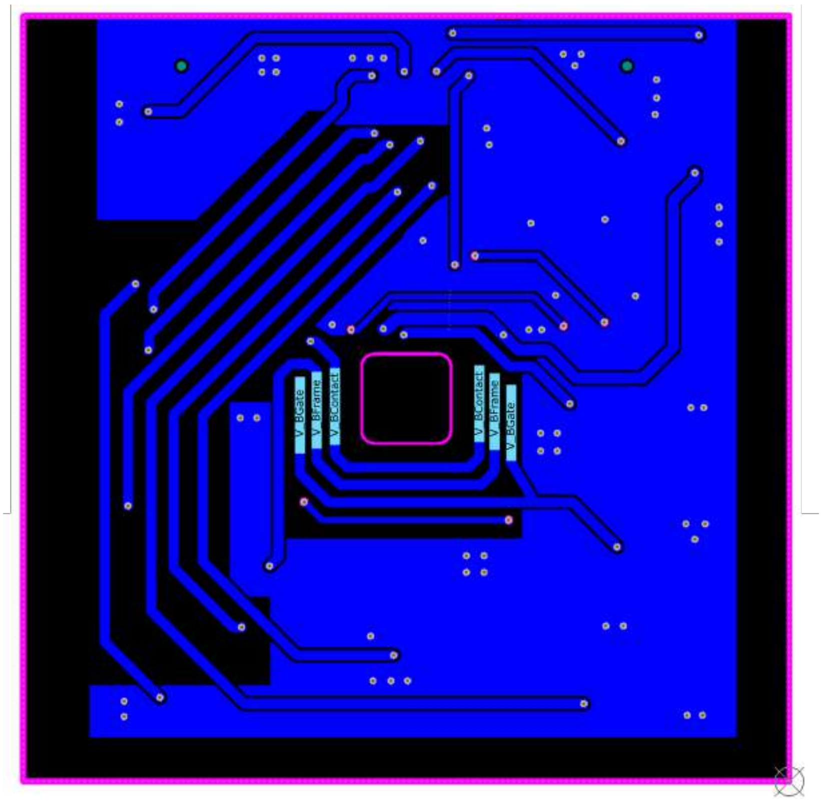

Figure 3.8: Main PCB design, bottom layer (mirrored).

Several SMD (surface mounted device) capacitors and resistors are placed on the PCB top side. The sensor voltages are filtered by blocking capacitors and RC low-passes with a corner frequency of

$$f_c = \frac{1}{2\pi RC} = 53 \text{ Hz}, \tag{3.2}$$

with $R = 30\ \text{k}\Omega$ and $C = 10\ \text{nF}$ to ensure voltage stability. As an example, figure 3.9 shows the respective circuit for $V_{\text{BackContact}}$.

The digital configuration signals for the preamp chip configuration are also filtered by a low-pass with $f_c = 1.5\ \text{MHz}$ to attenuate oscillations, arising from the steep slopes of the digital signals.
The bottom layer basically consists of a *GND* plane and voltage traces crossing the plane. For necessary *GND* connections on the top layer, multiple parallel *GND* vias

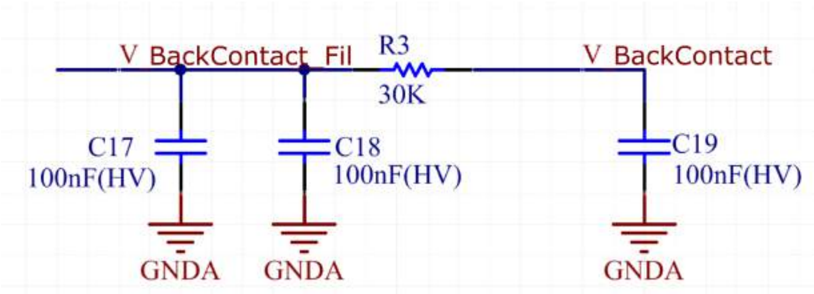

Figure 3.9: Low-pass circuit for $V_{\text{BackContact}}$ with a corner frequency of 53 Hz. The filtered voltage $V_{\text{BackContactFill}}$ goes to the respective bond pads and via a wire bond to the detector.

are placed on the PCB, connecting the top layer to the *GND* plane on the bottom layer. Several of them are placed in parallel to decrease the inductance caused by a single via. The vias have an inner diameter of 0.3 mm, the traces vary in thickness between 0.15 mm for signal traces and 0.8 mm for high voltage traces.
For fabrication reasons and to avoid flashovers, general PCB design rules were applied, which imply to have at least the distance of the width of a trace between two traces and to ensure electric fields below 100 $\frac{\text{V}}{\text{mm}}$ [71].

Components

Table 3.3 lists the used components of the main PCB with their respective values and sizes.

Table 3.3: List of components on the main PCB.

Name	Component	Type	Value	Max Voltage
R1 ... R6	resistor	SMD_0805	30 kΩ	200 V
R7, R9	resistor	SMD_0603	1 kΩ	50 V
R8, R10	resistor	SMD_0805	1.2 kΩ	50 V
R11 ... R14	resistor	SMD_0805	1 kΩ	50 V
C2 ... C4	capacitor	SMD_0603	100 nF	3.3 V
C5, C10	capacitor	SMD_0603	22 μF	3.3 V
C7 ... C9	capacitor	SMD_0603	100 nF	3.3 V
C11 ... C29	capacitor	SMD_1206	100 nF	200 V
C30 ... C35	capacitor	SMD_0603	100 nF	3.3 V
ERNI50	SMC connector, 50 Pins			500 V

Preamplifier

The seven point contacts of the prototype detector are wire bonded directly to a low-noise preamplifier, the respective preamp bond pads are labelled *In1, ..., In7* in the bonding plan in figure 3.10. The preamp chip itself is a new development by *I.Peric*[7].

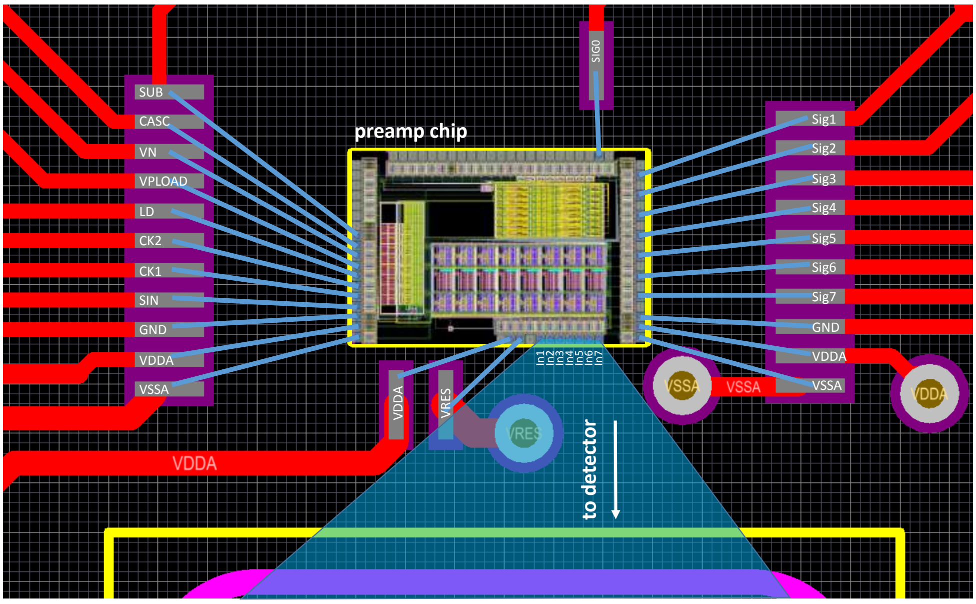

Figure 3.10: Bonding plan for the preamp chip. The preamp is fed with four digital configuration signals (*SIN, CK1, CK2, LD*) and seven analog voltages (*SUB, CASC, VN, VPLOAD, VDDA, VSSA* and *VRES*). The analog amplified detector output signals leave the preamp via wire bonds on the right (*Sig1 ... Sig7*). *Sig0* yields the analog output of the built-in test pixel.

The chip includes an amplifier with a feedback capacity of 15 fF. Simulations show that the intrinsic noise of the chip is expected to be of the order of 5 mV. The chip also in includes a second stage amplification that further enhances the signal by a factor of $\approx$ 10. Finally, the chip has the possibility of digitizing the signals, this feature, however, is not yet sufficiently tested. Table 3.4 summarizes the voltages, needed to operate the chip.

Wire bonds connect the analog amplified detector output signals $Sig1...Sig7$ from the preamp chip to bond pads next to the preamp. $Sig0$ has its bond pad on top of the preamp and carries the output signal of a built-in test pixel (p-i-n diode).

7 KIT, Institute for Data Processing and Electronics (IPE)

Table 3.4: Connections of the preamplifier

Label	Description
SUB	bias voltage for chip substrate
$CASC$	cascode voltage
VN	input amplifier voltage
$VPLOAD$	input amplifier voltage for PMOS transistor in cascode
$VDDA$	bias block voltage
$VSSA$	analog amplifier voltage
GND	ground connection
LD	load serial shift register
$CK1$	1^{st} system clock for two phase clocking
$CK2$	2^{nd} system clock for two phase clocking
SIN	serial-in shift register
$SIG0$	amplified output signal of test pixel
$SIG1$ ... $SIG7$	amplified output signals of seven detector pixels

3.2.2 Adapter PCB

The adapter PCB is used as an interface between the main PCB and two electrical 50-pin D-sub feedthroughs of the vacuum chamber. The adapter board, shown in figure 3.11, is a double layer board with solder pads on top and bottom layer. Cables are soldered to the pads and connect them to D-sub pins. The top layer contains seven solder pads for the digital configuration signals on the left-hand side, each one is separated by a GND connection. The output signals solder pads are situated on the right-hand side of the adapter PCB. All pads are placed in a way that ribbon cables can be soldered to the pads, the pitch equals the ordinary ribbon cable pitch of 1.27 mm. All input voltages for both detector and preamp are connected from the bottom side of the adapter PCB.
The two PCBs are connected to each other with an ERNI SMC connector with 50 pins. The ERNI connectors were chosen because of their high pin density and withstand voltage of 500 V.

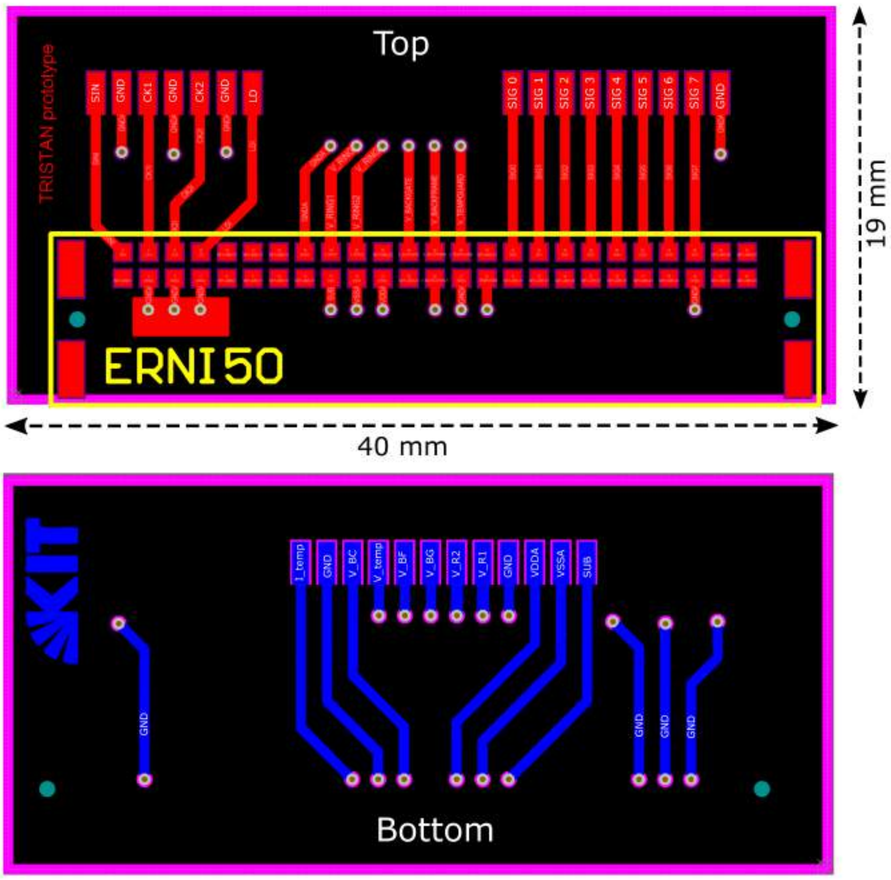

Figure 3.11: Top and bottom layer of the adapter PCB. The top layer includes solder pads for digital configuration signals (left) and analog output signals (right). The input voltage cables are soldered to the solder pads on the bottom side (mirrored image). The ERNI connector connects main and adapter PCB.

3.3 Test stand setup

A test stand for the prototype detector was designed and set up at KIT, an overview is given in figure 3.12. It consists of a double cross with ConFlat flanges with a diameter of 100 mm, CF100, to be operated as a vacuum chamber. Vacuum conditions are required for intended measurements with an electron source. A turbo molecular vacuum pump, Pfeiffer HiCube 80, is situated below the double cross (1). Pump and cross are connected to each other with a bellow and several safety valves. From the right, a cooling finger (2) enters the vacuum chamber. With a flexible hose it is connected to a dewar of liquid nitrogen outside the vacuum chamber. A Pt100 heating element within the dewar heats up the nitrogen and makes gaseous nitrogen flow through the copper cold finger which enters and exits the vacuum chamber via a feedthrough. The opposite side (3) holds two D-sub feedthroughs with 50 pins each for electrical inputs and outputs, i.e. voltage supplies for detector and preamp, digital configuration codes for the preamp and the amplified output signal of the detector. A pressure sensor will be mounted on top of the chamber (4) to monitor the vacuum conditions inside.

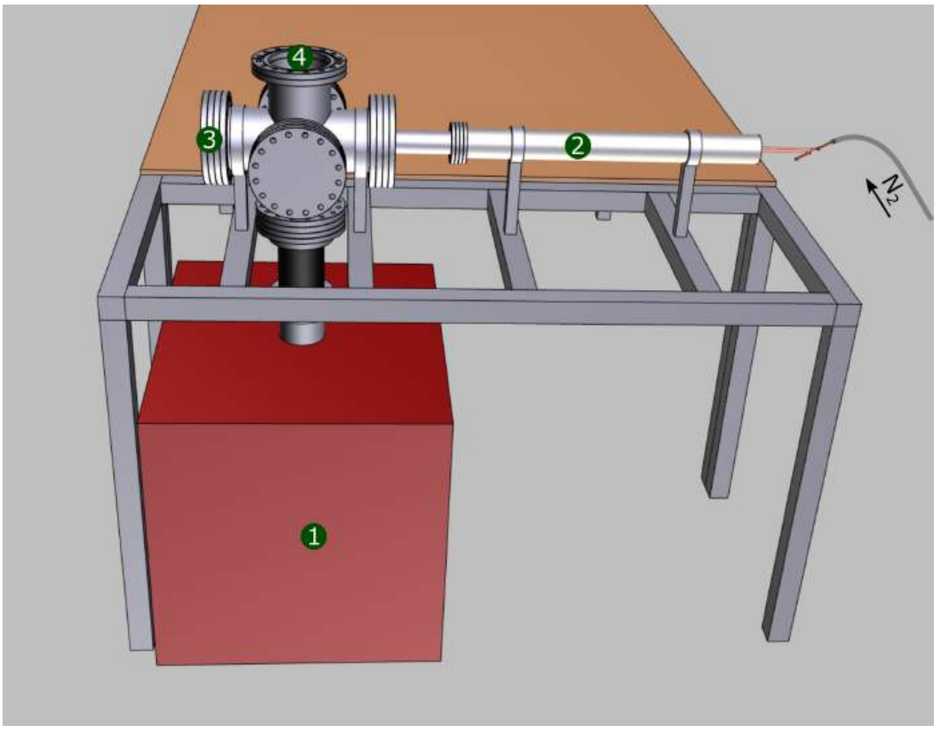

Figure 3.12: Test stand setup with a vacuum pump (1), a nitrogen cooling system (2) and electrical D-sub feedthroughs (3). The top of the CF100 double cross (4) will be closed by a flange with a feedthrough for a pressure sensor [72].

Figure 3.13 shows the top view of the vacuum chamber, with the vacuum pump (1), cooling finger (2), electrical feedthrough flange (3) and top flange for mounting the pressure sensor (4). The main parts of the inside of the vacuum system are a copper block for cooling (5), a card ridge system (6), and a source holding structure (7). The copper block has a groove to fix a set of copper braids, connecting the copper block to the cold finger. This is done as the detector is intended to be operated at $-50°$C to decrease the temperature dependent leakage current by a factor of ≈ 2 for $\Delta T = 7$ K [69]. Moreover, the preamp consumes power in the range of a few mW which is dissipated by the cooling.
The main PCB, holding the detector and the preamp chip, is inserted into the holding structure which works as as a card ridge system, pressing the board onto the copper block to maintain a good thermal contact. This system is very flexible and enables tests of different detectors on different PCBs. The PCB has to be inserted

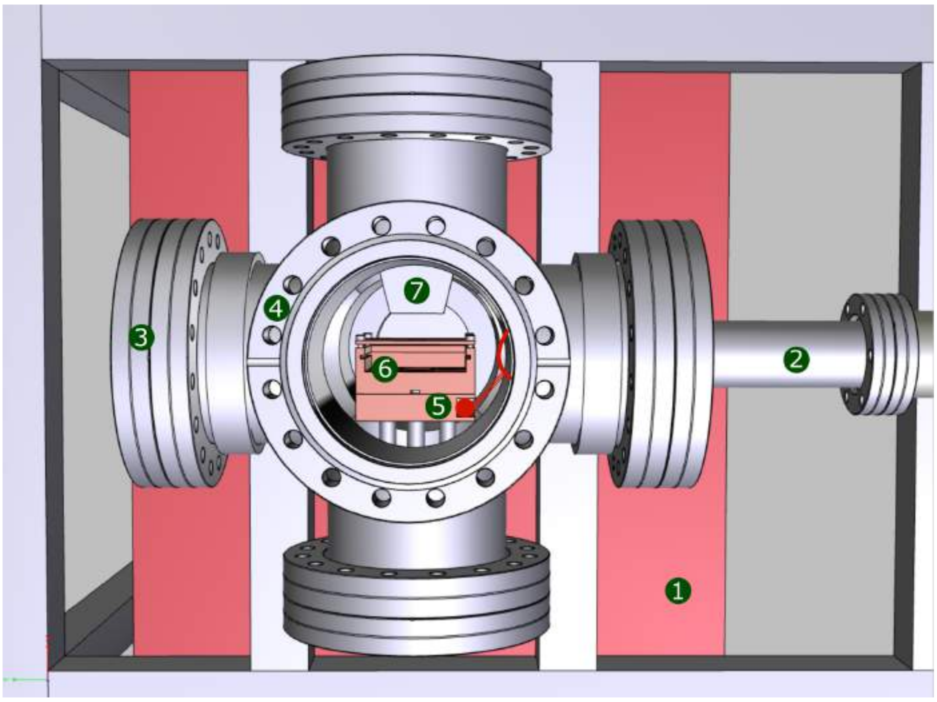

Figure 3.13: Top view on the vacuum chamber. Copper braids connect the cooling finger to a copper block (5). A card ridge system (6) is used as a holding structure for the PCB, a radioactive γ-source can be put on source holding structure (7) to measure γ-ray spectra with the detector.

in a way that the PCB top layer faces the copper block, its bottom layer faces the holding structure for a radioactive γ source, as the detector is operated with back-illumination. The adapter PCB is attached to the top of the main PCB, the cables are guided to the electrical feedthrough flange (3).

Cables and connections

Vacuum side

Inside the vacuum chamber, cables connect the adapter PCB with the inner side of two D-sub feedthroughs (see figure 3.14) in the CF100 flange. The pin assignments for the electrical feedthroughs are given in table 3.5.
One capton ribbon cable is used for the digitial configuration signal, another ribbon cable is used for the voltage supplies of both sensor and preamp. Capton coax cables with a common *GND* are used for the analog output signals of the preamp. Figure 3.15 shows a photograph of the cabling inside the vacuum.

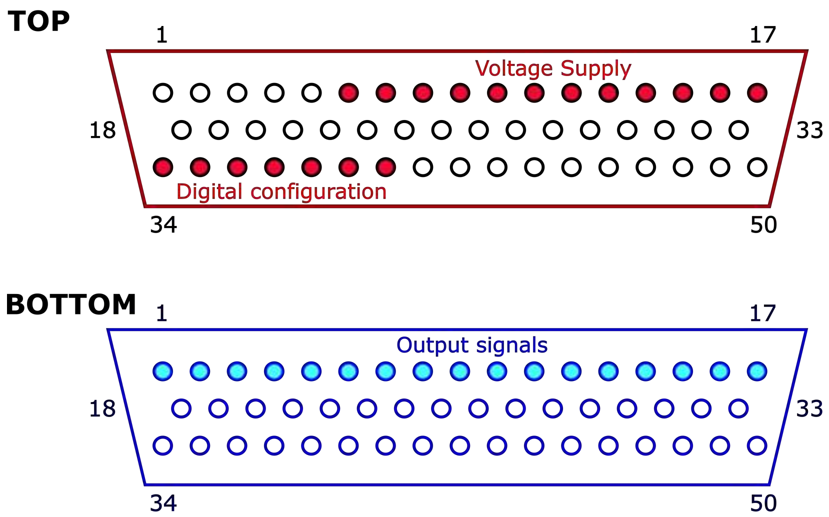

Figure 3.14: Pin assignment for top and bottom D-sub electrical feedthroughs

Table 3.5: Pin assignments for electrical feedthroughs (vacuum side).

D-sub	Pin number	Connection	D-sub	Pin number	Connection
TOP	6	SUB	BOTTOM	1	GND
	7	$VSSA$		2	$Sig0$
	8	$VDDA$		3	GND
	9	GND		4	$Sig1$
	10	V_{Ring1}		5	GND
	11	V_{Ring2}		6	$Sig2$
	12	V_{BackGate}		7	GND
	13	$V_{\text{BackFrame}}$		8	$Sig3$
	14	V_{temp}		9	GND
	15	$V_{\text{BackContact}}$		10	$Sig4$
	16	GND		11	GND
	17	I_{temp}		12	$Sig5$
	34	SIN		13	GND
	35	GND		14	$Sig6$
	36	$CK1$		15	GND
	37	GND		16	$Sig7$
	38	$CK2$		17	GND
	39	GND			
	40	LD			

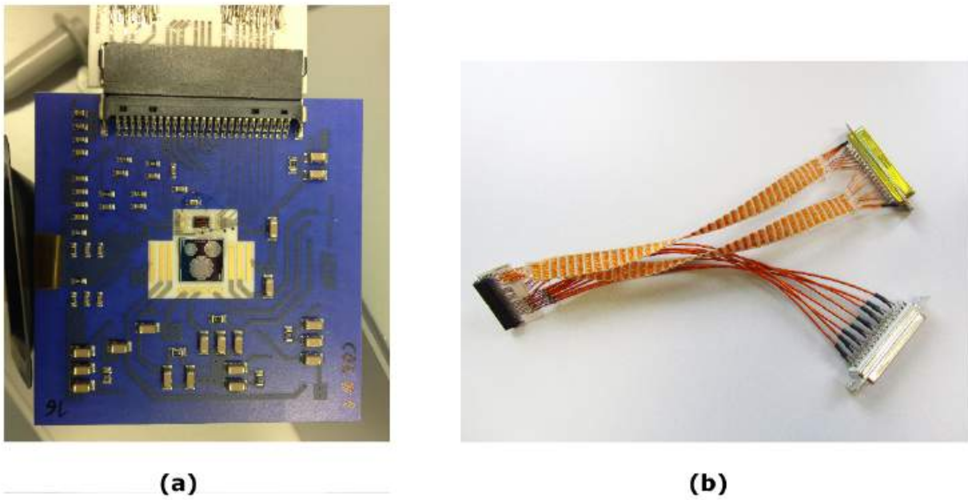

Figure 3.15: (a) Main PCB with bonded detectors and preamp chip, the adapter PCB is connected to the main PCB. **(b)** Ribbon cables and single capton cables connect the adapter PCB to two D-sub connectors with 50 pins each.

Air side

On air side, cables are guided to three different devices, see figure 3.16. A configuration board is needed to set the voltage configurations of the preamp chip and to provide the necessary clock signals. High voltage and low voltage supplies (*Wiener*) provide the required voltages for both sensor and preamp. A DAQ crate from IPE and a commercial STRUCK digitized can be accessed for data acquisition.

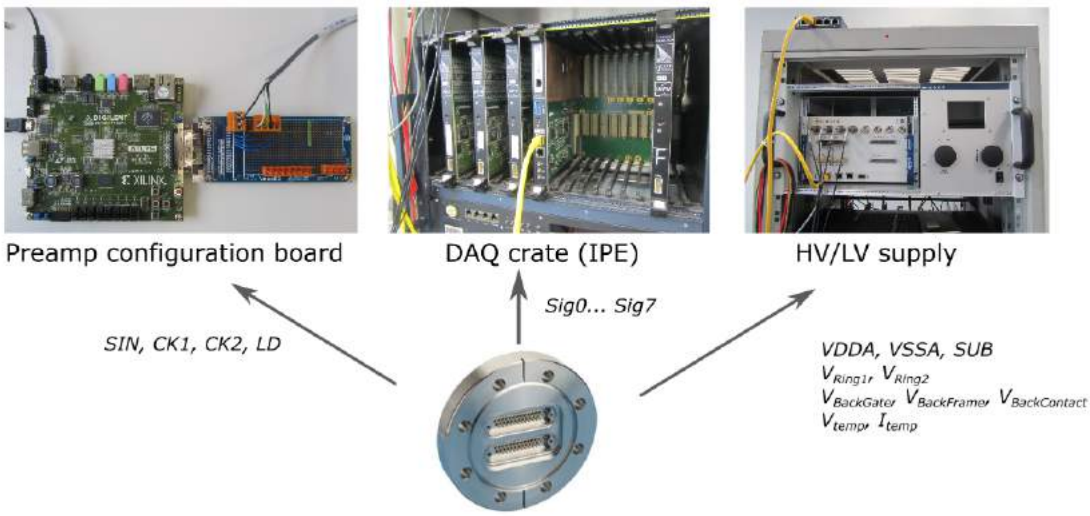

Figure 3.16: On air side, cables connect the D-sub feedthroughs with a preamp configuration board, a DAQ crate to read out and digitize the signals and HV/LV power supplies for both preamp and sensor.

3.4 First light of TRISTAN

Finally, a first measurement result of one of the TRISTAN prototype detectors is presented in this section. The measurement was performed with a ^{55}Fe source, a γ-source with $E_\gamma = 5.899$ keV and the central pixel of an HLL detector in the two-drift-ring design with a cell size of 250 μm. Figure 3.17 shows the first pulse, measured with an oscilloscope.

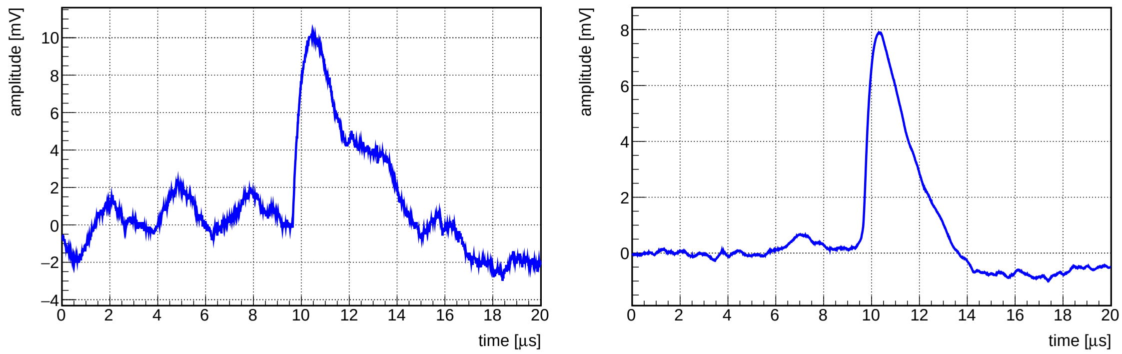

(a) **(b)**

Figure 3.17: (a) First ^{55}Fe γ-ray signal, measured with the TRISTAN prototype detector. **(b)** Signal after averaging over 128 samples.

In the measurement, the setup was not optimized for a low-noise performance. The detector was operated at room temperature, the applied bias and drift ring voltages were not optimized, and the grounding still needs to be improved. Consequently a high leakage noise is visible which leads to a signal-to-noise ratio of ≈ 4. Figure 3.17 (b) shows an average over 128 measured pulses.

The first test measurements approve the functionality of both preamplifier and detector, detailed investigations and optimizations are ongoing at the moment.

4 The impact of ADC Non-Linearities on the sensitivity to sterile neutrinos

Non-Linearities of Analog-to-Digital Converters (ADCs) are a major systematic effect for the sterile neutrino search with KATRIN. They provide errors on the measured particle energies and thus change the shape of the measured tritium β-decay spectrum. In order to reach the theoretically achievable sensitivity shown in figure 2.10, these resulting spectrum modifications need to be understood and mitigated to the ppm level.

This chapter gives an introduction to ADC Non-Linearities (NLs) and explains their origin (4.1.1). It displays a way to measure ADC Non-Linearities, shows experimental measurement results (4.1.2) and moreover demonstrates ways to perform NL corrections on real physics data (4.1.3).

In section 4.2 and 4.3 Monte Carlo and analytical simulation techniques are presented which investigate the impact of ADC Non-Linearities on the tritium β-decay spectrum. Mitigation methods are discussed and the final impact on the KATRIN sensitivity in respect to sterile neutrinos is analyzed in section 4.4.

4.1 ADC Non-Linearities

Non-Linearity is a very important parameter of every ADC and characterizes its imperfections and uncertainties due to the non-ideal, i.e. real components inside the ADC architecture.

4.1.1 Theory of ADC Non-Linearities

An ADC digitizes an input voltage with a certain resolution, depending on the number of bits. This yields a quantization error. For a theoretical ideal ADC, the

transfer function is a uniform step function with the same width for each step. However, due to the internal architecture with non-perfect components like capacitors and preamplifiers, as well as comparators and feedback Digital-to-Analog Converters (DACs), real ADCs show an additional intrinsic non-linear behaviour [73] which cannot be eliminated by energy calibration.
This behaviour is described by the Integral Non-Linearity (INL) which is defined as the deviation of the best-fit function to the ADC transfer function. Figure 4.1 shows the schematic transfer and best-fit functions of an ideal and a real ADC.

Mathematically, the INL is defined as

$$\mathrm{INL}[i] = \frac{U[i] - U_0}{U_{\mathrm{LSB}}} - i \tag{4.1}$$

where i is the number of the respective step in the transfer function, $U[i]$ the corresponding input voltage, U_0 the maximum input voltage to get 0 as ADC output code, and U_{LSB} indicates the voltage which would cause an ideal ADC to increase its output by 1 Least Significant Bit (LSB). INL is typically given in units of LSB.

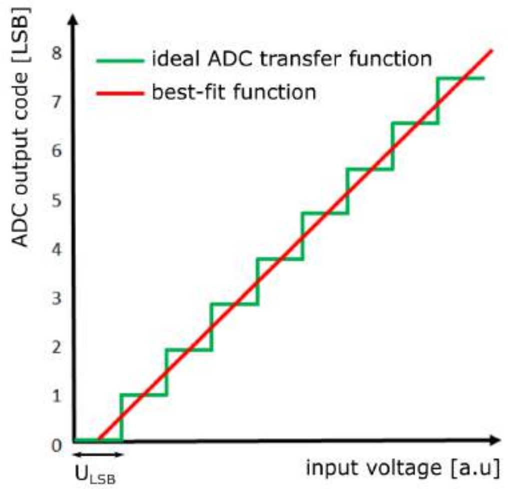

(a)

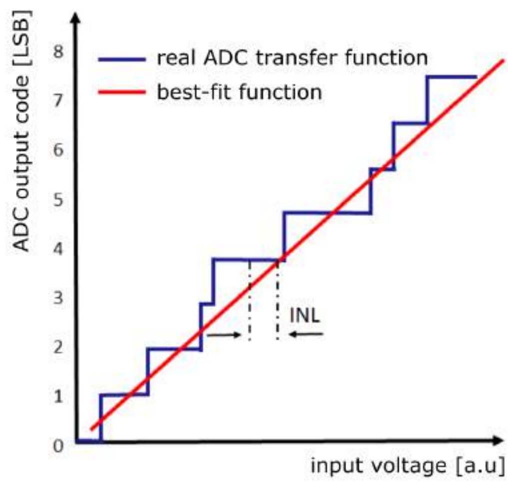

(b)

Figure 4.1: Schematic of the transfer function and best-fit function of an ideal linear ADC **(a)** and of a real ADC **(b)**. The ideal ADC has a uniform step width, the ADC output increases by one LSB (Least Significant Bit) for each voltage step U_{LSB}. However, for a real ADC the step widths differ and the deviation between the transfer and the best-fit function is called Integral Non-Linearity (INL).

Especially for a SAR-ADC (*Successive Approximation Register* - ADC), which has been used in the measurements described below, the INL shows a characteristic periodic structure. In a SAR-ADC the input voltage is successively compared to comparator voltages of the DAC and becomes more precise with each step of comparison. Due to this self-repeating process, the same NL structure appears consistently at different ADC output codes, i.e. ADC bins, and shows a repeating pattern in the INL spectrum [74].

4.1.2 Measurement of ADC Non-Linearities

ADC Non-Linearities cannot be avoided by simple energy calibration, therefore it is crucial to measure them to perform a correction of the data. Measurements to test the feasibility of NL corrections have been performed in a detector lab at Lawrence Berkeley National Laboratory (LBNL) in Berkeley/California.
The experimental setup consists of a function generator which generates pulses and sends them to a GRETINA digitizer, developed for the GRETINA (*Gamma-Ray Energy Tracking In-beam Nuclear Array*) experiment. The GRETINA digitizer has a sampling rate of 100 MHz and a 14-bits ADC resolution of monolithic SAR-ADCs, series AD6645 (*Analog Devices*). A functional block diagram of the ADC is shown in figure 4.2. The ADC has 2^{14} output codes from -8191 to 8192. More detailled specifications on the ADC can be found in [75].

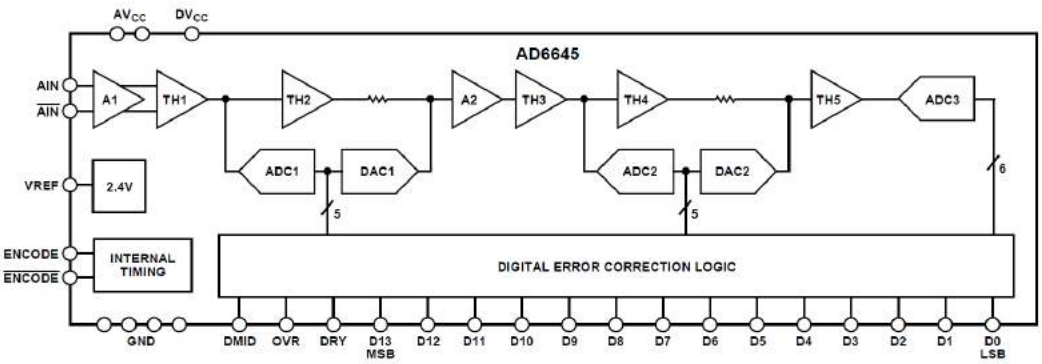

Figure 4.2: Functional block diagram of the AD6645 ADC. *AIN* is the input voltage, each *TH* triangle symbolizes a track-and-hold circuit, two internal Digital-to-Analog Converters (DAC) are on the chip. D0 ... D13 are the output bits of the ADC, D0 is the Least Significant Bit (LSB), D13 the Most Significant Bit (MSB).

The digitized data are processed by a single board computer and stored via an *ORCA*[8] interface, a data acquisition software. In the following, the precise procedure how to extract the INL spectrum from measured data is explained.

8 ***O**bject-oriented **R**eal-time **C**ontrol and **A**cquisition, developed at University of Carolina* [76].

Table 4.1: Settings for the two linear ramps of the function generator

	slow ramp	fast ramp
amplitude	2.5 V (-1.25 V to +1.25 V)	500 mV (-250 mV to + 250 mV)
period	10 s	1.5 ms
symmetry	100%	50%

Measurement procedure

The measurements have two goals. In a first step the INL of a SAR-ADC is determined, in a second step an INL correction is applied to physics data.
The measurement procedure requires two output signals of a function generator, following [77]. In the setup, an *Agilent 33500B Series* generator was used. The first signal is a slow increasing linear ramp, the second one a fast decreasing linear ramp. Table 4.1 lists the settings used for both ramp signals. The amplitudes were chosen in a way that the entire ADC range of the GRETINA digitizer is covered by the slow ramp.

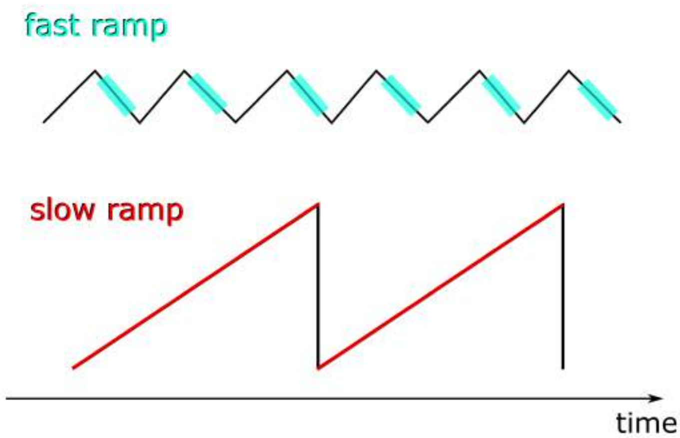

Figure 4.3: Schematic of INL measurement procedure. A fast ramp triangular signal is added to a slow ramp signal with small positive slope (red). The fast ramp is shifted by the slow ramp signal over the entire ADC range. The ADC is set to trigger on the falling edge of the fast triangular signal, recording a part of the decreasing slope (blue). Since, the triangular signal is shifted by the slow ramp, each of these recorded slopes spans a different ADC range.

By adding the two signals, the slow ramp will move the fast ramp over the entire ADC range. Figure 4.3 shows a schematic picture of the slow and fast ramp signals which are added.

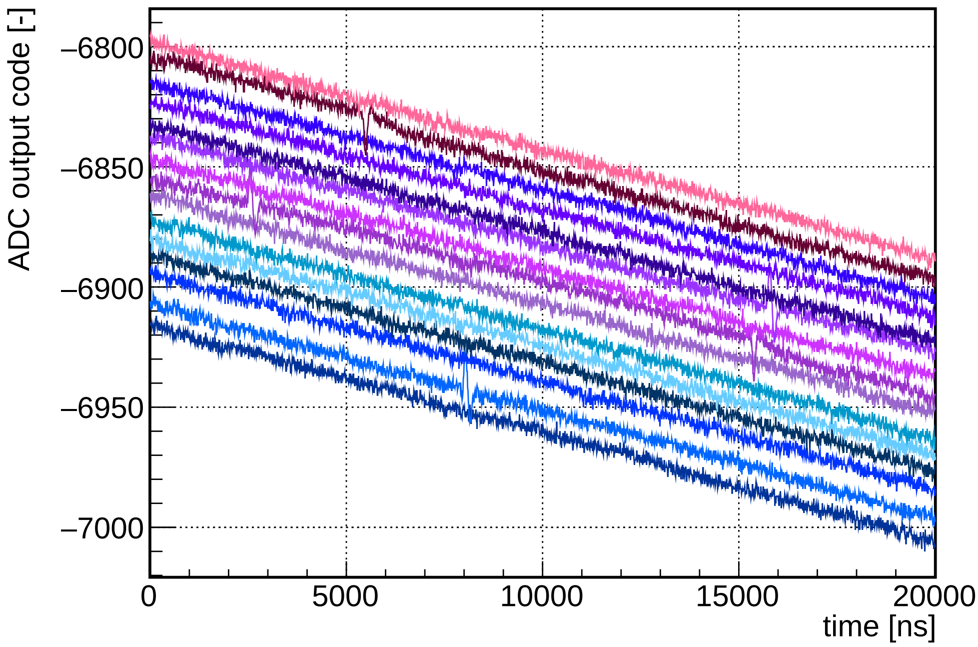

Figure 4.4: The entire ADC range is scanned by the fast ramp signal of the function generator which is shifted by the slow ramp signal. 15 examples of digitized waveforms are shown, each one has a length of 20 μs.

Figure 4.4 shows measured fast ramp waveforms which are moved by the slow ramp. The *sync* output of the fast ramp signal acts as an external trigger for the digitizer.

This novel measurement method has a huge advantage in contrast to the *histogram method*, well known from literature [78]:

In a classical histogram method, a high-quality pulse generator provides one ramp covering the entire ADC range, and one counts how often each ADC channel appears in the data stream. This classical method depends strongly on the linearity of the pulse generator. The method described in this section however is more independent of pulser linearities since the same fast-ramp waveform is reused over the entire ADC range, but shifted by the slow ramp. Any Non-Linearities in the fast ramp are averaged out, and the slow ramp has such a small slope that its Non-Linearities have a negligible impact.

Thanks to the differential input of the ADC, both the fast and the slow signal (as described above) can be fed to a single GRETINA card channel. In practice a 20 channel fanout cable is used to plug the output of both ramp signals into the differential input of one channel of the GRETINA digitizer (figure 4.5), where the two

Figure 4.5: GRETINA digitizer in a VME crate at LBNL. Two output signals of a function generator are inserted into the differential input of the GRETINA digitizer via a multi-wire fanout cable. The single cable above provides the digitizer with an external trigger set by the fast ramp signal. On board the signals get amplified and digitized with a sampling frequency of 100 MHz.

signals are added. Many waveforms of length 20 μs are collected, triggered by the start of the fast ramp. Any specific ADC channel occurs in many of those waveforms, but at different sample times (i.e. different points in the fast ramp waveform), as the difference between the two ramps spans the ADC range. Thus any small analog Non-Linearities in the fast input waveform are averaged away, and a very high-quality pulse generator is no longer required.

The individual waveforms are stored via the *ORCA* interface with a length of 20 μs for each waveform. In the measurements waveforms have been recorded for six different channels. Large amounts of samples were taken to reduce noise contributions.

Extraction of ADC Non-Linearities from the data

The basic idea how to extract the Non-Linearity out of the measured waveforms is to compare the expected number of counts to the actual number of counts per ADC output code [79]. The ratio of those is basically the INL of the ADC.

In the first step, each single waveform is projected onto the y-axis of figure 4.4 in a way that the highest and lowest ADC values are discarded to avoid edge effects. This projection yields the actual number of hits for each ADC output code in the ADC range. Secondly, this number is normalized to the expected number of counts which is derived by counting how often each ADC channel would be reached, assuming that each waveform would cover a certain ADC range in a perfectly linear way. Figure 4.6 illustrates the results of both projection and normalization.

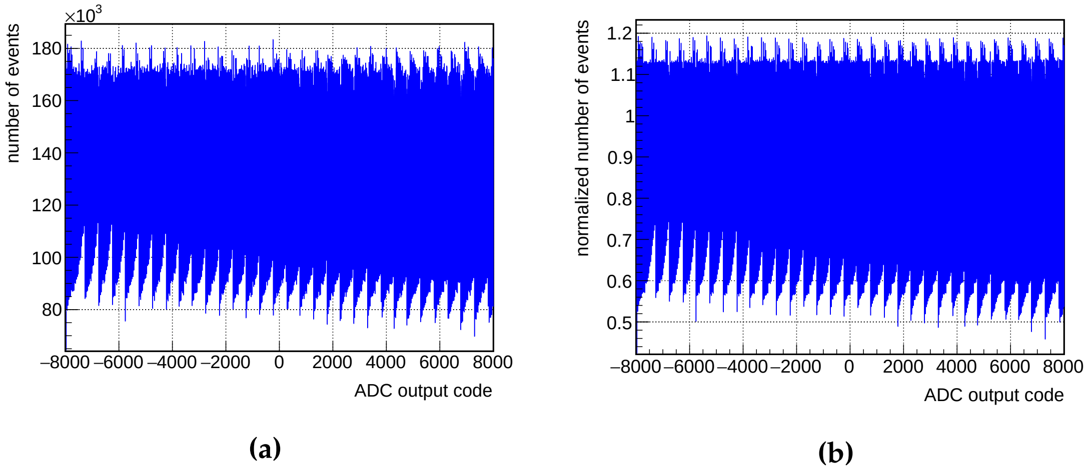

Figure 4.6: (a) The digitized waveforms are projected on the ADC output code to get the number of events for each output code. A repeating pattern can clearly be seen in the number of events, caused by the NL. **(b)** The number of events is normalized to the expected number of events without any ADC Non-Linearities.

In a third step, the values of the normalized number of events are added successively from the lowest to the highest ADC output code. This yields an ADC transfer function comparable to the one introduced in figure 4.1. The deviation between the resulting step function and the best-fit function provides the Integral Non-Linearity given in units of LSB. Its periodic structure, seen in figure 4.7, occurs due to the internal self-repeating comparator structure of a SAR-ADC. It reveals the number of internal comparison steps between the input voltage and the DAC comparators:

a) Looking at the entire ADC range of the INL spectrum, $2^5 = 32$ saw-teeth can be seen. They expose the discontinuities when switching between ADC ranges. This saw-tooth pattern indicates a 5-bits comparison in the first approximation step of the ADC, the most rough comparison which leads to a large-scale structure in the INL spectrum.
b) A zoom into the ADC output code region discloses $2^4 = 16$ identical peak-like medium-scale peaks between each of the big steps, merely shifted in their range. The second comparison is a 4-bits comparison.
c) The last approximation step compares the voltages with the maximum resolution of 1 LSB and provides a small-scale structure. There are $2^5 = 32$ ADC output

codes between each of the medium scale peaks, indicating a 5-bits comparison in the third approximation step.

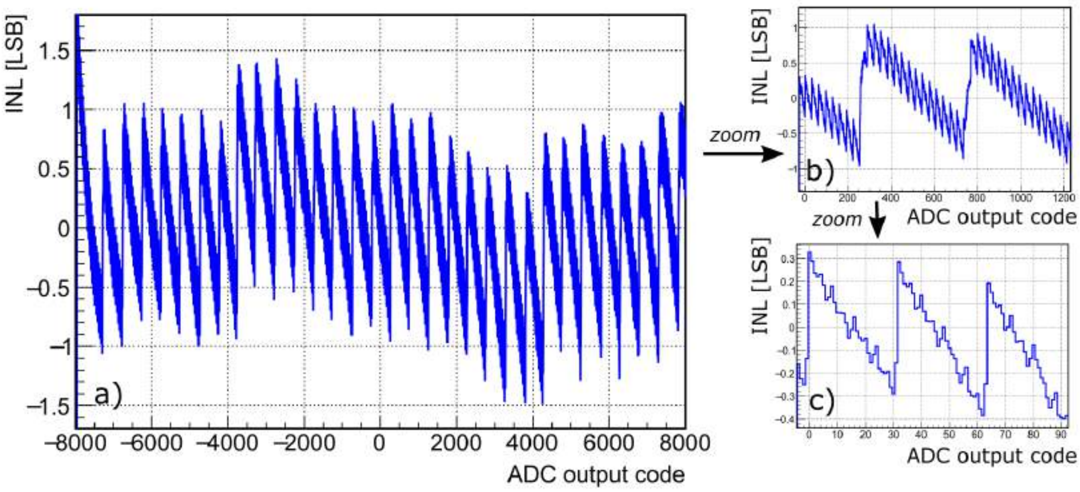

Figure 4.7: Integral Non-Linearity of the GRETINA SAR-ADC. The periodic structure reveals the internal structure of the comparators inside the ADC as a 5 bits/4 bits/5 bits comparator with the respective three steps of successive approximations.

Conclusion

The Integral Non-Linearity of an ADC AD6645 was measured with a new method which is independent of waveform generator Non-Linearities. The results show INLs of the order of ±1.5 LSB. A periodic structure is clearly visible as expected for a successive approximation digitizer. Measurements of all six GRETINA card channels have been performed. Channel 1 is presented as an example.

4.1.3 Non-Linearity corrections on real physics data

This section demonstrates, how to apply a NL correction to real physics data. Starting from measuring γ-spectra, the signals get shaped by a trapezoidal filter and provide a measurement of the energy, which is displayed in an energy histogram. A NL correction can be applied directly to the stored signal waveforms before shaping them.

Setup and measurement

The goal of this measurement was, to test the feasibility of a NL correction. For this purpose, γ-spectra were measured and digitized with the same ADC, whose INL spectrum was determined in the measurement described in section 4.1.2. A cryogenic germanium *p-type* point contact (PPC) detector (figure 4.9) of the *Majorana* experiment [80, 81], which searches for neutrinoless double β-decay, was used in order to record γ-spectra of ^{133}Ba and ^{60}Co. The detector was cooled down with liquid nitrogen and was connected via an amplifier board to the GRETINA digitizer. The setup is shown in figure 4.8.

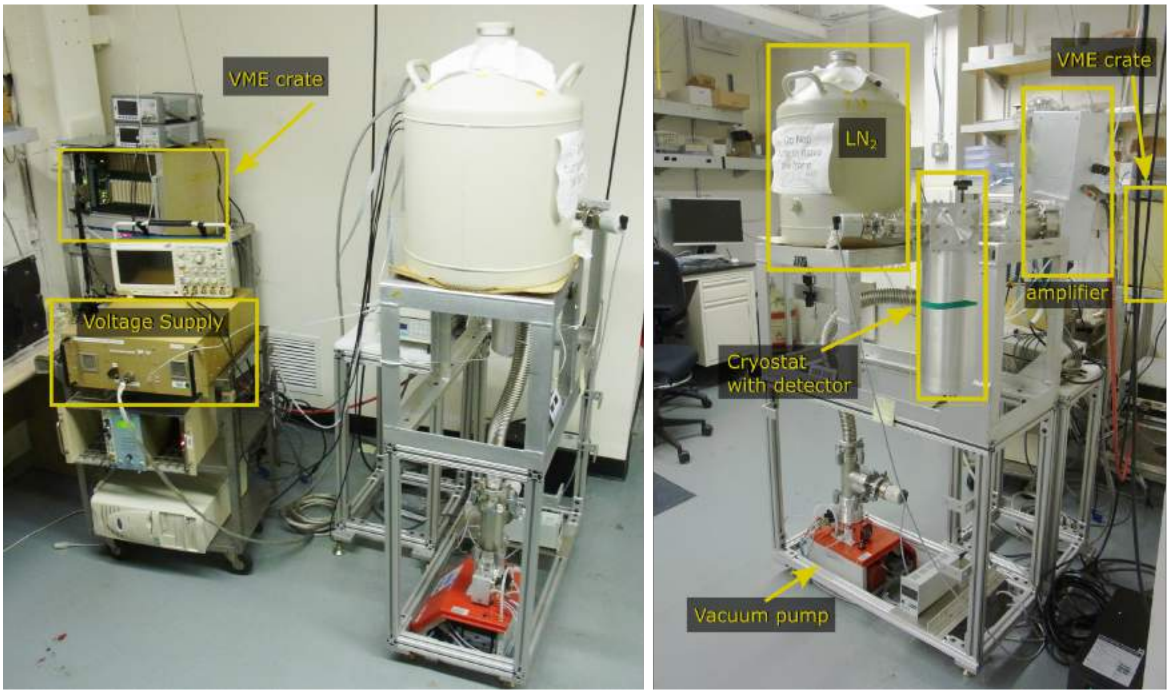

Figure 4.8: Measurement setup at LBNL: A germanium detector is fixed in a cryostat, cooled with liquid nitrogen (LN_2). It is connected to an amplifier board from where the signals are guided to the GRETINA digitizer in the VME crate. Two γ-ray sources of ^{133}Ba and ^{60}Co were put next to the cryostat to measure energy spectra with the cryogenic germanium point contact detector.

^{133}Ba disintegrates to ^{133}Cs via electron capture and emits four prominent γs with energies of 276 keV, 302 keV, 356 keV and 383 keV. ^{60}Co decays via β-decay to ^{60}Ni with a half-life time of $T_{1/2} = 1925.5$ d, emits an electron with endpoint 317.9 keV and two γs with 1.173 MeV and 1.332 MeV, as listed in table 4.2 [82, 83]. The γ-rays reach the germanium detector and create electron-hole-pairs inside the reverse biased sensor. The holes are pulled to the small point contact anode of the detector, the electrons move towards a lithiated n+ contact [80]. A capacitor of a

Table 4.2: γ-ray emission energies of ^{133}Ba and ^{60}Co

	Energy [keV]	Photons (per 100 disintegrations)
^{133}Ba	276.3989	7.16
	302.8508	18.34
	356.0129	62.05
	383.8485	8.94
^{60}Co	1173.228	99.85
	1332.492	99.9826

charge-sensitive feedback amplifier is charged up and a signal with a sharp rising edge is created. The height of this signal is proportional to the amount of charge released inside the detector by the γ-rays, and therefore to the energy deposited in the detector. The collected charge is then slowly drained away through a resistor, resulting in an exponentially decaying voltage drop.

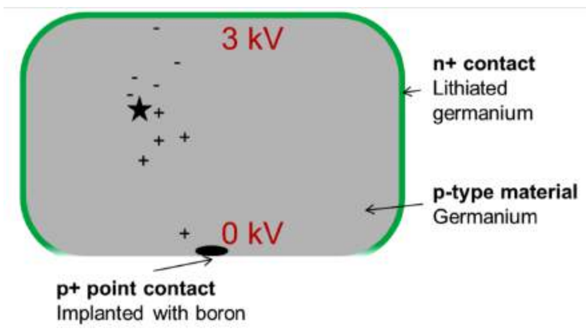

Figure 4.9: Schematic view of the used *Majorana* germanium *p-type* point contact detector [80]. The point contact is set to 0 V, the surrounding *n-type* contact is set on positive high voltage. If an ionizing particles enters the detector, electron-hole pairs are created. The holes move to the point contact, electrons to the positive *n+* contact.

The amplified signals are transported to the GRETINA digitizer which samples the signals with a sampling frequency of 100 MHz . With the *ORCA* interface each single digitized waveform is stored. Figure 4.10 shows typical waveforms with different energies, as they were measured in the setup. Their height is proportional to the respective energies of the γ hitting the detector, the baseline shifts occur due to the high rate of incident particles.

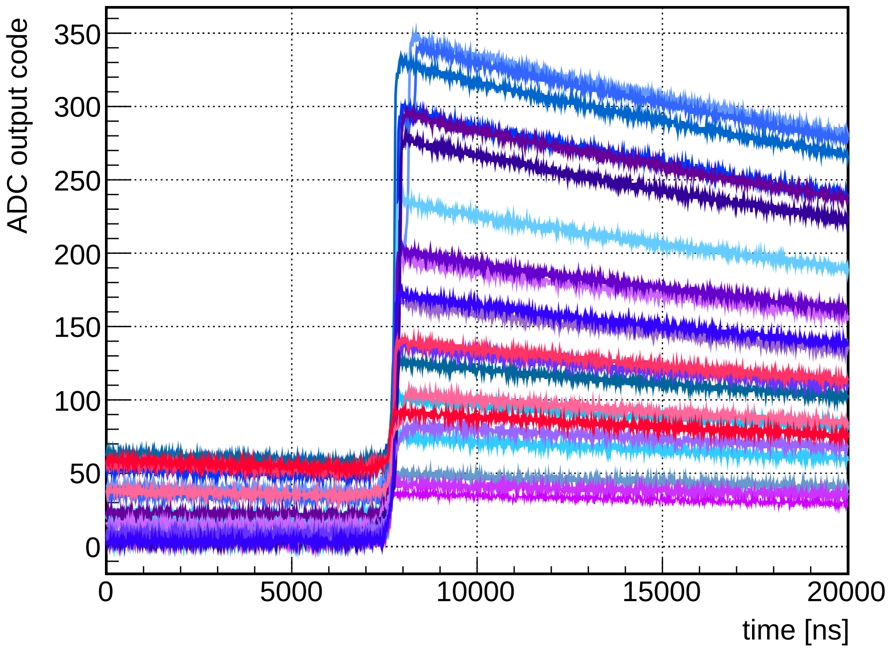

Figure 4.10: Waveforms of γ-ray measurements. If γs hit the detector at a high rate, a new waveform sits on the exponentially decaying tail of a previous one. This explains the baseline shifts. The signal height is proportional to the energy of the incident particle.

Filtering and histograming of the data

In spectroscopy, trapezoidal filters have proved their suitability in shaping exponentially decaying digital signals. They take over the role of analog shaping amplifiers [84]. In figure 4.11 the working principle of a trapezoidal filter is shown. It has two parameters which specify the filter configuration: the rise time t_{rise} and the flat-top time t_{flattop}. Two regions S1 and S2 are defined which are separated by t_{flattop}. For each point of the waveform the parameter E (the difference of the sum of ADC values in S1 and S2)

$$E = \frac{1}{t_{\text{rise}}} \left(\sum_{\text{S2}} \text{wave}[t] - \sum_{\text{S1}} \text{wave}[t] \right) \tag{4.2}$$

is calculated, where wave$[t]$ denotes the ADC output code at time step t. The filter output has a trapezoidal shape, the middle value of the flat top is taken as the filter output, i.e. the particle energy E [85]. Due to the averaging over several wave points within the intervals S1 and S2, the noise dependency is reduced, making the amplitude determination more stable.

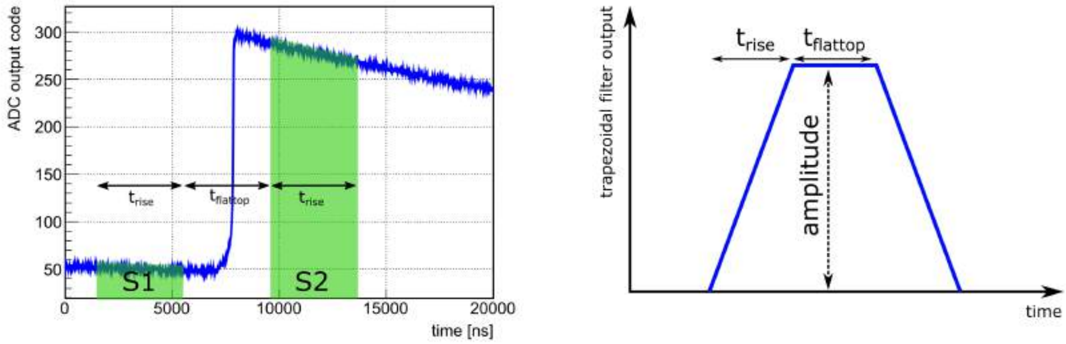

(a) **(b)**

Figure 4.11: Schematic of a trapezoidal filter. **(a)** For each point of the waveform the difference of the sums in the regions S2 and S1 is calculated and normalized to the number of sampling points in each of the regions. **(b)** Schematic of a trapezoidal filter output. The middle flat-top value of the filter output yields an amplitude proportional to the particle's energy.

The trapezoidal filter is applied to every recorded waveform. Figure 4.12 shows the resulting histogram containing the output amplitudes of the trapezoidal filter for the measured γ-ray spectra. The filter parameters were set to $t_{\text{rise}} = 4\ \mu s$ and $t_{\text{flat}} = 4.5\ \mu s$.

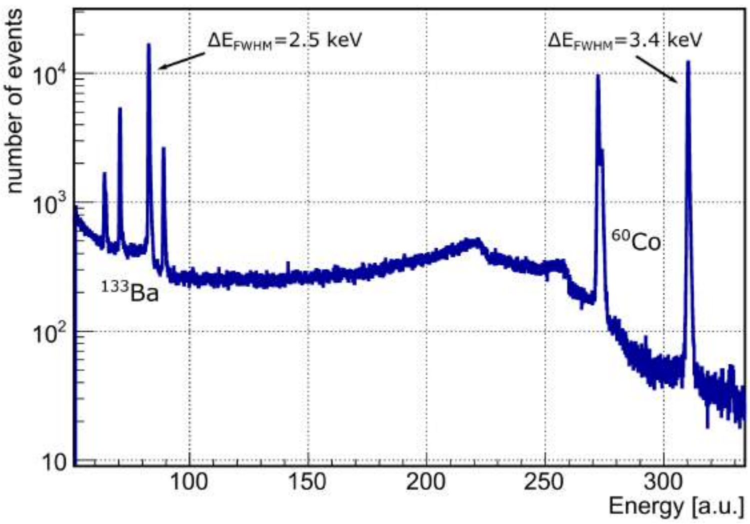

Figure 4.12: Energy spectrum, measured with the germanium *Majorana* PPC detector. The four ^{133}Ba and two ^{60}Co peaks are clearly visible. The energies correspond to the respective amplitudes of the trapezoidal filter output. Calibration of the data yields resolutions of $\Delta E_{\text{FWHM}} = 2.5$ keV for the strongest ^{133}Ba peak at $E = 356$ keV and $\Delta E_{\text{FWHM}} = 3.4$ keV for the right ^{60}Co peak at $E = 1332$ keV.

Non-Linearity correction

Up to this step, no Non-Linearity correction has been applied to the waveforms. To correct for the ADC Non-Linearities, each individual digitized data point wave[t], i.e. the ADC output code for the wave at time step t, of each single waveform is corrected with the respective INL value of its ADC output code. Thus, the respective INL value is subtracted from the data point ADC output code:

$$\text{wave}[t] \rightarrow \text{wave}[t] - \text{INL}(\text{wave}[t]). \tag{4.3}$$

Afterwards the signals get shaped by the trapezoidal filter. Figure 4.13 gives an overview on the main steps in the measurement and analysis procedure and displays the occurrence of the Non-Linearity correction.

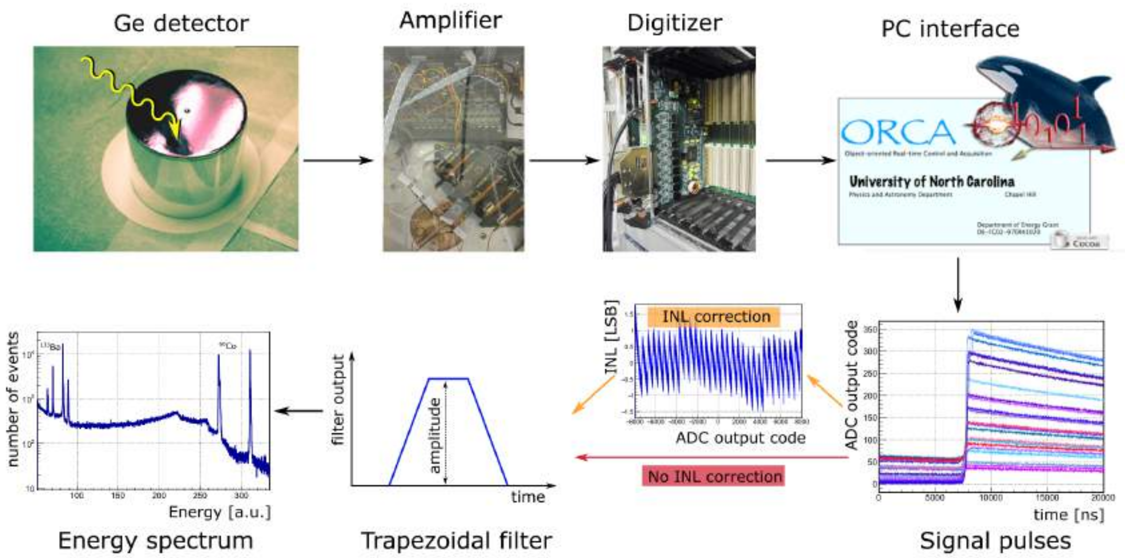

Figure 4.13: Schematic drawing of the individual steps from a γ, hitting the detector to the final energy spectrum. Before applying the trapezoidal filter the Non-Linearity correction is applied by correcting each data point of the signals according to the INL of its respective ADC output code.

Comparing the energy spectra with and without Non-Linearity correction demonstrates the impact ADC Non-Linearities have on the spectrum. The displayed ^{133}Ba peaks in figure 4.14 are clearly shifted after the correction.

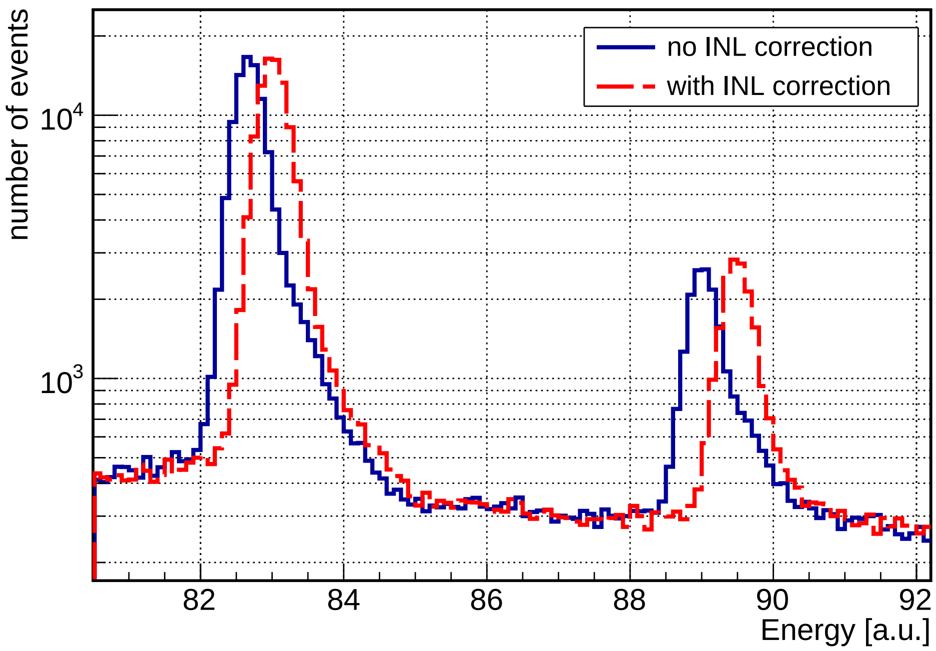

Figure 4.14: Comparison of γ energy spectra of ^{133}Ba with and without correction of ADC Non-Linearities. The Non-Linearities considerably change the spectrum.

Evaluation of the NL correction

To quantify the goodness of the NL correction, the residual Non-Linearity is calculated with the following steps:

- For both the corrected and the uncorrected energy spectrum a calibration is performed. The theoretical peak energies (see table 4.2) are plotted against the peak positions in the measured spectra which are obtained by Gaussian fits.

- For both cases the points are fitted with a linear calibration function respectively and the difference ΔE between the fit value and the theoretical energy is displayed against the theoretical peak energy.

Figure 4.16 illustrates the residual NL of the measured γ-spectra. The ΔE errors are clearly reduced by the NL corrections, but show an over-correction of the residual NL. An average error reduction factor $r_f = 1.85$ is obtained.

$$r_f = \left(\sum_{i=1}^{6} \frac{|\Delta E| \text{ at peak position } i \text{ with NL correction}}{|\Delta E| \text{ at peak position } i \text{ without NL correction}} \right) \cdot \frac{1}{6} = 1.85 \qquad (4.4)$$

Further improvement of the NL correction

The Non-Linearity correction can be further improved by applying more sophisticated correction methods on the data. In the described measurement and correction procedure above, the real physics data are corrected by subtracting the respective INL values from the data points. The INL values were obtained by ramping through the ADC range, using a ramp with a constant negative slope and counting how often each channel has fired. However, ADC Non-Linearities also depend on the signal slope, both on speed and sign, revealing a hysteresis behaviour [86]. Figure 4.15 displays the INL dependencies on ramp speed and sign of the slope.

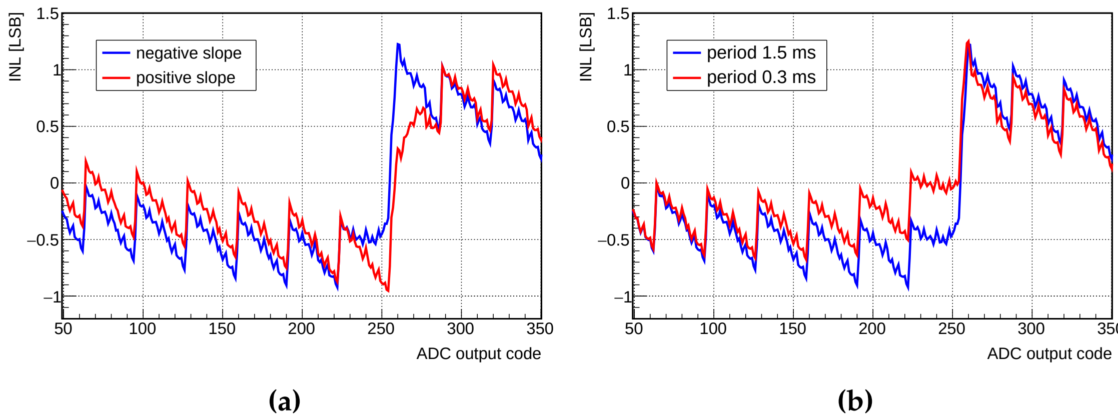

Figure 4.15: **(a)** The INL spectra, determined using input ramps with positive or negative slope, differ especially at the positions of the big saw-teeth and show a hysteresis behaviour. **(b)** The INL not only depends on the sign, but also on the value of the input slope. Here, two different ramps with periods of 0.3 ms and 1.5 ms were used which therefore cover different ADC ranges in the analysis time window of 20 μs.

A waveform, corresponding to a real physics event, entails a number of different slopes (see figure 4.10), such as a flat baseline, a steep rise and an exponential decay. These slopes depend on the energy of the event: Large energy events result in a high signal amplitude and a large negative slope in the decaying signal. Small energies yield smaller slopes. This observation is crucial for the application of a NL correction. It means, that the measured NL with the pulse generator is different from the NL, present during the calibration runs with a γ source. This effect can be partially compensated by averaging INL spectra obtained by fast ramps with different slopes. Using this method, figure 4.16 presents an improvement of the residual Non-Linearity for the γ-spectra measurements. The average reduction factor r_f of the residual Non-Linearity, defined in equation 4.4, for the averaged INL is

$$r_f(\text{averaged INL}) = 3.74, \tag{4.5}$$

showing an improvement by a factor of two, compared to the standard correction method. Initial studies have shown that further improvements are possible. A detailed investigation of these methods is ongoing at the moment.

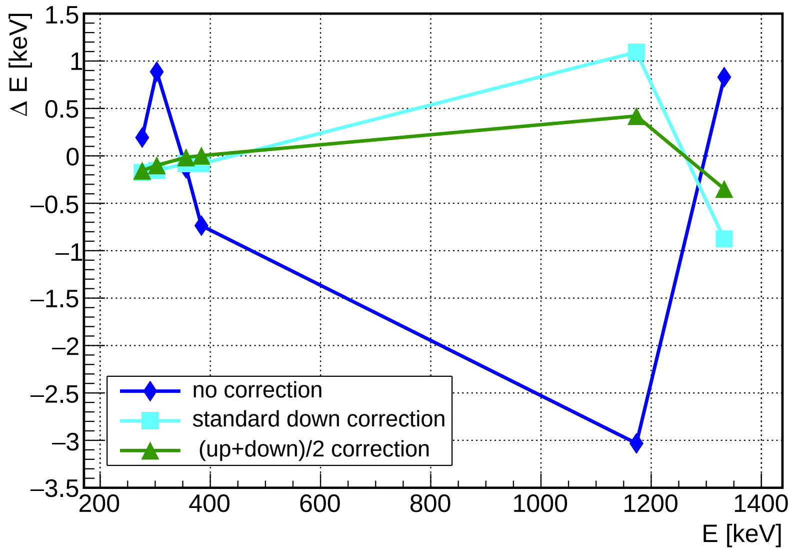

Figure 4.16: Residual Non-Linearity, i.e. the difference ΔE between the calibration fit values and the theoretical peak energies of ^{133}Ba and ^{60}Co spectra with and without NL corrections. The effect of the NL is clearly reduced by applying the standard correction with INL spectra, obtained by negative ramps with constant slope. However, this simple method seems to overcorrect the effect of the NL. The residual Non-Linearity can further be diminished by using an averaged INL considering the INL measurements with positive (up) and negative (down) ramp.

4.1.4 Conclusion

In this section it was shown that ADC Non-Linearities can be measured efficiently with the described method of shifting a fast ramp signal of a pulser trough the entire ADC range. A NL correction for real physics data of γ-ray spectra, recorded with a waveform-digitizing ADC, was demonstrated by correcting each individual sampling point with the respective INL deviation. As ADC Non-Linearities depend on the signal slope, a NL correction with an averaged INL further improves the correction and mitigates the residual ADC Non-Linearity.

4.2 Monte Carlo model for a single pixel detector

Having scrutinized the origin and properties of ADC Non-Linearities in section 4.1, this section is dedicated to Monte Carlo simulations to investigate the impact of ADC Non-Linearities on the tritium β-decay spectrum. The examinations are based on signal pulse simulations as they come out of a silicon detector and the resulting impacts on tritium β-decay spectra are compared for peak-sensing and waveform-digitizing ADCs. The simulations use input of the software *siggen*[9], a signal generator of pulses coming from semiconductor detectors.

4.2.1 Pulse train

The simulation uses a pulse train, a long series of pulses, whose energies are drawn from a probability density function (PDF), which corresponds to the tritium decay rate, given by

$$\frac{d\Gamma}{dE} = C \cdot F(E, Z=2) \cdot p \cdot (E + m_e) \cdot (E_0 - E)\sqrt{(E_0 - E)^2 - m_\nu^2}, \tag{4.6}$$

where E is the kinetic electron energy, m_e and m_ν are the electron and neutrino mass, E_0 is the endpoint for $m_\nu = 0$. C is a normalization factor given by

$$\frac{G_F^2}{2\pi^3} cos^2\Theta_C |M|^2, \tag{4.7}$$

where G_F is the Fermi constant, Θ_C is the Cabbibo angle and M denotes the nuclear transition matrix element.
The time between two pulses is drawn from an exponential distribution at a rate of 100 kHz.

Inversion method to draw random values according to a PDF

To create random numbers, following an arbitrary PDF, e.g. equation 4.6, the *Inversion method* is used [87]. Let $F(x)$ be the cumulative density function (CDF) of a PDF $f(x)$ and u a uniform $[0, 1]$ random variable, then $F^{-1}(u) = x$ and x is drawn from $f(x)$.
Figure 4.17 illustrates the PDF, CDF and inverse CDF^{-1} of the tritium decay rate.
In the following simulations, uniform distributed random numbers u between 1 and 10^4 are drawn from the CDF^{-1} distribution and the energies $CDF^{-1}(u)$ are

9 *siggen* was developed by I-Yang Lee (LBNL), Karin Lagergren and David Radford (ORNL).

assigned. The resulting energy spectrum follows the desired tritium decay rate distribution.

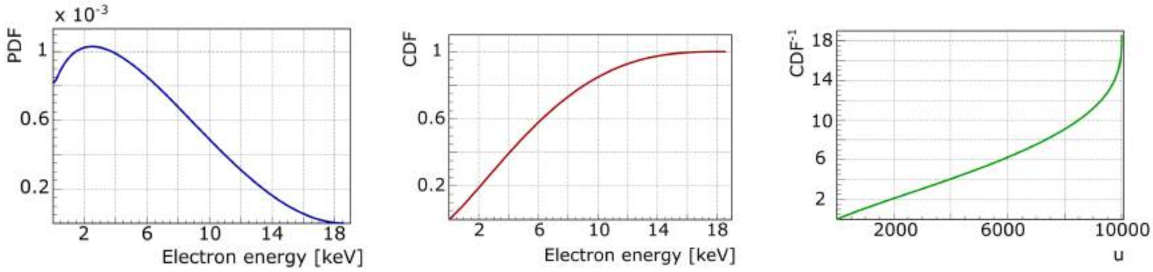

(a) **(b)** **(c)**

Figure 4.17: Inversion method to generate random numbers following the PDF **(a)** of the tritium decay rate. Iterative adding of the PDF values yields the CDF **(b)**. For uniform distributed random number u, its inverse $CDF^{-1}(u)$ can be used to generate samples following the tritium decay PDF **(c)**.

Pulse train results

For each single pulse, both energy and time to the next pulse are drawn randomly from the PDFs described above. Figure 4.18 shows an excerpt of the resulting output pulse train of the MC simulation, i.e. a pulse train, such as a continuously digitizing ADC would see. A random Gaussian noise with an RMS of 0.4 keV is added to the pulses.

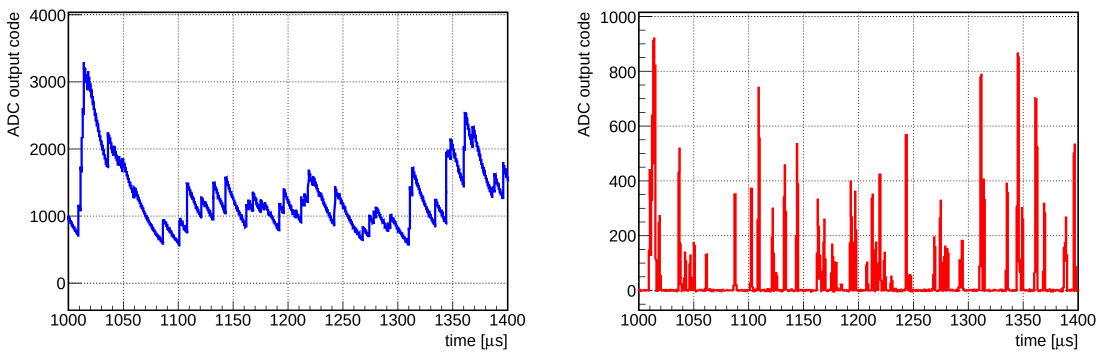

(a) **(b)**

Figure 4.18: **(a)** Excerpt of a simulated pulse train. Each pulse corresponds to an electron which creates a charge signal in a silicon detector. **(b)** After amplification and application of a trapezoidal filter, the peak heights of the shaped signals are used as a quantity which is proportional to the energies of the incident particles.

The signal heights vary according to the particles' energies. Due to the high rate, the baseline does not return to ADC output code = 0, but the pulses often sit on the

still high tail of a previous signal. If two pulses appear within a very short time window, *pile-up* occurs.
The pulse train gets scanned by a trapezoidal filter with a rise time of 1 μs and flat time of 0.1 μs. The resulting peak heights are histogramed and yield an energy spectrum. For pile-up events, however, it can occur that the trapezoidal filter cannot resolve the events and returns a weighted sum of the respective particle energies instead of two individual energy events. This has to be taken into account in an experiment.
At this point the Integral Non-Linearity enters the simulation. To investigate the impact of the INL on the resulting energy spectrum, the measured INL of the GRETINA-ADC (see figure 4.7) and simulated INL spectra, based on the measurements, are used as an input to the following simulations.

4.2.2 Simulation of INL spectra

With regard to subsequent investigations of the INL impact for a multi-pixel detector, where each pixel is read out by a separate ADC with a specific INL spectrum, a model was developed to randomly generate INL spectra of a 14-bits SAR-ADC with three comparison steps (5-bits, 4-bits, 5-bits), as it is used in the GRETINA digitizer.
The self-repeating structure of a SAR-ADC is implemented in the following way (a graphical example is shown in figure 4.19):

- The ADC output range $-8191...8192$ is divided into $2^5 = 32$ steps. Their INL values are drawn from a Gaussian distribution in a way which provides amplitudes of the order of the measured INL (≈ 1 LSB). These steps represent a simple realization of the large-scale structure in the INL spectrum **(a)**.

- Each large-scale step is divided into $2^4 = 16$ steps, for each one an amplitude is drawn from another Gaussian to simulate the second comparison step in the ADC. This medium-scale structure repeats itself for each single large-scale step **(b)**.

- Finally each medium-scale step is divided into $2^5 = 32$ small-scale steps, where one step corresponds to one ADC output code. Again the amplitudes are drawn from a Gaussian and replicate themselves for each medium-scale step in the INL spectrum **(c)**.

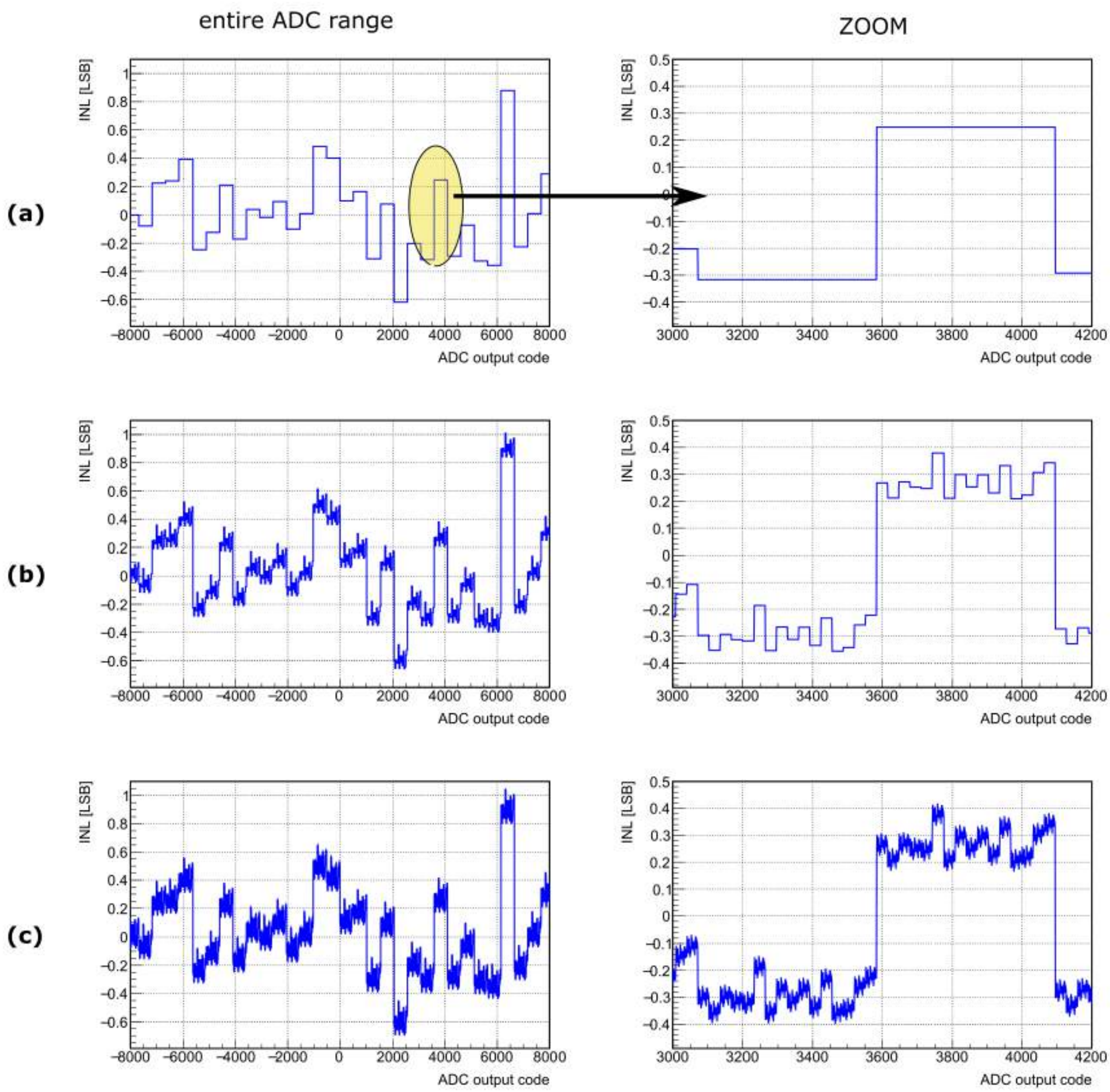

Figure 4.19: Simulation of INL spectra of a 14-bits SAR-ADC (5 bits + 4 bits + 5 bits). **(a)** The ADC range is firstly devided into $2^5 = 32$ steps to simulate the first ADC comparison step. The amplitudes are drawn from a Gaussian. **(b)** A medium-scale structure is added repetitively to each large-scale step. **(c)** A self-repeating small-scale structure is added to each medium-scale step.

Running the code n times, generates n different INL spectra which simulate n identically constructed SAR-ADCs, i.e. the step positions are the same for all INL spectra, but both amplitudes and internal structures of the INL fluctuations differ for each ADC, as it is the case in reality with non-ideal ADCs.

4.2.3 INL de-correction of simulated data

The basic idea of modelling the impact of ADC Non-Linearities on the tritium β-decay spectrum is to artificially modify, i.e. de-correct simulated data according to INL spectra by adding INL values to the respective ADC output codes. Two different approaches are followed which correspond to two different ways of digitizing data:

- **Peak-sensing ADC**: In this scenario, the waveforms are shaped, but only the digitized values of the peak heights $E(i)$ are stored. The respective INL values $\mathrm{INL}(i)$ are added to the peak heights and de-correct the data:

$$E_{\mathrm{INL}}(i) = E(i) + \mathrm{INL}(i). \tag{4.8}$$

- **Waveform-digitizing ADC**: In this mode, the entire waveform $\mathrm{wave}[t]$ is sampled and digitized, each single waveform point at time step t is de-corrected with the respective INL value:

$$\mathrm{wave}_{\mathrm{INL}}[t] = \mathrm{wave}[t] + \mathrm{INL}(\mathrm{wave}[t]). \tag{4.9}$$

The major difference between the two methods is that for the peak-sensing ADC a specific energy will always correspond to the same ADC channel. In contrast, a digitized waveform of a given energy will be composed of several different ADC channels that can span the entire ADC range (in case the baseline varies).
Accordingly, we expect that the effect of NL is washed-out more in case of the usage of a waveform-digitizer.
In the following, these two methods are investigated and their pros and cons for a real experimental setup are discussed.

Peak-sensing ADC

The principle of a peak-sensing ADC is modelled as follows: A MC pulse train of 10^8 pulses is created, the energies, i.e. the outputs of a trapezoidal filter, are stored, being the respective output codes of a peak-sensing ADC. Figure 4.20 shows the resulting tritium β-decay spectrum after histograming the INL de-corrected energy outputs of the trapezoidal filter.
The INL structure directly translates into the energy spectrum and yields significant

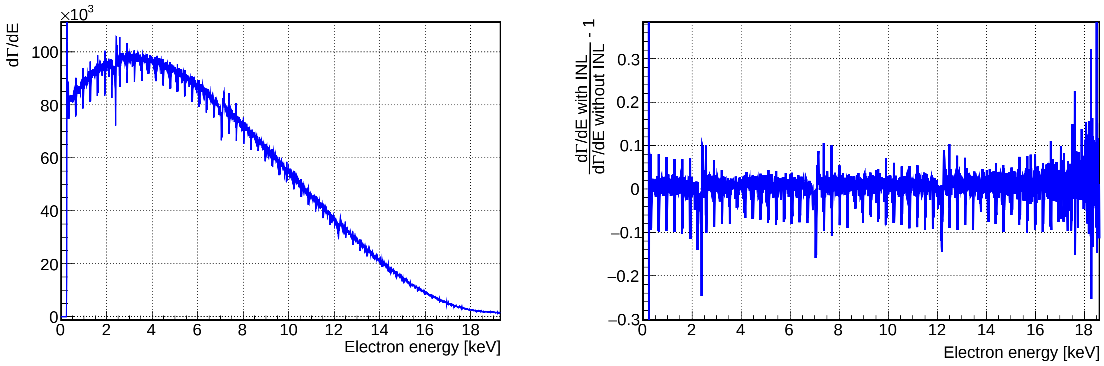

(a) **(b)**

Figure 4.20: (a) Tritium β-decay spectrum for 10^8 simulated signal pulses, whose energy outputs from the trapezoidal filter are de-corrected according to the INL value of the respective ADC output codes, modelling the working principle of a peak-sensing ADC. The steps in the INL are directly transfered into the resulting energy spectrum. **(b)** Shifted ratio of tritium β-decay spectra with and without INL.

distortions of the spectrum shape. To quantify them, the ratio

$$\frac{d\Gamma/dE \text{ with INL}}{d\Gamma/dE \text{ without INL}} - 1 \tag{4.10}$$

is calculated. It shows INL-induced fluctuations of the order of 10%. The large peaks (e.g. at 2 keV or 7 keV) correspond to the large-scale structure in the INL spectrum, caused by the first comparison step of the SAR-ADC.

Mitigation with a *Gatti slider*

To reduce the effect of the periodic structure in the INL, a mitigation technique can be applied by artificially shifting pulses to a different ADC range. This can be experimentally done by a *Gatti slider*, named after the Italian professor Emilio Gatti [88]: A voltage is generated by a DAC of an N bit counter (e.g. N = 6) and is added to the analog input signal of the ADC. After digitization, the digital counter value is subtracted again to obtain the digital value of the pure input signal. The counter is increased by 1 after each pulse and is reset after a whole cycle of 2^N pulses.
Figure 4.21 **(a)** shows the ratio with/without INL for the usage of a 6-bit *Gatti slider*. The spectrum distortions are reduced, but the bumps at the position of the big INL steps, e.g. at 2 keV , can still be seen.

Waveform-digitizing ADC

Another approach is to digitize the entire waveform, then de-correct the ADC output codes according to the respective INL values and finally obtain the energy as the amplitude of the trapezoidal filter. This method has a major advantage in comparison to the peak-sensing ADC: It is sensitive to the baseline of each signal. As shown in figure 4.18, the baseline shifts widely through the ADC range due to the high signal rate. Hence, also signals with the same signal height experience a different output from the trapezoidal filter, as they see different INL values at different ADC output codes. In contrast, in the peak-sensing case only the difference between baseline and signal height is digitized, making the result independent of the baseline. Therefore the baseline shift has to be added artificially using a *Gatti slider*, in the waveform-digitizing scenario it is included naturally, compare the two plots of figure 4.21.

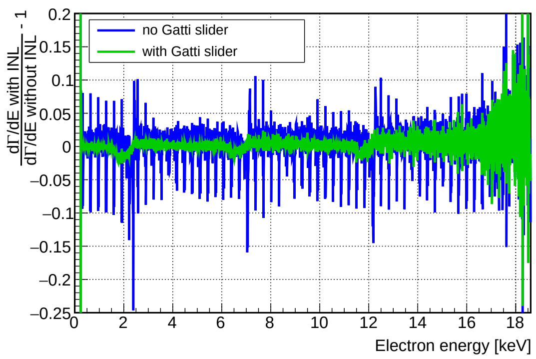

(a)

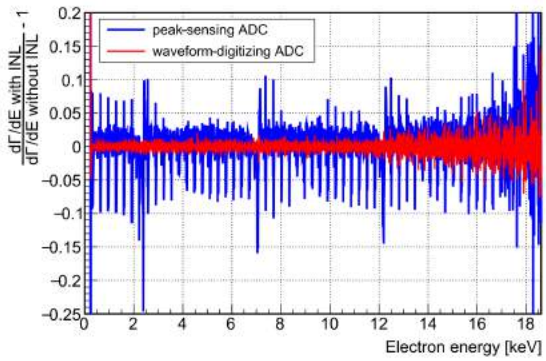

(b)

Figure 4.21: (a) Ratio of tritium β-decay spectrum with and without INL, using a peak-sensing ADC. A *Gatti slider* with a 6-bit counter significantly reduces the fluctuations in the ratio which occur because of the INL periodicity. The INL structure is partially averaged out. **(b)** Comparison of ratios for peak-sensing (no Gatti slider) and waveform-digitizing ADCs. For the waveform-digitizer the periodic INL structure is smeared by reason of the baseline shifts and the resulting varying ADC ranges the waveforms cover.

4.2.4 Conclusions and limitations of MC simulation

In the MC model, pulses are generated, whose energies are drawn from a tritium decay rate distribution. The pulses are de-corrected with INL values to investigate the INL impact on the tritium β-decay spectrum. This is done in two ways that correspond to the working principle of peak-sensing ADCs and waveform-digitizers.

The MC simulations show the advantage of a waveform-digitizing ADC compared to a peak-sensing ADC: It is sensitive to the baseline shift of the signal pulses and smears out the INL structure. However, the simulations have been executed for a 1-pixel detector which sends its pulses to one ADC with one specific INL distribution. To obtain a significant result for a multi-pixel detector and moreover a KATRIN-like statistic with 10^9 counts per second, it is not possible to simulate each single waveform with a MC simulation due to time and calculation power reasons. Analytical simulations have to solve the challenge. They are described in the following section.

4.3 Analytical model for a multi-pixel detector

In this section, the ideas, procedures and simulation results are presented which show the impact of ADC Non-Linearities on the tritium β-decay spectrum, using a multi-pixel silicon detector with one SAR-ADC per pixel, which digitizes the measured pulses. It is shown how the INL impact can be analytically included in the simulation by redistributing bin contents in case of a peak-sensing ADC and by convolution methods in case of a waveform-digitizer.

4.3.1 Peak-sensing model

The impact of the NL on the tritium β-decay spectrum, recorded with a multi-pixel detector (here $N = 10^4$ pixels), is investigated in the following way:

- A tritium β-decay spectrum without statistical fluctuations is calculated analytically according to equation 4.6.
- For each N pixels, an INL spectrum is generated, drawing *gain, offset* and *amplitude* of the INL as free parameters from Gaussian distributions (changing the offset is equivalent to implementing a *Gatti slider*).
- Applying an INL to an energy spectrum can be understood as streching or compressing energy bins (proportional to ADC output code), depending if the respective INL value is > 0 or < 0. Likewise, bin contents can be redistributed for a constant bin width according to the INL values. The latter is done in the simulation. The procedure is displayed in figure 4.22.
- The N resulting energy spectra are summed up and normalized.

- The shifted ratio of the resulting tritium β-decay spectrum and the theoretical input spectrum is calculated.

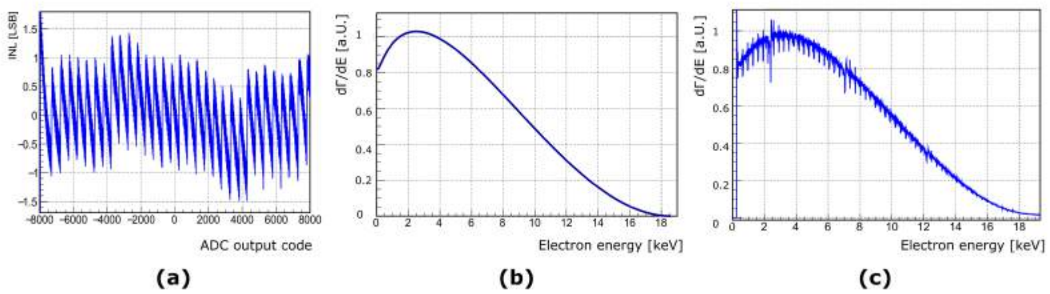

Figure 4.22: Schematic of working principle of the analytical peak-sensing ADC simulation. $N = 10^4$ INL spectra **(a)** are generated and applied to theoretical tritium decay spectra **(b)**. The bin contents get redistributed according to the respective INL value **(c)**.

Figure 4.23 shows the resulting ratio of tritium β-decay spectra with and without INL.

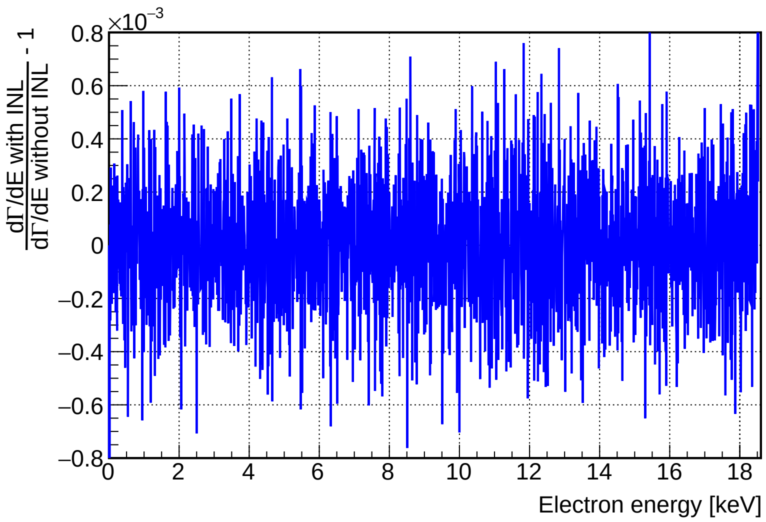

Figure 4.23: Ratio of tritium β-decay spectrum with/without INL with a simulated multi-pixel detector (10^4 pixels). For each pixel the signals are digitized with a peak-sensing ADC with its specific INL spectrum.

The fluctuations are significantly lower compared to the case of only one pixel (figure 4.21) due to the averaging over different INL spectra for different ADCs. They are of the order of 10^{-4}. The big steps in the input INL spectra can not be seen anymore.

4.3.2 Waveform-digitizing model

A convolution method has been developed in this thesis to analytically simulate the impact of INL on the tritium β-decay spectrum by digitizing the analog signals of the detector with a waveform-digitizing ADC. As in the peak-sensing case, the behaviour of a multi-pixel silicon detector with 10^4 pixels is simulated, where each pixel is connected to a SAR-ADC.
The simulation is based on convolutions of the analytically calculated tritium β-decay spectrum with the baseline distribution of the detector output signals and makes use of the working principle of a trapezoidal filter. In this section the convolution method and its necessary ingredients are described and results are shown.

Baseline distribution

As described in section 4.2.3, a waveform-digitizing ADC is sensitive to the baseline of a signal and thus to the ADC range a signal pulse covers. To insert this knowledge into the simulation, a baseline distribution is calculated, see figure 4.24, as a look-up table which is later on used as input to the analytical convolution method.

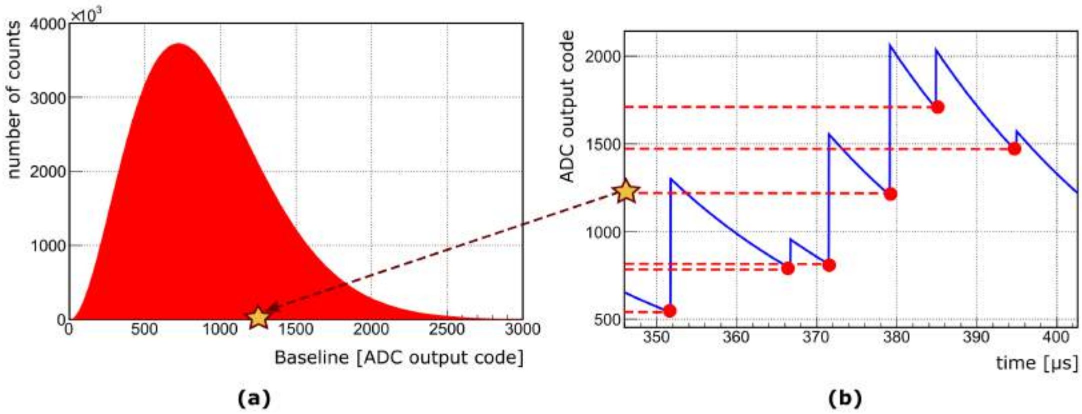

Figure 4.24: (a) The baseline distribution shows the frequency of the respective baseline ADC output codes of the simulated waveforms with the MC pulse train. **(b)** For each waveform, the ADC output code at this point in time before the next signal arises (red dots) is used as an input to the baseline distribution.

To this end, 10^9 waveform are simulated with the MC pulse train. Their energies are drawn from a tritium decay rate PDF, the time between the pulses are drawn from an exponential distribution. The ADC output code in the pulse train just before a new signal rises is used as a baseline value for the baseline distribution. The normalized baseline distribution is taken as a baseline PDF in the simulations.

Trapezoidal filter

According to equation 4.2, the energy output of a trapezoidal filter is calculated by

$$E = \frac{1}{t_{\text{rise}}} \left(\sum_{\text{S2}} \text{wave}[t] - \sum_{\text{S1}} \text{wave}[t] \right). \tag{4.11}$$

The intervals S1 and S2 are defined in figure 4.11. The de-correction of a theoretical waveform due to the INL can be written as

$$\text{wave}_{\text{INL}}[t] = \text{wave}[t] + \text{INL}(\text{wave}[t]) \tag{4.12}$$

(see equation 4.9), where $\text{wave}_{\text{INL}}[t]$ denotes the de-corrected waveform, $\text{wave}[t]$ the uncorrected waveform and $\text{INL}(\text{wave}[t])$ the respective INL value for the ADC output code at time step t.
Consequently, the trapezoidal filter output, i.e. the energy E_{INL} of an INL de-corrected waveform, is

$$\begin{aligned} E_{\text{INL}} &= \frac{1}{t_{\text{rise}}} \left(\sum_{\text{S2}} \text{wave}_{\text{INL}}[t] - \sum_{\text{S1}} \text{wave}_{\text{INL}}[t] \right) \\ &= \frac{1}{t_{\text{rise}}} \left(\sum_{\text{S2}} \text{wave}[t] + \sum_{\text{S2}} \text{INL}(\text{wave}[t]) - \sum_{\text{S1}} \text{wave}_{\text{INL}}[t] - \sum_{\text{S1}} \text{INL}(\text{wave}[t]) \right) \\ &= E + \frac{1}{t_{\text{rise}}} \left(\sum_{\text{S2}} \text{INL}(\text{wave}[t]) - \sum_{\text{S1}} \text{INL}(\text{wave}[t]) \right) \end{aligned} \tag{4.13}$$

with E being the trapezoidal filter output for the waveform without INL de-correction. Equation 4.13 provides a recipe, how to obtain the new energy E_{INL} for a known energy E: Sum up the ADC output codes of the INL spectrum which are hit by a waveform in the intervals $S1$ and $S2$ respectively. Then add (for $S2$) or subtract (for $S1$) them from the former energy E and obtain E_{INL}.

Assuming a constant decay time for all waveforms, it is sufficient to know one specific point of the waveform, e.g. the ADC output code of the baseline just before the signal rises (see figure 4.24), in order to calculate both all required ADC output codes of the waveform within the rise time intervals S1 and S2 and the sums of equation 4.13.

Convolution

In the analytical simulation of a tritium β-decay spectrum, digitized by a waveform-digitizing ADC, the baseline distribution is convoluted with the input infinite-statistics tritium β-decay spectrum. For each combination of baseline value B and electron energy E, the trapezoidal filter output E_{INL} is calculated, using equation 4.13 and an INL spectrum of a simulated SAR-ADC. Finally, for each energy bin, the bin entries get redistributed according to the new obtained energy values E_{INL}.
This procedure is clarified with the help of the following example: Assume a monoenergetic source which yields pulses of the same height, but due to high counting rates the pulses vary in their baseline and cover different ADC ranges. Without INL, in the output energy histogram all events will show up in the same energy bin, e.g. in bin 50. With INL, the calculated average energy bin is different, e.g. 50.3. In this case, we redistribute the counts in such a way that 70% of entries stay in bin 50, while 30% are shifted to bin 51. For an N-pixels detector this procedure is repeated N times, using N different INL input spectra with different gain, amplitude and offset. The spectra are summed up and averaged to get the final energy spectrum.

Figure 4.25 shows the ratios of the resulting tritium β-decay spectrum for a multi-pixel detector with 10^4 pixels with and without INL, for both of the described analytical simulations methods of a peak-sensing and a waveform-digitization case. The fluctuations are two orders of magnitude smaller for the waveform-digitizing ADCs (10^{-6}) than for the peak-sensing ADCs (10^{-4}).

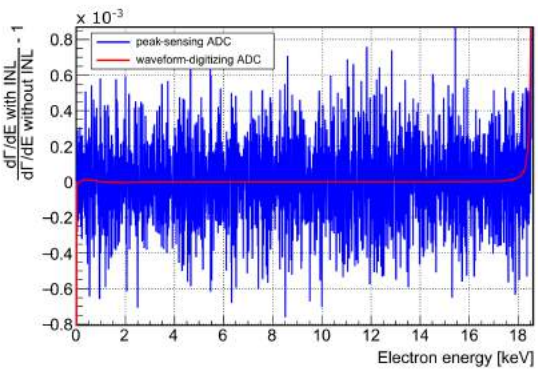

(a)

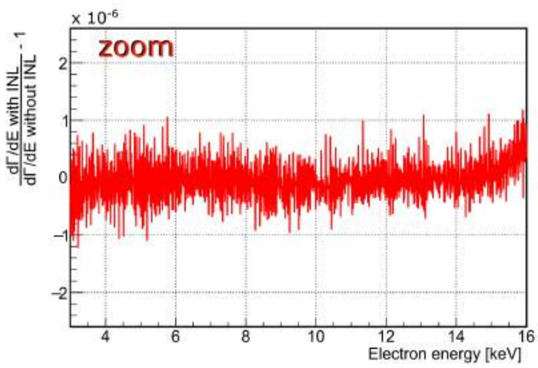

(b)

Figure 4.25: **(a)** Ratio of tritium β-decay spectra with and without INL for the analytical simulation results for peak-sensing and waveform-digitizing ADCs for a multi-pixel detector with 10^4 pixels. The fluctuations for the peak-sensing case are of the order of 10^{-4}. **(b)** A zoom in the ratio for the waveform-digitizing case shows fluctuations of the order of 10^{-6}.

Divergent boundary effects occur, as the ratio of a spectrum with finite energy resolution (spectrum with INL) and a spectrum with infinite resolution (theoretical spectrum) is calculated. This effect is understood and its correction will be the subject of follow-on work.

4.3.3 Mitigation by post-acceleration

A further possibility to mitigate the INL impact on the tritium β-decay spectrum is to use the post-acceleration electrode which already exists in the current KATIRN setup (see figure 2.6). It can be used to shift the entire energy spectrum to higher energies by accelerating all electrons, passing the main spectrometer, with an additional voltage. Figure 4.26 shows the original and five shifted tritium β-decay spectra, which are shifted by the post-acceleration electrode. In the data analysis, this additional post-acceleration energy would then be subtracted from the digitized energy again.

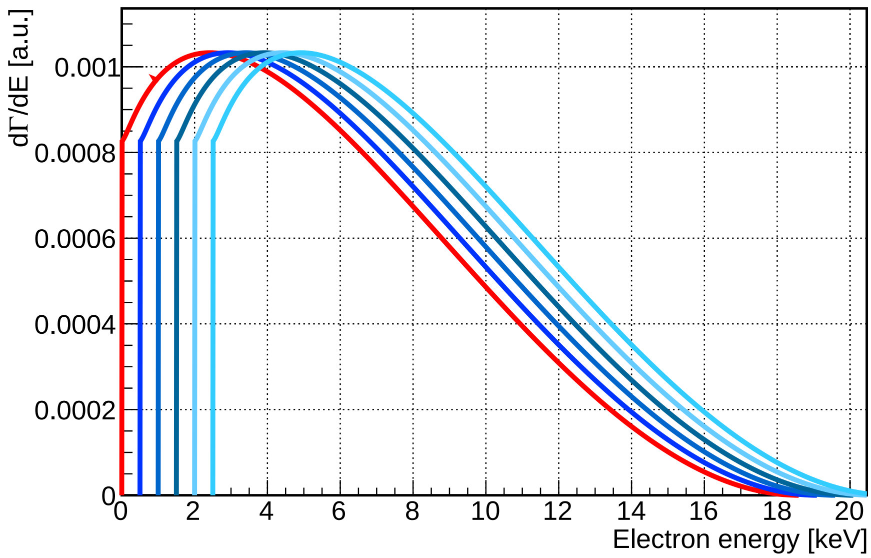

Figure 4.26: The original tritium β-decay spectrum (red) is shifted by additional post-acceleration for different post-acceleration voltages (blue).

With post-acceleration, in contrast to the *Gatti slider*, the covered ADC range of a waveform is not only shifted by a constant offset, but the particle energies themselves are changed, resulting in higher signals with steeper slopes. Signals with steeper slope cover more ADC output codes in the trapezoidal window S2 and the filter averages over more different INL values. Figure 4.27 shows three waveforms: the original waveform of a signal (yellow) which gets shifted by a *Gatti*-slider (green) or experiences additional post-acceleration (red). The covered ADC range with post-acceleration, ΔY_{PA}, is larger than the range $\Delta Y_{\mathrm{Gatti}}$ covered by the *Gatti*-shifted pulse.

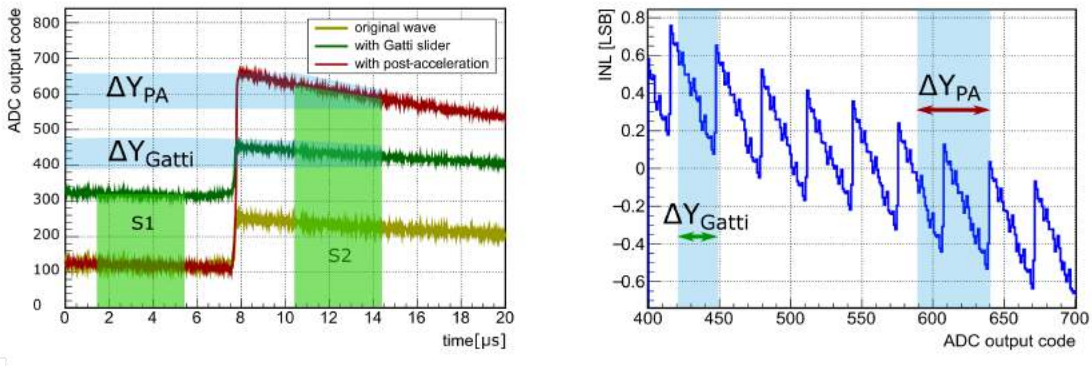

(a) **(b)**

Figure 4.27: **(a)** Whereas a *Gatti slider* changes the ADC range, additional post-acceleration of the incident particles results in higher waveforms which consequently have a steeper slope in the decaying part. More ADC values are covered in the interval S2. **(b)** The covered ADC range of the *Gatti*-shifted waveform (green, range $\Delta Y_{\mathrm{Gatti}}$) and the one with post-acceleration (red, range ΔY_{PA}) in the region $S2$ is different. For the green wave ≈ 30 ADC output codes are averaged to obtain the trapezoidal filter output, for the red wave ≈ 50 ADC bins are covered within the region $S2$. The greater the covered ADC range, the more averaging of the INL periodic structure is done by the trapezoidal filter.

By successively applying different post-acceleration values on particles, their waveforms will have different slopes, leading to different covered ADC ranges and thus to different averages of the periodic INL structures.

Figure 4.28 and 4.29 illustrate the effect of post-acceleration on the ratio of tritium β-decay spectra with and without INL for both peak-sensing and the waveform-digitizing ADCs. For the simulations 100 steps of post-acceleration were assumed, for each one 10 V are added to the acceleration voltage up to 1 kV. The INL fluctuations get reduced by a factor of 10 and reach a level of 10^{-7} for the waveform-digitizing case.

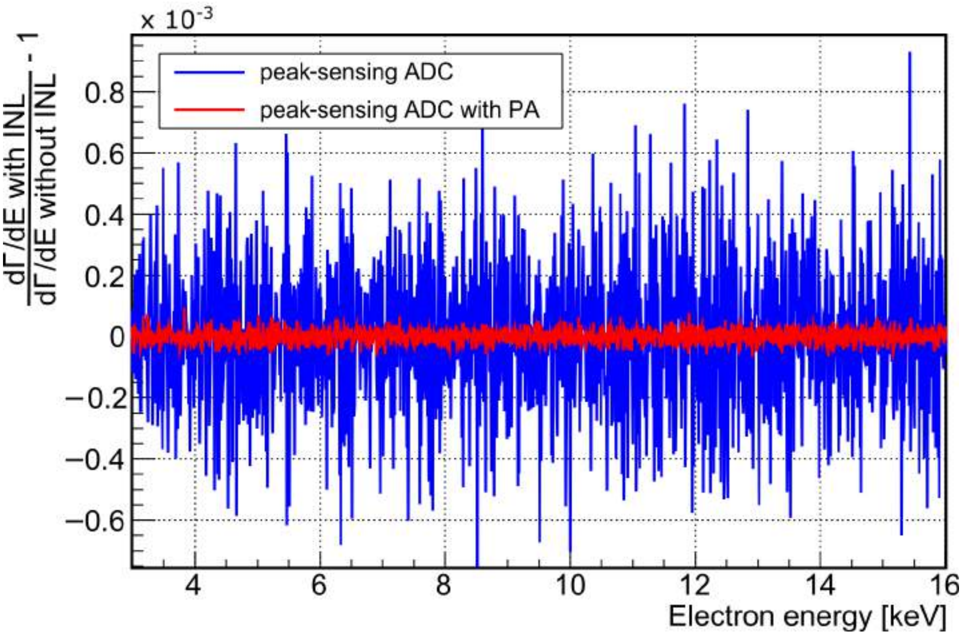

Figure 4.28: Ratio of tritium β-decay spectrum with/without INL and addtional post-acceleration for a 10^4 pixels detector with peak-sensing ADCs. 100 steps of post-acceleration were assumed in these plots, successively increasing by 10 V per step.

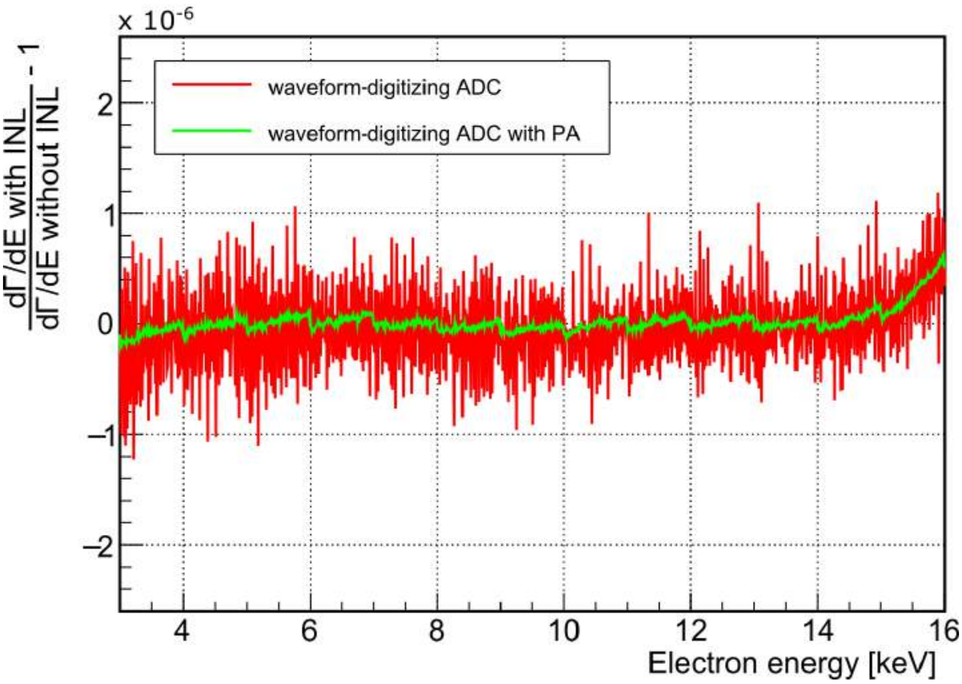

Figure 4.29: Ratio of tritium β-decay spectrum with/without INL and addtional post-acceleration (PA) for a 10^4 pixels detector with waveform-digitizing ADCs. Note the different scale as compared to figure 4.28.

4.3.4 Conclusion

Analytical models have been developed to demonstrate the impact of ADC Non-Linearites on the tritium β-decay spectrum measured by a 10^4 pixels detector, where each pixel is connected to a SAR-ADC. The models are based on INL-induced re-distributions of bin entries and convolution methods. They describe the different behaviours of both peak-sensing and waveform-digitizing ADCs.

The simulations show several possibilities how to mitigate the periodic INL structure which otherwise strongly distorts the energy spectrum:

1. Use of a multi-pixel detector, where each pixel is read out with its own ADC with a specific INL spectrum.
2. A *Gatti*-slider can be used to shift the waveforms in order to cover different ADC ranges.
3. Post-acceleration of the incident particles changes the slope of the signals and increase the covered ADC ranges for each pulse.

Including all mitigation techniques the INL-induced fluctuations can be reduced to a level of 10^{-5} with purely peak-sensing ADCs, whereas sampling and digitizing entire waveforms provides a reduction down to 10^{-7}. Note that a possible INL correction as described in section 4.1.3 can further reduce the magnitude of fluctuations.
In general, a waveform-digitizing ADC yields smaller INL fluctuations and is therefore strongly favoured for the read-out electronic of a future multi-pixel silicon detector to search for sterile neutrinos.

4.4 Impact of NL on the sterile neutrino sensitivity

In this section the impact of ADC Non-Linearities on the sensitivity in the sterile neutrino search with KATRIN is investigated.
A sterile neutrino in the keV range leaves a tiny distortion, a kink-like signature in the tritium β-decay spectrum. If the mixing angle is small enough, the signature is hidden in the INL fluctuations and cannot be detected anymore. Figure 4.30 shows the ratio of tritium β-decay spectra with and without INL. The INL spectrum further contains a mixing of $\sin^2\vartheta = 10^{-4}$ for a sterile neutrino mass $m_s = 10$ keV for a 10^4 pixels detector including the mitigation techniques of the Gatti-slider as well as

post-acceleration. The kink can be seen for both cases, peak-sensing or waveform-digitization of the pulses. For the peak-sensing ADCs, however, the fluctuations are already of the order of the kink itself (10^{-4}). For smaller mixing angles the kink cannot be seen anymore in the peak-sensing case, using waveform-digitizing ADCs a kink at $\sin^2\vartheta = 10^{-6}$ can still be identified, which implies an improvement of two orders of magnitude.

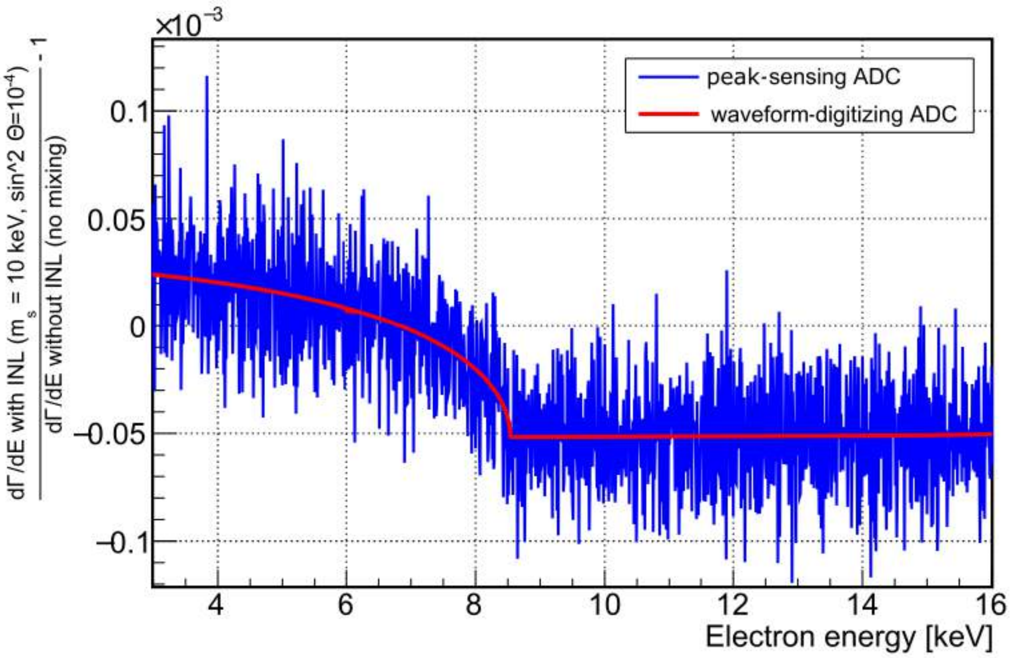

Figure 4.30: Ratio of two tritium β-decay spectra with and without INL. The spectrum with INL additionally includes an active-to-sterile mixing of $\sin^2\vartheta = 10^{-4}$ for a sterile neutrino mass of $m_s = 10$ keV. The ratio is shown for a simulation of a 10^4 pixels detector using peak-sensing (blue) or waveform-digitizing ADCs (red) respectively with the mitigation effects of a *Gatti*-slider and additional post-acceleration.

4.4.1 Mathematical derivation of the covariance matrix

To quantify the INL impact on the sensitivity statistically, covariance and correlation matrices were calculated. For this purpose 1000 KATRIN-like experiments were simulated. Each one measures the tritium β-decay spectrum with a 10^4 pixels detector, read-out by 10^4 ADCs with different INLs. The covariance matrices are compared to the covariance matrices deduced from purely statistically fluctuating

tritium β-decay spectra of 1000 KATRIN-like experiments without any ADC Non-Linearities. The procedure to derive the covariance matrix from a data set follows the instructions in [89].
The covariance matrix is given by

$$\mathbf{V} = \begin{bmatrix} \sum x_1^2/N & \sum x_1 x_2/N & \dots & \sum x_1 x_k \\ \sum x_2 x_1/N & \sum x_2^2/N & \dots & \sum x_2 x_k \\ \dots & \dots & \dots & \dots \\ \sum x_k x_1/N & \sum x_k x_2/N & \dots & \sum x_k^2 \end{bmatrix}, \tag{4.14}$$

where N is the number of experiments, k the number of bins of the tritium β-decay spectra, x_i is a deviation score (= difference of the raw score and the mean score) of the ith data set (i.e. the ith experiment):

$$x_i = y_i - \bar{y}_i, \tag{4.15}$$

where y_i denotes the raw score for the ith experiment and $\bar{y}_i$ the mean score of all observations y_i.
On the diagonal of this symmetric matrix the variance is displayed. The non-diagonal elements show the covariance between different columns.

Let $\mathbf{X}$ be a N x k matrix (here $N = 1000$, $k = 186$) with the raw data sets of N tritium β-decay spectra with k bins respectively. To derive the covariance matrix two steps have to be executed:

- Calculate the deviation score matrix $\mathbf{x}$ by

$$\mathbf{x} = \mathbf{X} - \frac{\mathbf{11'X}}{N}, \tag{4.16}$$

  where $\mathbf{1}$ denotes an n x 1 column vector of ones, $\mathbf{1'}$ its transposed row vector.

- Calculate the deviation sums shown in 4.14 and normalize them to N, the number of experiments:

$$\mathbf{V} = \frac{\mathbf{x'x}}{N}. \tag{4.17}$$

  Additionally, the correlation matrix $\boldsymbol{\rho}$ is derived by

$$\boldsymbol{\rho} = \frac{\mathbf{V}}{\sigma_i \sigma_j} \tag{4.18}$$

  with the standard deviations $\sigma_i = \sqrt{V_{ii}}$ and $\sigma_j = \sqrt{V_{jj}}$.

4.4.2 Covariance matrix of tritium β-decay spectra with INL

Figure 4.31 displays the covariance matrix (a) and the correlation matrix (b) for the case of a 10^4 pixels detector with peak-sensing ADCs and additional post-acceleration of the electrons. The second line of the plots shows a zoom into the covariance matrix of the peak-sensing case (c), to be compared with a zoom in the covariance matrix of purely poisson statistical fluctuating tritium β-decay spectra (d). The covariance matrices for both cases of statistical or INL fluctuations show huge values on the main diagonal and small fluctuating non-diagonal elements. This demonstrates that spectrum deviations due to ADC Non-Linearities have almost a purely statistical character and negligible correlations between neighbouring energy bins.

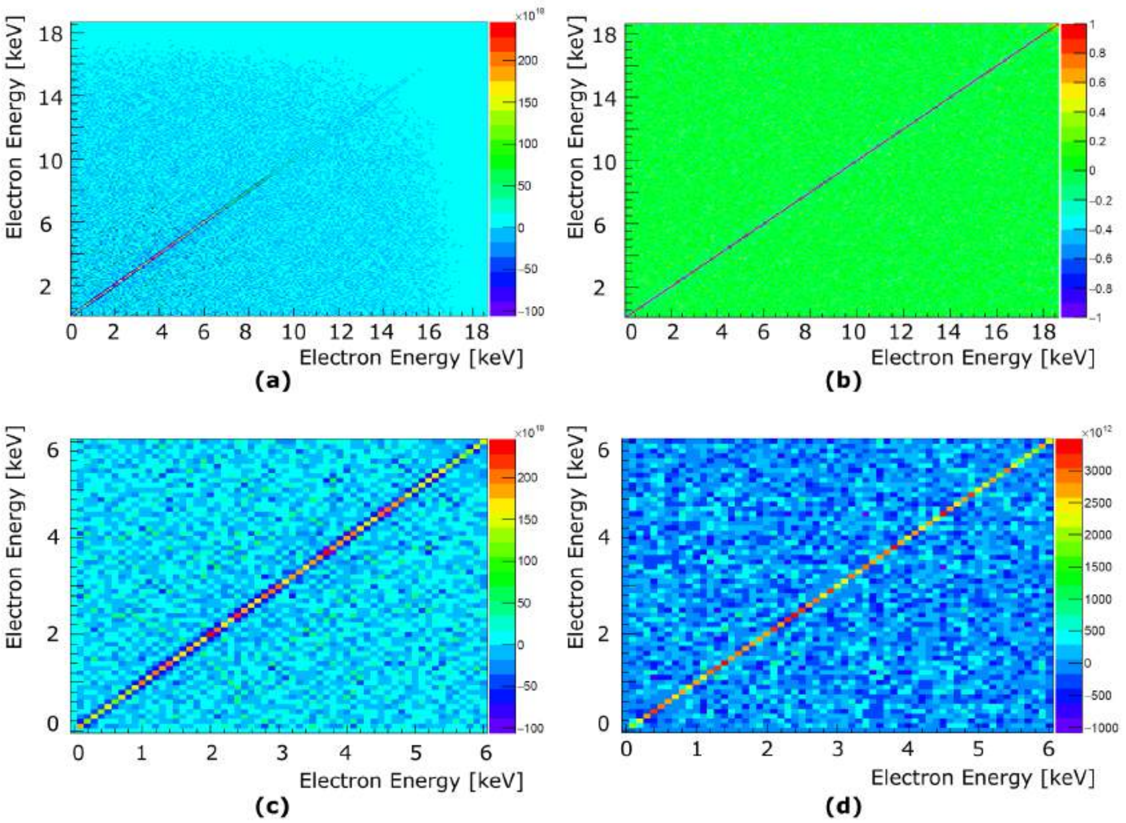

Figure 4.31: Covariance Matrix of tritium decays of 1000 simulated KATRIN-like experiments with a 10^4 pixels detector, read out by peak-sensing ADCs with additional post acceleration of the elctrons **(a)** and the corresponding correlation matrix **(b)**. **(c)** is an xy-zoom into the covariance matrix of (a) and **(d)** shows a zoom into the covariance matrix for 1000 tritium β-decay spectra with purely poisson statistical fluctuations (no INL). The INL fluctuations behave like an additional statistical error on the energy spectrum and do not insert significant correlations between the energy bins.

In contrast to the statistical error, the INL-based fluctuations do not depend on the source strength, i.e. the statistics of the experiment. Whereas the relative statistical error decreases with increasing statistic $\sigma_{\text{stat}} = \frac{\sqrt{N_E}}{N_E}$ (N_E is the number of measured electrons with energy E), the uncertainty based on the ADC Non-Linearities is independent of the experiment's total statistics. It appears as a percental effect and leads to a percental redistribution of energy bin contents. Nevertheless, it behaves as a statistical error in the sense of adding no significant correlations between energy bins.

Figures 4.32 compares the magnitude of the relative uncertainties σ_{rel}, based on statistical effects (source strength, i.e. the number of tritium molecules N_{mol} in the source) and based on INL fluctuations for different numbers of pixels for both peak-sensing and waveform-digitizing ADCs as a function of the electron energy.

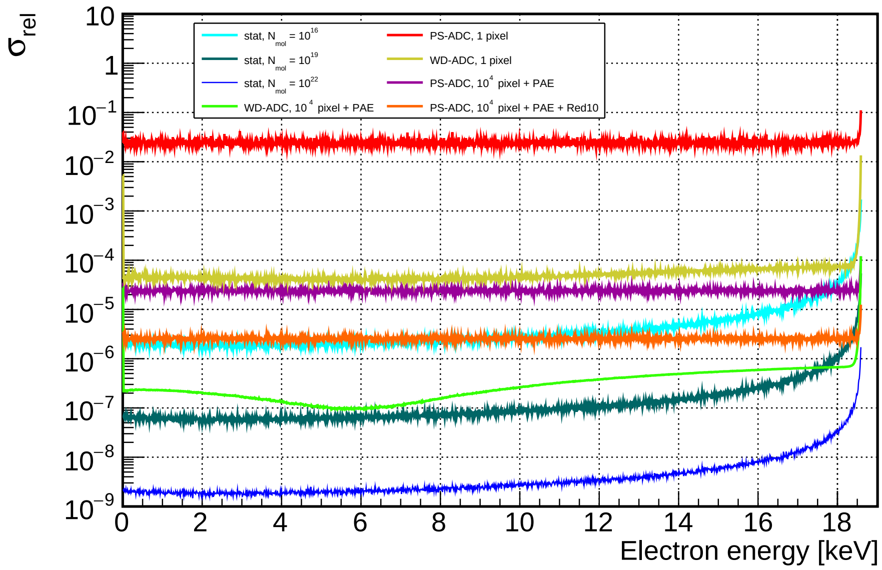

Figure 4.32: Comparison of the relative errors σ_{rel}. With an increasing source strength N_{mol} the relative statistical uncertainty decreases, for large energies it increases due to lower statistics near the endpoint. The INL-induced uncertainties depend on the applied mitigation techniques discussed in section 4.3. σ_{rel} decreases by increasing the number of pixels, by using waveform-digitizing (WD) instead of peak-sensing (PS) ADCs and by using the post-acceleration electrode (PAE). Red10 denotes an INL reduction by a factor of 10.

Figure 4.33 displays σ_{rel} for a fixed energy as a function of N_{mol}. The values σ_{rel} are derived from the diagonal elements of the covariance matrix calculations described above.

As discussed in section 4.3, the INL-induced fluctuations are mitigated by going

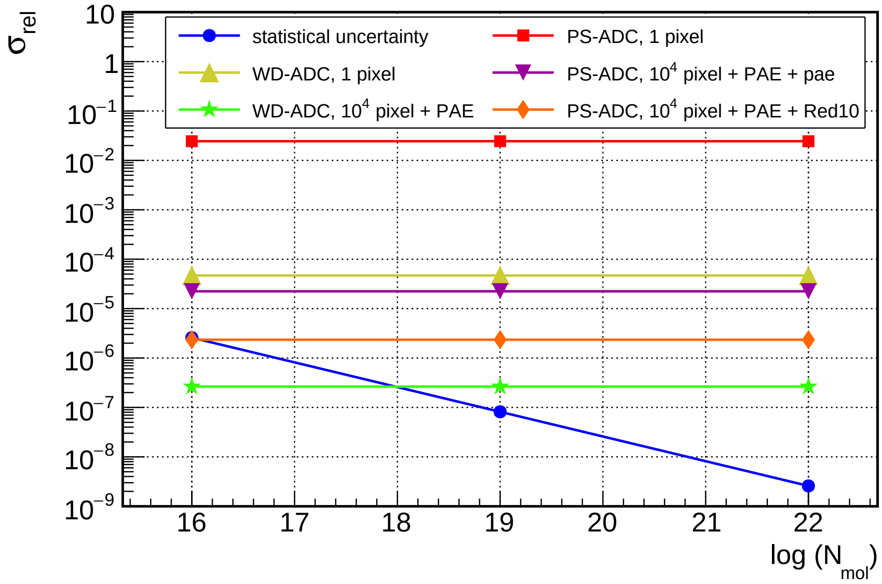

Figure 4.33: Dependency of σ_{rel} on source strength N_{mol} for a fixed energy of $E = 10$ keV, i.e. a cross section through figure 4.32 at $E = 10$ keV.

to higher numbers of pixels and by digitizing entire waveforms instead of using peak-sensing ADCs. For a waveform-digitizing ADC with 10^4 pixels, uncertainties of the order of 10^{-7} can be reached. This is of the same order as the statistical error for the nominal KATRIN source strength of $N_{\text{mol}} \approx 10^{19}$ tritium molecules. A similarly small error could be reached by using a peak-sensing ADC but reducing the NL by a factor of 10. This could be either achieved by a highly linear ADC, whose fluctuations in the INL spectrum vary only between roughly ± 0.1 LSB (in the simulations fluctuation $\approx \pm 1.5$ LSB were assumed, see figure 4.7), or by a significant measurement-based INL correction with no more than 10% residual INL. A combination of both methods is also possible.
In all other cases, the error due to NL significantly outweighs the purely statistical error that would be achieved with the nominal source strength of

4.4.3 Sensitivity at 90% confidence level

Based on a χ^2-test [90] with 90% confidence level, an exclusion limit in the m_s-$\sin^2 \vartheta$-plane is calculated to derive the impact of ADC Non-Linearities on the KATRIN sensitivity to search for sterile neutrinos in the keV mass regime.

χ^2-test

In order to obtain a 90% C.L. exclusion curve to show the INL impact on the sensitivity of a sterile neutrino search with KATRIN, a χ^2-test is executed. The χ^2 test is a useful analysis tool to reject a nullhypothesis λ with a significance level α. In this content the test statistic χ^2 is given by

$$\chi^2(\lambda) = \sum_{i,j=1}^{n} (y_i - \lambda_i)(V^{-1})_{ij}(y_j - \lambda_j), \tag{4.19}$$

where λ is the nullhypothesis, stating that there is a sterile neutrino with mass m_s and mixing angle $\sin^2\vartheta$, y are simulated measurement data with no sterile neutrinos, V^{-1} denotes the inverse covariance matrix and n is the number of energy bins.

In the following investigations the non-diagonal elements of the covariance matrices are neglected, as no significant correlations exist between the energy bins (see figure 4.31). In this case equation 4.19 reduces to

$$\chi^2(\lambda) = \sum_{i=1}^{n} \frac{(y_i - \lambda_i)^2}{\sigma_i^2}, \tag{4.20}$$

with $\sigma_i = \sqrt{V_{ii}}$.

For a given $\lambda(m_s, \vartheta)$ and a simulated measured spectra y, the test statistic χ^2 is calculated to derive the p-value

$$p = \int_{\chi^2}^{\infty} f(z, n_d)\, \mathrm{d}z, \tag{4.21}$$

where n_d denotes the degrees of freedom (here $n_d = 2$: mass m_s and mixing angle ϑ) and $f(z, n_d)$ is the corresponding χ^2 distribution for n_d degrees of freedom.

For a significance level $\alpha = 10\%$ (which implies a confidence level of 90%) the nullhypothesis $\lambda(m_s, \vartheta)$ is rejected with 90% C.L. if $p < \alpha$, i.e. the measured data exclude the existence of a sterile neutrino for this region in the m_s-$\sin^2\vartheta$-plane. This is equivalent to rejecting the nullhypothesis $\lambda(m_s, \vartheta)$ if $\chi^2 > 4.605$ (critical value for χ^2-distribution with two degrees of freedom).

Figure 4.34 shows the 90% C.L. exclusion curve resulting from a χ^2-scan of the m_s-$\sin^2\vartheta$-plane. The areas on the right of the respective curves are excluded, i.e. the nullhypothesis of a sterile neutrino with mass and mixing angle in this region is rejected with 90% C.L. if KATRIN does not detect a sterile neutrino signal in measurement data. For a one-pixel detector with a purely peak-sensing ADC only a sensitivity $> 10^{-3}$ can be reached. Two orders of magnitude are gained by replacing the peak-sensing ADC with a waveform-digitizer. For a multi-pixel detector with 10^4 pixels and additional usage of the post-acceleration electrode, a sensitivity down to 10^{-6} can be reached with a peak-sensing ADC. It can be improved with a reduction of the INL for each ADC by a factor of ten by means of highly linear ADCs and successful INL corrections. Finally, the best-case sensitivity in respect to a sterile neutrino search is obtained with a 10^4 pixels detector and waveform-digitizing ADCs with additional post-acceleration. It reaches a sensitivity of $\sin^2 \vartheta = 10^{-7}$ without any INL correction.

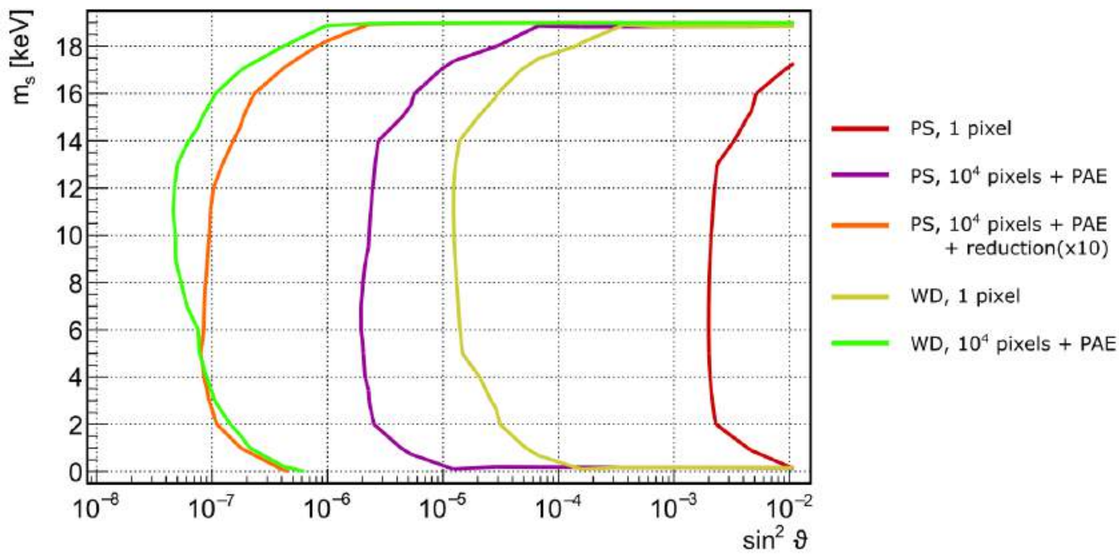

Figure 4.34: 90% C.L. exclusion curves. The plot shows the KATRIN sensitivity with respect to a sterile neutrino search for different detector and read-out configurations. For an increased number of pixels and waveform-digitizing (WD) instead of peak-sensing (PS) ADCs, the impact of ADC Non-Linearities is mitigated and the sensitivity increases down to a mixing angle of $\sin^2 \vartheta = 10^{-7}$ (green). With an INL reduction by a factor of 10 almost the same sensitivity can be reached with peak-sensing ADCs (orange).

4.5 Conclusion

In this chapter, the impact of ADC Non-Linearities on the KATRIN sensitivity in the search for sterile neutrinos was investigated. The investigations were based on the Non-Linearity of a Successive Approximation Register (SAR) ADC as it is used

in the *GRETINA* digitizer with INL fluctuations of the order of ± 1.5 LSB.
For a novel multi-pixel detector for the KATRIN experiment, the results recommend the usage of waveform-digitzing ADCs. They are sensitive to shifts in the signal baseline and thus offer a good intrinsic smearing of the INL structures, especially for high count rates at the detector. Moreover, digitized waveforms offer the possibility of a pulse shape analysis and provide a tool to reject pile-up events. On the other hand waveform-digitizers are expensive and an individual ADC for each pixel is space-consuming. Hence, the number of pixels is limited in this scenario.
Read-out systems with peak-sensing ADCs show to be less sensitive, but appear to be less expensive and space-consuming, since they can be directly implemented in the read-out ASIC close to the detector itself. In a peak-sensing case an intrinsic low INL is required and mitigation techniques of a *Gatti slider* and additional post-acceleration of the electrons before they hit the detector will be necessary to achieve a high sensitivity.

5 Conclusion

The KATRIN experiment shows high potential to search for sterile neutrinos. To detect the tiny kink-like signature of a keV-scale sterile neutrino in the electron spectrum from tritium β-decay, the measurement interval has to be extended from a narrow region very close to the endpoint (where the impact of the neutrino mass is maximal) to cover the entire tritium β-decay spectrum. The unprecedented source luminosity of the gaseous source is advantageous for a keV-scale sterile neutrino search as it provides high statistics and small systematic effects. Hence, it allows to probe small active-to-sterile mixing angles. However, with the nominal source strength, typical counting rates at the focal plane detector will be 12 orders of magnitude higher than in the normal mode of operation. Consequently, a novel multi-pixel detector and read-out system are required for a high-statistics keV-scale sterile neutrino search.

This R&D effort is the focus of this thesis and covers two main aspects: 1) the commissioning and test of the first prototype detector of the novel design and 2) the study of the impact of ADC non-linearities on the final sensitivity of an upgraded KATRIN setup to detect sterile neutrinos. The new Si-detector design combines the advantages of the drift ring design (SDD) with an ultra-thin dead layer. A first prototype was developed at the Halbleiter Labor (HLL) of the Max-Planck society, Munich and Lawrence Berkeley National Laboratory.

In the framework of this thesis, a ceramic printed circuit board (hybrid) was developed for the HLL prototype. First detector tests with this hybrid revealed the functionality of the sensor itself and the integrated electronics system. To conduct a detailed characterization of the detectors, a dedicated test stand was commissioned in the context of this thesis. It entails a vacuum chamber, cooling system, back-end read-out electronic, voltage supplies as well as a radioactive source and detector holding structure. The development of the hybrid, the initial tests and the test stand will be essential for the future development and design optimization of the detector system.

The second major result of this thesis is the development of efficient mitigation techniques against the sensitivity-limiting effect of ADC Non-Linearities. These

were identified to be one of the major systematic effects in a keV-scale sterile neutrino search with an upgraded KATRIN setup. In this context, dedicated measurements of the NLs of a Successive Approximation Register ADC were performed at Lawrence Berkeley National Laboratory and a new method of NL correction was successfully tested and implemented.
With detailed Monte Carlo and analytical simulations, the quantitative impact of ADC NLs on the tritium β-decay spectrum was investigated. Three major ways to mitigate the effect of NL from the percent level to the ppm level were developed. These are based on 1) a measurement-based NL correction, 2) the usage of waveform-digitization and 3) the application of the post-acceleration electrode of KATRIN to wash-out periodic NL structures. The best result, which reduces the effect of NLs to a negligible level of 10^{-7} is achieved for a multi-pixel detector, with each pixel being equipped with its own waveform-digitizing ADC.
This design proposal will be instrumental for the implementation of a future detector and read-out system to search for keV-scale sterile neutrinos with KATRIN.

List of Figures

List of Tables

Bibliography

[1] T. Asaka and M. Shaposhnikov, "The nuMSM, dark matter and baryon asymmetry of the universe," *Physics Letters B*, vol. 620, 2005.

[2] J. Chadwick, "Intensitaetsverteilung in magnetischen Spektren der beta Strahlen von Radium B und C," *Verhandlungen der Deutschen physikalischen Gesellschaft*, pp. 383–391, 1914.

[3] Pauli Letter Collection, CERN.

[4] F. A. Scott, "Energy Spectrum of the Beta-Rays of Radium E," *Physical Review*, vol. 48, 1935.

[5] F. Reines and C. Cowan, "The neutrino," *Nature*, vol. 178, pp. 446–449, September 1956.

[6] J. Bahcall and A. Serenelli, "New solar opacities, abundances, helioseismology and neutrino fluxes," *The Astrophysical Journal*, vol. 621, pp. 85–88, March 2005.

[7] R. Davis *et al.*, "Search for Neutrinos from the Sun," *Physical Review Letters*, vol. 20, pp. 1205–1209, May 1968.

[8] P. Anselmann *et al.*, "GALLEX results from the first 30 solar neutrino runs," *Physics Letters B*, vol. 327, pp. 377–385, May 1994.

[9] J. Abdurashitov *et al.*, "Results from SAGE (The Russian-American gallium solar neutrino experiment)," *Physics Letters B*, vol. 328, pp. 234–248, May 1994.

[10] Y. Fukuda *et al.*, "Measurements of the Solar Neutrino Flux from Super-Kamiokande's First 300 Days," *Physical Review Letters*, vol. 81, pp. 1158–1162, August 1998.

[11] G. Ardsma *et al.*, "A heavy water detector to resolve the solar neutrino problem," *Physics Letters B*, vol. 194, pp. 321–325, August 1987.

[12] B. Aharmim *et al.*, "Determination of the ν_e and total B8 solar neutrino fluxes using the Sudbury Neutrino Observatory Phase 1 data set," *Physical Review C*, vol. 75, pp. 1–69, April 2007.

[13] Y. Fukuda *et al.*, "Evidence for Oscillation of Atmospheric Neutrinos," *Physical Review Letters*, vol. 81, pp. 1562–1567, August 1998.

[14] F. P. An *et al.*, "Observation of Electron-Antineutrino Disappearance at Daya Bay," *Physical Review Letters*, vol. 108, pp. 1–7, April 2012.

[15] K. Abe *et al.*, "Precise Measurement of the Neutrino Mixing Parameter θ_{23} from Muon Neutrino Disappearance in an Off-Axis Beam," *Physical Review Letters*, vol. 112, pp. 1–8, May 2014.

[16] `http://www-sk.icrr.u-tokyo.ac.jp/nu98/scan/063/063-13.jpg`, homepage of *Neutrino 98* conference, called on 5th February 2016.

[17] B. Pontecorvo, "Inverse beta processes and nonconservation of lepton charge," *Sov.Phys.JETP*, vol. 7, pp. 172–173, 1958.

[18] Z. Maki *et al.*, "Remarks on the unified model of elementary particles ," *Progress of Theoretical Physics*, vol. 28, pp. 870–880, 1962.

[19] Press release by "The Royal Swedish Academy of Sciences" to award the Nobel Prize in Physics for 2015, October 2015.

[20] C. Kraus *et al.*, "Final results from phase II of the Mainz neutrino mass search in tritium beta decay," *European Physic Journal C*, vol. 40, pp. 447–468, April 2005.

[21] J. Angrik and others, "KATRIN design report," 2004.

[22] M. Agostini *et al.*, "Results on Neutrinoless Double β Decay of ^{76}Ge from Phase I of the GERDA Experiment," *Physical Review Letters*, vol. 111, 2013.

[23] A. Gando *et al.*, "Limit on Neutrinoless $\beta\beta$ Decay of Xe136 from the First Phase of KamLAND-Zen and Comparison with the Positive Claim in Ge76," *Physical Review Letters*, vol. 110, February 2013.

[24] P. Gorla *et al.*, "The CUORE experiment: status and prospects," *Journal of Physics: Conference Series*, vol. 375, 2012.

[25] W. Konetschny and W. Kummer, "Nonconservation of total lepton number with scalar bosons," *Physics Letters B*, vol. 70, October 1977.

[26] T. Schwetz, "Neutrinos in the Standard Model of Particle Physics and Beyond," Talk at ν-Dark 2015 Workshop, TUM Munich.

[27] R. Adhikari *et al.*, "A White Paper on keV Sterile Neutrino Dark Matter," *arXiv:1602.04816*, February 2016.

[28] M. Gell-Mann *et al.*, "Complex Spinors and Unified Theories (North-Holland, Amsterdam, 1979)," *Proceedings of the Stony Brook Supergravity Workshop*, 1979. Stony Brook, Amsterdam, New York, 1979.

[29] R. N. Mohapatra and G. Senjanovic, "Neutrino Mass and Spontaneous Parity Nonconservation," *Physical Review Letters*, vol. 44, April 1980.

[30] M. Lindner *et al.*, "See-saw Mechanisms for Dirac and Majorana Neutrino Masses," *Physical Review D*, vol. 65, February 2002.

[31] J. Fan, "Light sterile neutrinos and short baseline neutrino oscillation anomalies," *Journal of High Energy Physics*, vol. 83, April 2012.

[32] J. M. Conrad *et al.*, "The LSND and MiniBooNE Oscillation Searches at High Δm^2," *Annual Review of Nuclear and Particle Science*, vol. 63, 2013.

[33] H. J. de Vega and N. G. Sanchez, "Model independent analysis of dark matter points to a particle mass at the keV scale," *Monthly Notices of the Royal Astronomical Society*, vol. 404, 2010.

[34] A. Boyarsky *et al.*, "The Role of Sterile Neutrinos in Cosmology and Astrophysics," *arXiv:0901.0011*, 2008.

[35] A. Schneider, "Structure formation with suppressed small-scale perturbations," *Monthly Notices of the Royal Astronomical Society*, vol. 451, 2015.

[36] N. Menci *et al.*, "Galaxy Formation in WDM Cosmology," *Monthly Notices of the Royal Astronomical Society*, vol. 421, 2012.

[37] M. R. Lovell *et al.*, "The Haloes of Bright Satellite Galaxies in a Warm Dark Matter Universe," *Monthly Notices of the Royal Astronomical Society*, vol. 420, 2012.

[38] J. F. Navarro *et al.*, "A Universal density profile from hierarchical clustering," *Astrophysical Journal*, vol. 490, 1997.

[39] D. Weinberg *et al.*, "Cold dark matter: Controversies on small scales," *Proceedings of the National Academy of Sciences*, October 2015.

[40] S. Tremaine and J. E. Gunn, "Dynamical Role of Light Neutral Leptons in Cosmology," *Physical Review Letters*, vol. 42, 1979.

[41] E. Papastergis and F. Shankar, "An assessment of the "too big to fail" problem for field dwarf galaxies in view of baryonic feedback effects," *arXiv:1511.08741v1*, November 2015.

[42] E. Bulbul *et al.*, "Detection of An Unidentified Emission Line in the Stacked X-ray spectrum of Galaxy Clusters," *Astrophysical Journal*, vol. 789, 2014.

[43] O. Urban *et al.*, "A Suzaku Search for Dark Matter Emission Lines in the X-ray Brightest Galaxy Clusters," *arXiv:1411.0050*, November 2014.

[44] T. Tamura *et al.*, "An X-ray Spectroscopic Search for Dark Matter in the Perseus Cluster with Suzaku," *arXiv:1412.1869*, December 2014.

[45] M. Viel *et al.*, "Warm dark matter as a solution to the small scale crisis: New constraints from high redshift Lyman-α forest data," *Physical Review D*, vol. 88, 2013.

[46] A. Boyarsky *et al.*, "Constraints on sterile neutrinos as dark matter candidates from the diffuse X-ray background," *Monthly Notices of the Royal Astronomical Society*, vol. 370, 2006.

[47] S. Horiuchi *et al.*, "Sterile neutrino dark matter bounds from galaxies of the Local Group," *arXiv:1311.0282*, 2013.

[48] B. Bornschein, "The closed Tritium cycle of KATRIN," *Progress in Particle and Nuclear Physics*, vol. 57, 2006.

[49] M. Schloesser *et al.*, "In-Line Calibration of Raman Systems for Analysis of Gas Mixtures of Hydrogen Isotopologues with Sub-Percent Accuracy," *Analytical Chemistry*, vol. 85, 2013.

[50] F. Priester *et al.*, "Commissioning and detailed results of KATRIN inner loop tritium processing system at Tritium Laboratory Karlsruhe," *Vacuum*, vol. 116, June 2015.

[51] Picture by K. Valerius, KATRIN Collaboration.

[52] M. Ubieto-Diaz *et al.*, "A broad-band FT-ICR Penning trap system for KATRIN," *International Journal of Mass Spectrometry*, vol. 288, 2009.

[53] W. Gil *et al.*, "The Cryogenic Pumping Section of the KATRIN Experiment ," *IEEE transactions on applied superconductivity*, vol. 20, June 2010.

[54] Picture by the KATRIN collaboration.

[55] J. W. B. Flatt, "Design of the KATRIN pre-spectrometer ," *Nuclear Physics B*, vol. 118, April 2003.

[56] M. Zboril *et al.*, "Ultra-stable implanted $^{83}Rb/^{83m}Kr$ electron sources for the energy scale monitoring in the KATRIN experiment," *Journal of Instrumentation*, vol. 8, March 2013.

[57] J. Amsbaugh *et al.*, "Focal-plane detector system for the KATRIN experiment," *Nuclear Instruments and Methods in Physics Research A*, vol. 778, 2015.

[58] J. Schwarz, "The detector system of the KATRIN experiment - Implementation and first measurements with the spectrometer," PhD Thesis, KIT, 2014.

[59] Personal communication with Sanshiro Enomoto.

[60] S. Mertens *et al.*, "Sensitivity of next-generation tritium beta-decay experiments for keV-scale sterile neutrino search," *Journal of Cosmology and Astroparticle Physics*, vol. 20, 2015.

[61] S. Mertens, K. Dolde, M. Korzeczek, *et al.*, "Wavelet approach to search for sterile neutrinos in tritium β-decay spectra," *Physical Review D*, vol. 91, 2015.

[62] H. Spieler, "Front-End Electronics and Signal Processing," *Instrumentation in Elementary Particle Physics*, 2003. AIP Conf. Proc. 674.

[63] Drawing by the David Radford.

[64] `http://www.hll.mpg.de`, called on 14th March 2016.

[65] `http://sensors.lbl.gov`, called on 14th March 2016.

[66] C. Kittel, *Introduction to Solid State Physics*. John Wiley and Sons, Inc., 2004. New York, London, Sydney, Toronto.

[67] F. Hartmann, *Evolution of Silicon Sensor Technology in Particle Physics*. Springer-Verlag Berlin Heidelberg, 2009.

[68] Drawing by Peter Lechner, HLL.

[69] Personal communication with Peter Lechner, HLL Muenchen.

[70] Drawing by Craig Tindal, LBNL.

[71] Personal communication with Ivan Peric, Roberto Blanco, Lars Eisenblaetter (KIT/IPE).

[72] Technical drawing by K. Schaefer, KIT/IKP.

[73] L. Michaeli *et al.*, "Unified ADC nonlinearity error model for SAR ADC," *ScienceDirect*, pp. 198–204, Measurement 41, 2008.

[74] P. Suchanek *et al.*, "ADC Nonlinearity Correction Based on INL(n) Approximations," *IEEE International Workshop on Intelligent Data Acquisition and Advanced Computing Systems: Technology and Applications*, September 2009.

[75] "Analog Devices, Datasheet A/D Converter AD6645." `http://www.analog.com/media/en/technical-documentation/data-sheets/AD6645.pdf`, called on 20th January 2016.

[76] `http://orca.physics.unc.edu/Getting_Started/Index.html`, called on 14th March 2016.

[77] D. Radford, "Nonlinearities in the GRETINA Digitizers," Talk at Majorana Collaboration Meeting, October 2012.

[78] M. V. Bossche *et al.*, "Dynamic testing and diagnostics of A/D converters," *IEEE Transactions on Circuits and Systems*, vol. CAS-33, August 1986.

[79] Personal communication with Jason Detwiler, University of Washington.

[80] S. Mertens *et al.*, "Majorana Collaborations Experience with Germanium Detectors ," *Journal of Physics*, Conference Series 606 (2015)012005, 2015.

[81] C. Aalseth *et al.*, "The majorana ^{76}Ge double-beta decay project," *Nuclear Physics B*, vol. 124, July 2003.

[82] `http://www.nucleide.org/DDEP_WG/Nuclides/Co-60_tables.pdf`, called on 20th January 2016.

[83] http://www.nucleide.org/DDEP_WG/Nuclides/Ba-133_tables.pdf, called on 20th January 2016.

[84] V. T. Jordanov and G. F. Knoll, "Digital synthesis of pulse shapes in real time for high resolution radiation spectroscopy," *Nuclear Instruments and Methods in Physics Research Section A*, vol. 345, pp. 337–345, 1994.

[85] R. Grzywacz, "Applications of digital pulse processing in nuclear spectroscopy," *Nuclear Instruments and Methods in Physics Research Section B*, vol. 204, pp. 649–659, 2003.

[86] F. Adamo *et al.*, "Frequency Domain Analysis for Dynamic Nonlinearity Measurement in A/D Converters," *IEEE transactions on instrumentation and measurement*, pp. 760–769, 2007.

[87] L. Devroye, *Non-Uniform Random Variate Generation*. Springer Verlag, New York, 1986. p.42.

[88] E. Gatti *et al.*, "A new method for analog to digital conversion," *Nuclear Instruments and Methods*, pp. 241–242, June 1963.

[89] http://stattrek.com/matrix-algebra/covariance-matrix.aspx, called on 28th January 2016.

[90] G. Cowan, *Statistical Data Analysis*. Oxford Science Publications, 1997.